

Characterization of a Ti(Mo)C-Ni Cermet for Use in Impact Resistant Sandwich Panels

---

A Thesis

Presented to

the faculty of the School of Engineering and Applied Science

University of Virginia

---

In Partial Fulfillment

Of the requirements for the Degree

Master of Science (Materials Science)

By

Jasmine Imani Keene

December 2013

APPROVAL SHEET

The thesis  
is submitted in partial fulfillment of the requirements  
for the degree of  
Master of Science

Jasmine Imani Keene

AUTHOR

This thesis has been read and approved by the examining Committee

---

Elizabeth Opila, Committee Chair

---

Sean Agnew, Advisor

---

Haydn Wadley

## ABSTRACT

The deflection of edge-clamped plates during out of plane impulsive loading is proportional to a merit index given by the square root of the ratio of the plate material strength to its density [1]. Even smaller deflections can be achieved if sandwich panels with cellular cores can be made from these high specific strength materials. Ti(Mo)C-Ni based cermets have been identified as a potentially superior material for this application since their compressive strength is typically 2-3 GPa and their density is in the 5,500 kg/m<sup>3</sup> range. The merit index of this cermet exceeds that of all known metallic systems. Although the toughness of cermets generally exceeds that of ceramics, they have low fracture toughness relative to many metals and this will inhibit their suitability for some applications.

A comprehensive characterization of the mechanical properties of Ti(Mo)C-Ni cermets has been conducted in order to determine if it is a viable candidate for use in truss core sandwich panels. Additionally, the lack of well-established fabrication and joining techniques needed to fabricate sandwich panels is also a concern. The feasibility of using a transient liquid phase bonding (brazing) technique to fabricate a cellular structure was also therefore investigated.

The cermet system investigated here is found to have a density of 5,520 kg/m<sup>3</sup> in its as-received condition. Using image analysis and quantitative x-ray diffraction-based phase identification, it was determined to consist of approximately 83 vol % TiC ceramic with 15 vol% of the nickel binder, and an average porosity of 1.6 vol%. Chemical analysis via inductively coupled optical emission and energy dispersive x-ray spectroscopy indicate the ceramic phase has a metal composition of 88% Ti, 11% Mo, and <1% Ni. Similar analysis of the binder gives a composition of 94% Ni, 5% Ti, and <1% Mo, respectively. The elastic modulus of the system

was determined to be 380 GPa via pulse-echo ultrasonic technique. The cermets measured compressive strength was 2.7 GPa but its bending strength was only 520 MPa, which is likely reconciled in terms of the characteristic flaws within the material.

The density and elastic moduli are well estimated by a rule of mixtures of the ceramic hard phase and the metallic binder properties. A computation of the theoretical density of the individual phases permits a calculation of the aggregate porosity level from the independently measured phase fractions. The elastic modulus of the cermet is nearly equivalent to that upper bound prediction computed based upon the moduli of pure TiC and Ni phases, but this may be a consequence of force chain formation.

The as-received cermet was discovered to undergo cracking during electro-discharge machining (EDM) of truss core shapes. X-ray diffraction measurements showed that a significant level of residual stress of  $165 \pm 15$  MPa was present in the TiC phase. Stress-relief annealing at  $900^\circ\text{C}$  with a subsequent cooling rate of  $15^\circ\text{C}/\text{min}$  was observed to relieve the stress to a value lower than the experimental uncertainty. Hot-isostatic-pressing at  $1270^\circ\text{C}$  (with a cooling rate of  $50^\circ\text{C}/\text{min}$ ) was found to increase residual stress, and it failed to reduce the porosity in the samples. No major differences between the microstructure and mechanical properties were observed following either the stress-relief or hot-isostatic pressed treatments.

Brazing with a Ni-Cr-P braze alloy was found to be an adequate cermet bonding method for assembly of a sandwich panel structure with a cermet truss core. Preliminary testing of brazed cellular unit cells revealed that failure occurs entirely in the base material, indicating that the brazed joint was not a limiting factor.

## ACKNOWLEDGEMENTS

I would like to express my deepest appreciation to all of the individuals who contributed to this thesis, as this work would not be possible without them. I would like to thank first and foremost my thesis advisor Sean Agnew for his guidance. His enthusiasm and expertise within the field of physical metallurgy combined with lots of meaningful conversations truly propelled the project. I would also like to thank Haydn Wadley for providing the vision for this project, as well as an unparalleled knowledge base that served as the starting point for this work. Without the support of these two individuals this thesis work would not have been possible.

I would also like to thank the past and present members of the Agnew research group at the University of Virginia: Mohammed Shamsujjoha, Dr. Peter Lekeaka-Takunju, Jishnu Bhattacharyya, Vincent Sloan, and Christopher Calhoun. These individuals not only assisted in some of the measurements, but also provided meaningful insight that provoked thought to develop substance within the discussions. Members of the Wadley Research Group at the University of Virginia also provided significant insight to this project. In particular Dr. Kumar Dharmasena, Mark O'Masta, Toni Kember, and Brad Richards all helped to guide some of the testing performed on the cermet. I would also like to express my special thanks to Dr. Liang Dong, who performed the parallel study of the brazed unit cell performance. The results from his work truly helped to provide significant context to this thesis, and provide me with some confidence that all of this detailed characterization may have some fruitful payoff.

Last but not least, I would like to thank my committee chair Elizabeth Opila for providing thoughtful comments on the overall work, as well as asking questions that helped to improve the overall quality of the thesis. I would also like to thank her student, Joe Hagan, for performing the inductively coupled plasma spectroscopy on the cermet at her recommendation.

## TABLE OF CONTENTS

ABSTRACT .....	i
ACKNOWLEDGEMENTS .....	iii
LIST OF FIGURES .....	vi
LIST OF SYMBOLS .....	xi
LIST OF TABLES .....	xiv
1. Introduction and Background .....	1
1.1. Motivation of research .....	1
1.2. Cermets .....	4
1.3. Research objectives .....	6
2. X-ray diffraction-based study of phase content, residual stress, and texture .....	8
2.1. Introduction .....	8
2.2. Experimental procedures .....	9
2.2.1. Qualitative phase identification .....	10
2.2.2. Quantitative phase identification .....	10
2.2.3. Crystallographic texture .....	12
2.2.4. Residual stress .....	13
2.3. Results .....	18
2.3.1. Phase content .....	18
2.3.2. Phase volume fractions .....	21
2.3.3. Crystallographic texture .....	23
2.3.4. Residual stress .....	24
2.4. Conclusions .....	27
3. Image based analysis of phase volume fractions and porosity .....	29
3.1. Introduction .....	29
3.2. Experimental procedure .....	29
3.2.1. Sample preparation .....	29
3.2.2. Phase volume fraction determination .....	31
3.3. Results .....	35
3.3.1. Microstructural characterization .....	35
3.3.2. Phase volume fraction and porosity .....	39
3.4. Discussion .....	40
3.5. Conclusions .....	41
4. Compositional Analysis of DDG-X Cermet tiles .....	43
4.1. Introduction .....	43
4.2. Experimental procedure .....	44
4.2.1. Inductively coupled plasma optical emission spectroscopy .....	44
4.2.2. Energy dispersive spectroscopy .....	45

4.3. Results.....	47
4.3.1. Overall chemistry.....	47
4.3.2. Phase-by-phase chemistry.....	48
4.4. Discussion.....	56
4.5. Conclusions.....	60
5. Mechanical properties of Ti(Mo)C-Ni cermets.....	62
5.1. Introduction.....	62
5.2. Experimental procedure.....	62
5.2.1. Pulse-echo ultrasonic measurement of elastic moduli.....	62
5.2.2. Hardness and Strength (Compressive and Flexural).....	65
5.2.3. Single edge v-notched beam fracture toughness testing.....	67
5.3. Results.....	70
5.3.1. Elastic moduli.....	70
5.3.2. Hardness and strength (compressive and flexural).....	72
5.3.3. Fracture toughness.....	76
5.4. Discussion.....	78
5.5. Conclusions.....	83
6. Joining of cermet structures using brazing.....	85
6.1. Introduction.....	85
6.2. Methods.....	86
6.3. Results and Discussion.....	90
6.4. Conclusions.....	93
7. Conclusions and Future Work.....	94
7.1. Conclusions.....	94
7.2. Future Work.....	96
APPENDICES.....	97
A. Hot isostatic pressing (HIP) pressure and temperature parameters.....	97
B. Example of Lorentzian and Gaussian fits used in image analysis.....	98
C. Quantile-quantile plot for particle size distribution analysis.....	100
D. Full porosity results for as-received and HIPed material.....	101
E. Full results for ICP and EDS analyses.....	102
F. Useful binary and ternary phase diagrams.....	103
G. Single Edge V Notch Beam notch radii.....	106
H. Uncertainty analyses for pulse-echo ultrasonic measurements.....	107
I. Hardness Values.....	108
J. Selected stress-strain curves from compression testing.....	110
K. Selected load-deflection curves from single edge v notch beam experiment.....	113
L. Vendor supplied properties of DDG-X cermet (Ti(Mo)C-Ni).....	115
M. Nanoindentation.....	116
REFERENCES.....	120

## LIST OF FIGURES

Figure 1: Ashby style plot of compressive strength vs. density. The grey unattainable material space is defined by the Hashin bound. The TiC/Ni cermet used in this study (shown by the black dot) has an expected compressive strength of 2 GPa and density of 5500 kg/m <sup>3</sup> . [5].....	2
Figure 2: Visual representation of combustion synthesis process .....	4
Figure 3: Bragg-Brentano geometry. In this scan, both $\theta$ and $2\theta$ are moved at the same rate. There is only one scan per sample, and the diffraction axis does not move.....	9
Figure 4: 2theta-omega geometry. Each scan is performed using the bragg-brentano geometry, but one residual stress measurement consists of a series of scans at different omega tilts. (a) shows the configuration for a scan at $\omega=0^\circ$ , and (b) shows the configuration for a scan at $\omega=-15^\circ$ .....	15
Figure 5: Example of a set of $\theta:2\theta$ scans for a $2\theta-\omega$ type scan. ....	15
Figure 6: Location of spatial residual stress measurements within the TiC phase. ....	17
Figure 7: X-ray diffraction patterns of DDG-X cermet tile. Each observed peak is marked with its reference phase – either titanium carbide or nickel. ....	19
Figure 8: Sample bragg-brentano scans of the first four peaks of the cermet in the as-received condition. The first two nickel peaks are observed to fluctuate greatly in repeat measurements in which the sample is moved. ....	20
Figure 9: Comparison of three quantitative phase identification methods. The black line (measured) is a reference line that each method is measured against.....	21
Figure 10: Calibration curve produced by external standard method. The measured intensity of the Ni (111) peak in the sample of interest is used to determine its weight percentage.....	22
Figure 11: Ni (200) pole figure. The plot shown is a 2-dimensional Schmidt plot with a normalized linear scale .....	23
Figure 12: TiC (111) pole figure. The plot shown is a 2-dimensional Schmidt plot with a normalized linear scale. ....	24
Figure 13: This figure shows the $d$ vs. $\sin^2 \omega$ behavior for TiC (511) peak at $2\theta=134.95$ with Cu radiation for positive (green) and negative (blue) $\omega$ tilts. 165 MPa of compressive stress is observed in this phase. ....	25
Figure 14: $d$ vs. $\sin^2 \omega$ behavior for TiC (511) peak at $2\theta=134.95$ with Cu radiation in the HIPed condition. 285 MPa of compressive stress is observed in this phase. ....	25

Figure 15: $d$ vs. $\sin^2 \omega$ behavior for TiC (511) peak at $2\theta=134.95$ with Cu radiation in the stress-relieved condition. No evidence of stress was found in this phase. ....	26
Figure 16: Representative histogram of pixels for each grayscale value where 0 is pure black and 255 is pure white. Notice the bimodal distribution, with a small percentage of black pixels as well.....	31
Figure 17: Example Gaussian fits for generated histogram of grayscale values (same as Figure 16 above). The areas underneath the Gaussian fits are used to estimate the volume percentage of each phase, and deduce the porosity. ....	32
Figure 18: Example of pseudo-Voight fits for generated histogram of grayscale values (Same as Figure 16 and Figure 17 above).....	33
Figure 19: (a) Example of SEM micrograph, and (b) its black and white conversion for estimation of porosity. ....	35
Figure 20: (Left) SEM micrograph of as-received DDG-X cermet tile, and (right) SEM micrograph of DDG-X cermet after undergoing HIP treatment. ....	36
Figure 21: Representation of variance of porosity with depth of the plate.....	37
Figure 22: Change in porosity observed with depth of plate...each increment is $600\mu\text{m}$ .....	38
Figure 23: Particle size distributions of as-received (left) and HIPed samples (right). ....	39
Figure 24: Graphical representation of theoretical basis of energy dispersive spectroscopy (EDS) [22]. ....	46
Figure 25: SEM Micrograph of total area examined for EDS broad spectrum. Total area is roughly $1200\mu\text{m}^2$ .....	49
Figure 26: EDS compositional analysis of entire microstructure .....	50
Figure 27: Binder and carbide probe locations .....	51
Figure 28: EDS compositional analysis of binder .....	51
Figure 29: EDS compositional analysis of carbide.....	52
Figure 30 : SEM Micrograph illustrating core-rim structure within carbide.....	53
Figure 31: Linescan across core-rim structure illustrating the change in molybdenum content. ...	54
Figure 32: SEM micrograph showing probe path for line scan analysis. ....	55
Figure 33: Line scan results showing change in metal composition over a span of $55\mu\text{m}$ . The titanium weight percentage can be used to track when the probe was within the carbide or binder phase. ....	55

Figure 34: Schematic of location of thickness measurements. ....	63
Figure 35: Schematic of experimental setup for ultrasonic elastic modulus measurements. ....	65
Figure 36: Schematic of fracture toughness sample geometry. All dimensions are in inches. ....	68
Figure 37: Optical images of the polished notch prior to testing. The radius at the notch tip is approximately 30 $\mu$ m. ....	69
Figure 38: Representative longitudinal waveform for an as-received sample. Waveform comes from sample AR3, and time of flight measurements are shown within. ....	70
Figure 39: Representative shear waveform for an as-received sample. Waveform comes from sample AR3, and time of flight measurements are shown within. ....	71
Figure 40: Compression test results for as-received (blue) and HIP (red) cermet conditions. ....	73
Figure 41: Measured flexural strength of cermet for as-received and heat treated condition. ....	74
Figure 42: Weibull distribution function overlaid with histogram data of the flexural strength testing. The red line indicates the probability of failure at the given stress level, and the dotted green line indicates a probability of survival of 37% (corresponds to the mean flexural strength). ....	75
Figure 43: Example SEM micrograph of fracture surface of bend beams after testing. ....	76
Figure 44: Fracture toughness values for all conditions. As-received, top, and bottom all come from different as-received plates. ....	77
Figure 45: Fracture surface of as-received DDG-X cermet. ....	78
Figure 46: Plot illustrating upper (Voight), lower (Reuss), and average (Hill) rule of mixture boundaries for elastic modulus. ....	80
Figure 47: Fracture toughness versus notch radii for all samples tested via single-edge v-notch beam method. ....	83
Figure 48: Graph of furnace temperature cycle for brazing of cermet to cermet with Nicrobraz © filler metal. ....	88
Figure 49: Assembly process of pyramidal truss structures assembled in a parallel study [35] ...	89
Figure 50: Representative images of the braze joints for the ground surfaces (left) and ...	90
Figure 51: Line scan analysis of EDM surface braze joint. The dark grey solids within the joint and within the binder are confirmed as Cr based particles. ....	91

Figure 52: Micrograph corresponding to line scan analysis in the above figure. ....	91
Figure 53: Stress-Strain response of cermet pyramidal lattice structure with relative core density of 4.97% (left), and image of failed sample (right). This testing was completed in a parallel study [35] .....	92
Figure 54: Ashby style plot of compressive strength vs. density. The grey unattainable material space is defined by the Hashin bound. The TiC/Ni cermet used in this study is shown by the black dot. The properties observed for the unit cell structure is shown by the red dot. [5].....	93
Figure 55: Temperature and Pressure parameters used in HIP run for DDG-X cermet tiles. ....	97
Figure 56: Example Pseudo-Voight profile fit.....	98
Figure 57: Gaussian portion of example pseudo-voight fit shown in Figure 56. ....	98
Figure 58: Lorentzian portion of example pseudo Voight fit shown in Figure 56. ....	99
Figure 59: Quantile-quantile plot for as-received particle size distribution .....	100
Figure 60: Quantile-quantile plot for HIPed particle size distribution .....	100
Figure 61: Titanium-molybdenum binary phase diagram [50].....	103
Figure 62: Titanium-carbon binary phase diagram [50].....	103
Figure 63: Titanium-nickel binary phase diagram [51] .....	104
Figure 64: Nickel-molybdenum binary phase diagram [52].....	104
Figure 65: Nickel-carbon binary phase diagram [54].....	105
Figure 66: Isothermal section of the titanium-molybdenum-carbon ternary phase diagram at 1400C. The ternary phases are based on the binary phases as follows: $\beta$ -( $\beta$ Ti,Mo); $\gamma$ -( $\beta$ Mo <sub>2</sub> C); $\delta$ -(TiC); $\eta$ -(MoC <sub>1-x</sub> ). [50] .....	105
Figure 67: Stress-strain curves for as-received specimens .....	111
Figure 68: Stress-strain curves for as-received specimens tested to failure .....	111
Figure 69: Stress-strain curves for HIPed specimens .....	112
Figure 70: Stress-strain curves for as-received specimens tested to failure .....	112
Figure 71: Sample load-deflection curves for as-received condition .....	113
Figure 72: Sample load deflection curve for as-received material from bottom of 18mm plate. ....	113
Figure 73: Sample load deflection curves for as-received material from top side of 18mm plate.....	114
Figure 74: Sample load-deflection curves for HIPed material. ....	114

Figure 75: Cross-comparison chart provided with as-received cermet tiles.....	115
Figure 76: SEM micrographs of indent on HIPed sample. (Left) showing evidence of (1) pileup in the binder (2) fracture within the carbide phase, (3) particle debonding from the binder, and (4) cleavage planes in the carbide phase after indenting. (Right) example of indentation exclusive to one phase. ....	118
Figure 77: Load vs. penetration depth charts for both the as-is and HIPed sample. ....	119
Figure 78: Modulus vs. depth data as captured via CSM measurement techniques. Striking differences are observed between the two phases.....	119

## LIST OF SYMBOLS

## Chapter 1

$I_0$	Material index which minimizes plastic deformation of a plate due to planar impact loading
$m_b$	Mass per unit area
$\sigma_Y$	Yield strength in compression
$\rho_m$	Material density
$c_0$	Wave speed in a medium
$E$	Elastic modulus
$Z$	Atomic number

## Chapter 2

$2\theta$	Diffracted angle, angle between the incident beam and the detector
$I_\gamma$	Diffracted intensity of $\gamma$ phase
$I_\alpha$	Diffracted intensity of $\alpha$ phase
$R_\gamma$	Constant for a given diffraction peak depending on crystallographic information for $\gamma$ phase
$R_\alpha$	Constant for a given diffraction peak depending on crystallographic information for $\alpha$ phase
$c_\gamma$	Volume fraction for $\gamma$ phase
$c_\alpha$	Volume fraction for $\alpha$ phase
$v$	Unit cell volume
$F_{hkl}$	Structure factor
$p$	Peak multiplicity
$M$	Temperature factor
$\phi$	Azimuth angle for texture measurements
$\chi$	Tilt angle for texture measurements
$\sigma$	Stress in the x-ray measurement direction
$E$	Young's modulus
$\omega$	Angle of tilt of the diffraction axis
$d_\omega$	Interplanar spacing measured at the angle $\omega$
$d_n$	Interplanar spacing measured at the angle $\omega=0$
$\psi$	Angle of tilt of the diffraction axis
$v_{Ni}$	Volume fraction of nickel phase
$v_{TiC}$	Volume fraction of titanium carbide phase
$\sigma_{Ni}$	Stress in the nickel phase
$\sigma_{TiC}$	Stress in the titanium carbide phase
$d_{hkl}$	Interplanar spacing for a given plane in the bulk solid
$I_Q$	Observed intensity of phase Q in a mixture
$I_{QP}$	Reference intensity of pure phase Q

## Chapter 3

$R^2$	Coefficient of determination
$L(x)$	Lorentzian function

$G(x)$	Gaussian function
$y_i$	Dependent variable
$I_0$	Scaling factor for pseudo-voight function
$\eta$	Lorentzian fraction of pseudo-voight function
$y_0$	Initial value of the dependent variable
$A$	Amplitude of the function
$x$	Independent variable
$x_C$	Center of function
$w$	Width of function

## Chapter 4

$Z$	Atomic number
$A$	Absorption correction factor
$F$	Fluorescence correction factor
$\rho$	Theoretical density
$n'$	Number of formula units per cell
$a_C$	Atomic mass of cation
$a_A$	Atomic mass of anion
$V_C$	Volume of unit cell
$N_A$	Avogadro's number

## Chapter 5

$d$	Plate thickness (elastic modulus measurements)
$\sigma_d$	Standard deviation for thickness measurements
$u_2$	Uncertainty in measurement due to repeatability
$u$	Overall uncertainty in measurement
$v$	Speed of wave in medium
$t$	Time of flight
$v_L$	Speed of longitudinal wave in medium
$v_T$	Speed of transverse wave in medium
$C_{11}$	Elastic constant from material stiffness matrix
$C_{44}$	Elastic constant from material stiffness matrix
$\rho$	density
$E$	Young's modulus
$\nu$	Poisson's ratio
$G$	Shear modulus
$HV$	Vickers hardness number
$F$	Indenter load
$d$	Average diagonal of Vickers indent
$P$	Break load
$L$	Outer span for four point-1/4 point flexure fixture
$b$	Specimen width
$d$	Specimen thickness
$K_I$	Fracture toughness
$P$	Load at fracture
$S$	Loading span

$Y$	Shape factor
$\alpha$	Geometric factor for crack, $a/W$
$a$	Crack length
$W$	Height of fracture toughness sample
$B$	Thickness of fracture toughness sample
$K_{IC}$	Plane strain fracture toughness
$P_s$	Probability of survival for a given volume $V_0$
$V_0$	Volume subject to load in flexural test
$\sigma$	Maximum tensile stress
$\sigma_0$	Weibull characteristic strength
$m$	Weibull modulus
$K_C$	Fracture toughness of composite
$E_C$	Elastic modulus of composite
$\nu_m$	Poisson's ratio of metal binder phase
$V_f$	volume fraction of metal binder phase
$K_m$	fracture toughness of metal binder phase
$\nu_c$	Poisson's ratio of composite
$\beta$	constant representing critical crack opening displacement divided by mean free binder path
$\sigma_{eff}$	effective flow stress of metal binder phase
$h$	mean free binder path

#### Chapter 6

$\sigma_c$	effective strength of unit cell structure
$\sigma_{strut}$	strength of base material of strut
$\bar{\rho}$	relative density
$\omega$	angle of inclination of unit cell struts

## LIST OF TABLES

Table 1: Candidate materials and their respective material indices which provide a comparison for expected performance with impulsive load mitigation. [5], [6].	3
Table 2: Compositions (in weight %) examined for quantitative phase identification.	11
Table 3: Key variables used within Rietveld refinement. Global variables apply to the entire pattern, and phase variables only apply to the peaks of the given phase.	12
Table 4: Optics and instrument settings utilized for crystallographic texture measurements.	13
Table 5: X'Pert diffractometer optics and instrument settings.	18
Table 6: TiC-NiMo bulk sample peak locations and intensities (experimental)	19
Table 7: Summary of phase volume fractions that were estimated by the direct comparison method, Rietveld refinement, and the external standard method.	22
Table 8: Residual stress values for positional scans.	26
Table 9: Nickel bonded titanium carbide polishing regimen.	30
Table 10: Lorentzian and Gaussian functions used within Pseudo Voight profile fit.	33
Table 11: Volume fractions for carbide, metal binder, and porosity as determined by image analysis.	40
Table 12: Summary of phase fraction results from chapter 2 and chapter 3	40
Table 13: Standard solutions prepared for ICP - OES analysis	45
Table 14: Average chemical composition of the DDG-X plates determined by ICP -OES	47
Table 15: EDS scan parameters	48
Table 16: EDS compositional analysis of entire microstructure	50
Table 17: EDS compositional analysis of binder.	51
Table 18: EDS compositional analysis of carbide	52
Table 19: Methods for calculating parameters used in theoretical density evaluation	57
Table 20: Atomic fractions and atomic mass values used in theoretical density calculation	57
Table 21: Average thickness values of samples, standard deviation and total experimental uncertainty (with 95% confidence level)	63
Table 22: Average longitudinal measured time-of-flight and uncertainty.	71
Table 23: Average shear measured time-of-flight and uncertainty	71
Table 24: Pulse- Echo Modulus results summary.	72

Table 25: Summary of mechanical properties obtained by compression testing.....	73
Table 26: Summary of fracture toughness results for all conditions .....	77
Table 27: Property summary for Ti(Mo)C-Ni cermet .....	81
Table 28: Polishing regimen for brazed joint samples.....	89
Table 29: Phase fraction and % porosity results for as-received material, complete with coefficient of determination for pseudo-voight profile fitting.....	101
Table 30: Phase volume fraction and % porosity results for HIPed sample, complete with coefficient of determination for pseudo-voight profile fitting.....	101
Table 31: Inductively Coupled Plasma results for as-received sample .....	102
Table 32: Second Run of Inductively coupled plasma results for as-received sample.....	102
Table 33: List of fracture toughness values measured, and corresponding notch radii .....	106
Table 34: Vickers microhardness measurements for as-received condition.....	108
Table 35: Vickers microhardness measurements for HIPed condition.....	109
Table 36: Compression testing complete results .....	110

# 1. Introduction and Background

## 1.1. Motivation of research

Edge clamped plates subjected to impulsive central loading resulting from impact with a solid or impingement of an air or water propagated shock front, suffer an out of plane deflection [2-4]. If the impulsive load is sufficiently small, such that the local stresses created in the plate do not exceed the yield or fracture strength of the plate material, the plate suffers only elastic transient (oscillatory) motion which dies out by damping. However, if the plate strength is exceeded by the localized loading, a permanent deformation of the plate is added to the elastic transient. In severe loadings, fracture of the plate can occur, either by petaling under the impacted region or by shear-off at the attachments.

For an edge clamped plate with thickness  $h$ , density  $\rho_m$ , and yield strength  $\sigma_Y$  that is subjected to center impulse loading, it was shown by Xue and Hutchinson [1] that maximizing a material index,  $I_0$  minimized the plastic displacement of the plate. They showed that

$$I_0 = \frac{1}{2} m_b \sqrt{\frac{\sigma_Y}{\rho_m}}$$

where  $m_b$  is the mass per unit area of the plate (i.e. the area density of the plate  $\rho_m h$  where  $\rho_m$  is the plate material density and  $h$  its thickness),  $\rho_m$  is the plate material density, and  $\sigma_Y$  is the yield strength of the plate material. This index has units of Pa-s, the same as those of specific impulse (momentum per unit area), and it has recently been shown [1] that the panel deflection dependence upon specific impulse scales with the  $I_0$  material property index for the plate material.

Figure 1 below shows an Ashby style plot of compressive strength and density. The material property index  $(\sigma_Y/\rho_m)^{1/2}$  can be used to select a viable option for an impulse resistant application. The triangle in the figure indicates the target range of properties for this application. The black datum point denotes monolithic TiC-Ni cermet, and the curves denote predictions of the strength vs. density for sandwich panels of different topologies, to be discussed below.

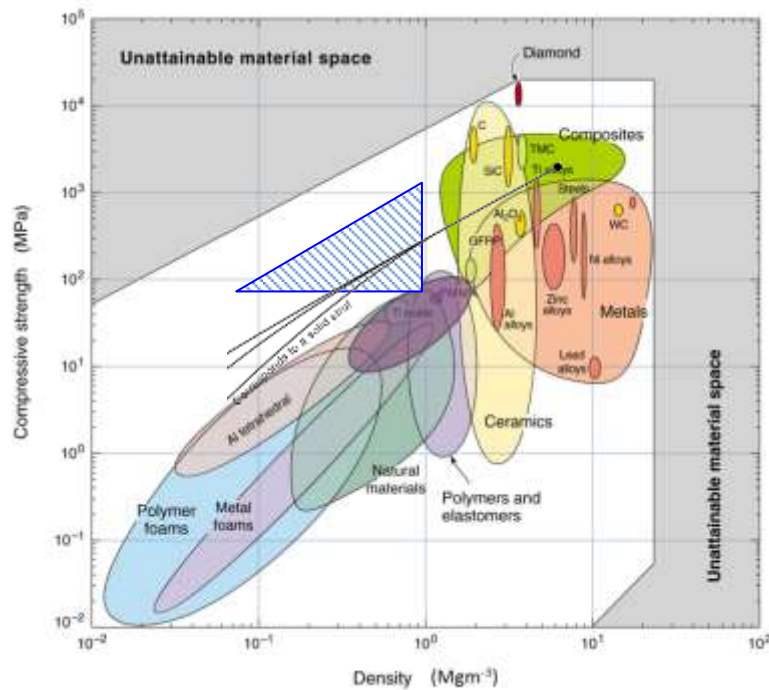


**Figure 1: Ashby style plot of compressive strength vs. density. The grey unattainable material space is defined by the Hashin bound. The TiC/Ni cermet used in this study (shown by the black dot) has an expected compressive strength of 2 GPa and density of 5500 kg/m<sup>3</sup>. [2]**

Table 1 below gives the material indices for a few candidate materials that could be considered for monolithic plates capable of mitigating impulsive loads. To date, high ductility stainless steels have primarily been used due to their ability to plastically deform and absorb the mechanical (impact) energy via a crushable core. However, nickel-bonded TiC is one system that stands out as a possibility with an exceptionally high material index ( $I_0 \approx .595$ ). High

performance (technical) ceramics with a superior merit index such as SiC or B<sub>4</sub>C are not viable candidates for this application because of their brittle nature. This cermet system is identified as viable due to its advertised fracture toughness of 20MPa·m<sup>1/2</sup>, making it significantly more durable than typical ceramics. This combination of properties makes the TiC/Ni cermet system a superior candidate for reducing deflection caused by impulsive loads.

**Table 1: Candidate materials and their respective material indices which provide a comparison for expected performance with impulsive load mitigation. [5-6].**

Candidate material	$\sigma_y$ (MPa)	$\rho_m$ (kg/m <sup>3</sup> )	$(\sigma_y/\rho_m)^{1/2}$	$K_{IC}$ (MPa·m <sup>1/2</sup> )	$I_0$
AL6XN SS	380	8060	0.217		54.25
17-4 PH SS (condition H900)	1170	7810	0.387	78	96.75
TiC/Ni-Mo Cermet	2000	5520	0.602	20	150.5
SiC	3410	3200	1.03	2.8	257.5
B <sub>4</sub> C	2760	2490	1.05	3	262.5

As shown by Wei et al, sandwich panels can offer an even further advantage, as they suffer smaller deflections than monolithic plates of the same areal density [3]. Specifically, Wadley et al showed through experimentation and simulation that the impulse transferred to a fully supported sandwich structure is with a compressible cellular core about 28% less than that transferred to a solid plate [4]. This arises because of the sandwich effect and in some cases a fluid structure interaction. When the fluid-structure interaction is weak, as in a mine blast loading by soil particles, the sandwich effect is the key to reducing deflection and this is maximized by using a strong core sandwich. The strength of a nickel bonded TiC cellular material offers a potentially superior option as a core material. This material offers a higher merit index than any other known metallic system. See the curves in Figure 1, based upon available property data for Ni-bonded TiC and the model of octet truss cellular material by Deshpande and Fleck [5], which permits obtaining new structures within the target property regime highlighted in blue.

Additionally, the advertised toughness of this system makes it attractive relative to pure ceramic options, which can boast even higher merit indices.

However, an extensive characterization of the cermet material must first take place before its viability can be assessed. Due to the composite nature of these materials, particular care needs to be taken to determine the effect of processing methods on the mechanical properties critical to this application. If detrimental effects exist, utilizing post-processing methods should also be explored to obtain the best properties possible.

## 1.2. Cermets

A common method for TiC cermet synthesis is via exothermic self-sustaining (combustion) synthesis, also referred to as self-propagating high-temperature synthesis (SHS) [6]. In this method, a green compact of the titanium and carbon powders are reacted in-situ with nickel powder in an inert atmosphere. Since this reaction is highly exothermic, once the heat of reaction for TiC synthesis is reached, the heat of formation propels the reaction of the rest of the heated powder. Figure 2 below shows a visual representation of the combustion synthesis process.

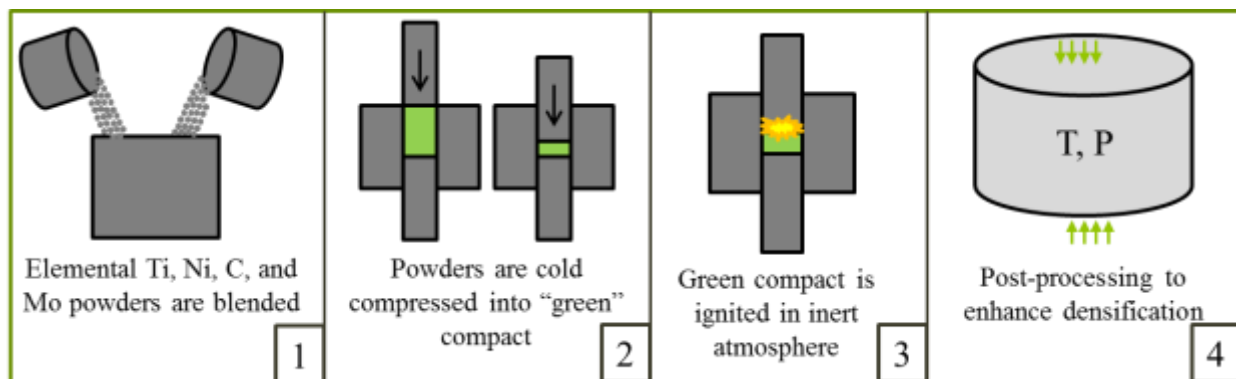


**Figure 2: Visual representation of combustion synthesis process**

In general this method is known to be cost efficient, but the result is a porous material – which is not desired for our applications. In order to obtain full (or near-theoretical) densification, SHS must be coupled with a pressure application process [6]. Multiple researcher groups have explored the applicability of hot isostatic pressing (HIP), quasi isostatic pressing (QIP), infiltration, and impact forging as potential densification methods [9-10]. One last precaution that applies is the possibility of contaminants and other impurities. Using high purity powders and a non-reactive atmosphere (either vacuum or argon) will help to keep this to a minimum. Large (100mm x 100mm x 6.3mm) tiles of a Ni bonded TiC cermet have been provided by the Davis Defense Group for the study conducted here. However, it is not known which method the vendors used to produce the cermet examined in this study. However, evidence will be provided which suggests that SHS was employed.

Another method employed to improve densification of TiC-Ni cermets in particular is through the addition of elemental molybdenum. LaSalvia et al have shown that replacing just 10 wt.% of the Ni binder phase can improve the wetting of the binder phase on the surface of the TiC particles necessary to achieve 100% contact between phases [7]. The increased wetting was shown to reduce microstructural defects and increase the transverse rupture strength, young's moduli, and fracture toughness. In that study the addition of Mo was also shown to insignificantly affect the Vickers microhardness of the material. The material studied contains Mo and so we investigate its distribution within the microstructure.

In order to assess the usability of the nickel bonded titanium carbide system in sandwich panel structures, an extensive characterization of the mechanical and chemical properties of the cermet must be completed. Again, little detail is known about the how the as-received condition of the cermet was reached from the supplier, so this characterization will provide some insight to

the process-structure-property relations that are of concern in this application. The as-received cermet tile was susceptible to fracture during cutting, leading to the speculation that either residual stresses are present (large enough to make the material more susceptible to fracture) and/or the fracture toughness may be lower than expected. As a result, some of the as-received cermet tiles were stress-relieved by heat treating in vacuum at 900°C for 30 minutes. The decision was made to compare the as-received mechanical properties with the stress-relieved condition. The as-received material was also compared to the HIPed condition (details in appendix A), which could possibly improve properties through stress-relief as well as densification. We also must recognize that the chemical composition will also have a major influence on the performance of the material. In particular, the ratio of TiC to Ni is crucial in determination of properties of the composite. Studies have shown that the addition of molybdenum and an increase in the metal fraction lead to improved fracture toughness [7]. Finally, in order to fabricate cellular materials from this cermet, simple methods must be available to produce and join the trusses or webs. It is currently unknown whether or not current metal bonding methods such as brazing of the cermet will work for the application in view. As such, this study will also investigate a brazing process.

### **1.3. Research objectives**

The applicability of the nickel-bonded titanium carbide cermet for use in sandwich panel structures is assessed as follows:

1. The microstructure of the nickel bonded titanium carbide cermet provided by the Davis Defense Group (hereafter DDG-X cermet) is characterized including the TiC particle size

distribution, ceramic and binder volume fractions, absolute and relative densities, and residual stress state.

2. The mechanical properties of the DDG-X cermet are assessed in the as-received, stress-relieved and hot isostatically pressed (HIPed) conditions. In particular, emphasis is placed on refining the parameters necessary for cellular material design and identifying opportunities for improvement of the core material.
3. The feasibility of using the nickel-bonded titanium carbide cermet in cellular structures is assessed by examining a cermet-cermet joining technique (brazing) and the behavior of a single unit cell of an octet truss sandwich is documented.

## **2. X-ray diffraction-based study of phase content, residual stress, and texture**

### **2.1. Introduction**

X-ray diffraction (XRD) is utilized throughout this study as a non-destructive tool to characterize the structure of the cermet. It proved to be particularly useful as an initial test to determine the phases present in the bulk solid, the volume fractions of the two phases, as well as their lattice parameters – which also then allowed the determination of the theoretical density of the solid. Each of these quantities is used in subsequent chapters as a means of comparison with methods that have a lower level of confidence - in particular, standardless x-ray microanalysis (Chapter 3), and a novel in-house image analysis technique developed by the author (Chapter 4). X-ray diffraction is also used to determine if there are any residual stresses present in either phase. Previous observations of fracture during machining have led to speculation that such stresses may exist and efforts to relieve it with a stress-relief anneal. If the residual stresses found are type I macro stresses, the presence of these stresses are of great concern, in particular when utilizing the DDG-X cermet tiles as the base material for cellular materials. In pursuing an octet truss design, it is already known that the structure will be stretch-governed. Since this type of design allows for the individual struts to primarily bear axial stresses, the compressive strength of the material can be exploited. However, the struts may also be subject to some bending stresses as well. Type I macro stresses decrease the amount of applied stress that the material can withstand before failure occurs. Considering the toughness of the cermet, residual stresses could be sufficient enough to promote cracking at a much lower stress than expected. If this happens within the individual struts, the overall strength of the structure would be weakened.

Finally, the possibility of crystallographic texture is assessed because a preferred orientation can affect the phase quantification and the residual stress assessments.

## 2.2. Experimental procedures

A Panalytical X'Pert MPD diffractometer equipped with a Cu  $K\alpha$  source was used to collect x-ray diffraction data for the DDG-X cermet tiles. For all qualitative and quantitative phase identification, Cu  $K\alpha$  radiation was employed using a standard Bragg-Brentano geometry ( $\theta:2\theta$ ) to collect the diffraction pattern on the  $2\theta$  range of  $30^\circ$ -  $110^\circ$ . A slit size of  $\frac{1}{2}$ " was used on both the incident and diffracted beam side, as well as soller slits with an angular allowance of  $0.18^\circ$ . The Panalytical X'Celerator detector, a real time multiple strip (RTMS) detector, was used to collect the diffracted beam. Figure 3 below depicts the general setup of the instrument for the Bragg-Brentano geometry used for the phase identification (slits not included).

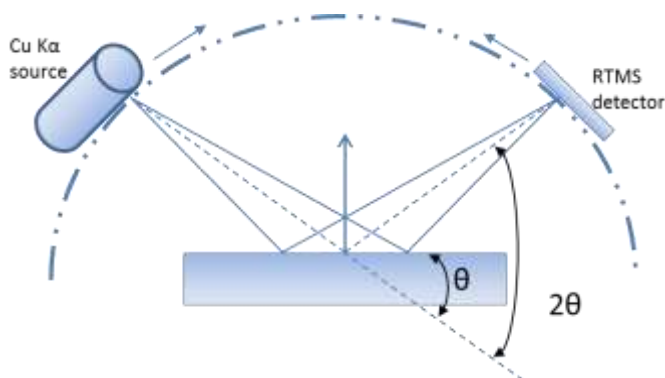


**Figure 3: Bragg-Brentano geometry. In this scan, both  $\theta$  and  $2\theta$  are moved at the same rate. There is only one scan per sample, and the diffraction axis does not move.**

### 2.2.1. Qualitative phase identification

The collected x-ray diffraction pattern for the cermet sample was analyzed using the Hi-Score© software by Panalytical. After using the software to define the  $2\theta$  position and intensity of each diffraction peak, the peak list is compared to experimental patterns contained in the Powder Diffraction File™ (PDF-4+) utilizing the Hanawalt search-and-match algorithm within Hi-Score to determine the constituent phases. The final PDF selections are manually selected from among the highest probability matches automatically selected by the software.

### 2.2.2. Quantitative phase identification

After the constituent phases are determined, the direct comparison method as outlined by Cullity [8] is used to determine the relative fraction of each phase. This method does not require a sample of the pure phases, but it does require that the lattice parameters and crystal structure of each phase is known. This information is obtained directly from the PDF files determined as a match for the observed nickel and titanium carbide phases. For a bulk material containing two phases,  $\alpha$  and  $\gamma$ , the ratio of diffraction peak intensities can be used to determine the phase fractions using the following relation [8]:

$$\frac{I_{\gamma}}{I_{\alpha}} = \frac{R_{\gamma}c_{\gamma}}{R_{\alpha}c_{\alpha}}$$

where  $c_i$  is the volume fraction of the  $i$ th phase and  $I_i$  is the diffracted intensity of a peak.  $R_i$  for each diffraction peak is a constant that depends on the crystal structure, and is given by:

$$R_{hkl} = \frac{1}{v^2} \left[ F_{hkl} p \left( \frac{1 + \cos^2 \theta}{\sin^2 \theta \cos \theta} \right) \right] e^{-2M}$$

where  $M$  is a temperature factor,  $F_{hkl}$  is the structure factor,  $p$  is the peak multiplicity, and  $v$  is the unit cell volume. Two other related methods, an external standard method and a basic Rietveld whole-pattern analysis are used to measure phase fractions for comparison.

The main result of the external standard method is a calibration curve that can be used to determine the weight percent of a given phase based on the intensity of a selected Bragg peak. This calibration curve is constructed by collecting an x-ray diffraction pattern for a series of different mixtures of pure titanium carbide and nickel powders. For each pattern, the planar spacing, peak location, relative peak intensity, and percentage by weight were recorded. Together, these patterns will be used to compare the input phase composition (by weight percentage), to the measured phase composition (by x-ray diffraction). Table 2 below displays the compositions used in developing the scale:

**Table 2: Compositions (in weight %) examined for quantitative phase identification.**

Case	reference	reference	1	2	3	4	5	6
<b>Wt. % TiC</b>	100	0	50	70	75	82	94	97
<b>Wt.% Ni</b>	0	100	50	30	25	18	6	3

The Rietveld refinement allows for a determination of the relative phase fractions without a dependence on a standard, or a calibration based on the experimental data. Prior to the refinement, the peaks are determined, and the full pattern is fit including the background and all peaks. The peaks are fit using Pseudo-Voigt functions. Then, the Rietveld function within Hi-score is utilized to conduct a non-linear least squares refinement on the full pattern based on user inputs for a set of free variables. Table 3 below describes the key variables used in the refinement. Specimen displacement and flat plate parameters are allowed to vary because of the condition of the surface of the as-received plates. The individual phase variables (unit cell

dimensions, zero shift) are allowed to vary because of the suspected solid solution elements within the phases. Finally, the scale factor is allowed to vary, as it is the main variable of a Rietveld refinement which compares the observed intensities to the normalized intensity for one unit cell.

**Table 3: Key variables used within Rietveld refinement. Global variables apply to the entire pattern, and phase variables only apply to the peaks of the given phase.**

<b>Variable type</b>	<b>Name of Variable</b>
<b>Global Variables</b>	Specimen displacement (Z height)
	Flat plate (surface roughness)
<b>Phase Variables</b>	Unit cell dimensions
	Zero shift
	Scale factor

### 2.2.3. Crystallographic texture

Although no strong texture is expected in this powder processed material, the presence of texture would have a strong bearing upon the measurement and quantitative analysis of phase fractions and residual stress (described in the next section), that it was decided to explore for the possible presence of texture in both the TiC and the Ni-binder phases.

Incomplete pole figures were collected using the (200) peak for the Ni binder. In order to perform the measurement, the x-ray source must first be turned 90° within its casing in order to ensure that it is set up to use the point source window. Once it is set up, the beam height is realigned such that the center of the beam is centered along the goniometer axis. Next, the incident beam optics must be replaced with the cross slits. In this case, 2mm x 2mm cross slits are used in order to create the largest incident area possible while remaining on the sample. On the diffracted beam side, a parallel plate collimator (PPC) along with a 0.18” PPC slit is used to

restrict the accepted divergence of the diffracted beam. Last but not least, the proportional detector is used to collect the diffracted beam. The full setup is summarized in Table 4 below.

**Table 4: Optics and instrument settings utilized for crystallographic texture measurements.**

<b>X-ray source</b>	
Radiation	Cu K $\alpha$
Power Settings	45kV, 40mA
Focus	Point Focus
<b>Incident beam optics</b>	
Cross-slits	2mm x 2mm
K $\beta$ filter	Nickel (Cu)
<b>Divergent beam optics</b>	
Receiving slit	.18"
Parallel plate collimator	.5"
<b>X-ray detector</b>	
Proportional Detector	

The pole figure data were collected on a 5 x 5 degree grid of  $\phi$  (azimuth) and  $\chi$  (tilt) from 0-355° and 0-80°, respectively. In order to achieve these geometric positions, an open Eulerian cradle stage is used to hold the sample. The possibility of defocusing with tilt was explored using a completely random titanium powder sample. It was confirmed that the intensity remained constant up to a tilt angle  $\chi = 55^\circ$ . In the event that orientation distribution functions or complete pole figures were required, defocusing correction could be implemented using this defocusing data. The background intensity was corrected for by collecting the background at a  $2\theta$  position before and after the diffraction peak and then subtracted from the peak intensity measured at each tilt position explored.

#### **2.2.4. Residual stress**

Assuming a plane stress condition, the residual stress on the surface can be characterized by measuring the lattice strain along a chosen direction. Experimentally this is measured as the

change in interplanar spacing within the crystal lattice as evidenced by a shift in the  $2\theta$  peak position at various planes in the specimen containing the direction of measurement. The main result for this method is a factor defining the change in the interplanar spacing measured with the change in the sample tilt. It can be shown that this factor can be used to calculate the stress in the measurement direction with the equation [9]:

$$\sigma = \frac{E}{(1 + \nu) \sin^2 \omega} \left( \frac{d_\omega - d_n}{d_n} \right)$$

where  $\omega$  is the angle of tilt of the diffraction axis,  $d_\omega$  is the interplanar spacing at the angle  $\omega$ , and  $d_n$  is the interplanar spacing at  $\omega = 0^\circ$  [10].  $E$  and  $\nu$  are the elastic modulus and Poisson's ratio, respectively. The slope of the  $d$  vs.  $\sin^2 \omega$  plot is equal to the value of  $\frac{d_\omega - d_n}{\sin^2 \omega}$ .

This data is obtained through a  $2\theta$ - $\omega$  type measurement on the X'pert diffractometer. This measurement utilizes the geometry shown in Figure 4 below to complete  $\theta:2\theta$  scans at different  $\omega$  offsets (also known as  $\psi$  tilts) to measure the location of the peak of interest. Figure 5 on the next page gives an example of the output data that is obtained from the  $2\theta$ - $\omega$  scan. From these data, the change in interplanar spacing can be measured.

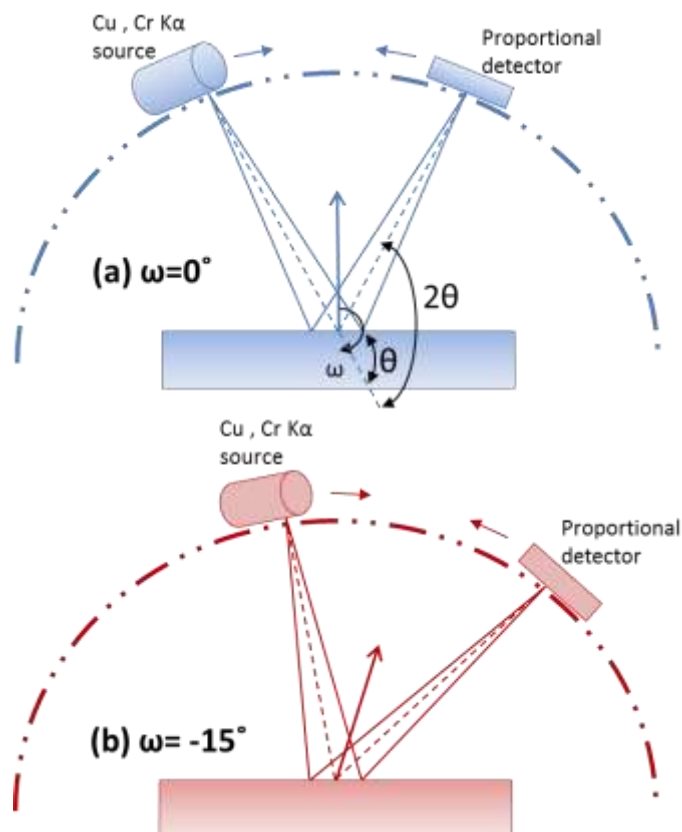


Figure 4: 2theta-omega geometry. Each scan is performed using the bragg-brentano geometry, but one residual stress measurement consists of a series of scans at different omega tilts. (a) shows the configuration for a scan at  $\omega=0^\circ$ , and (b) shows the configuration for a scan at  $\omega=-15^\circ$ .

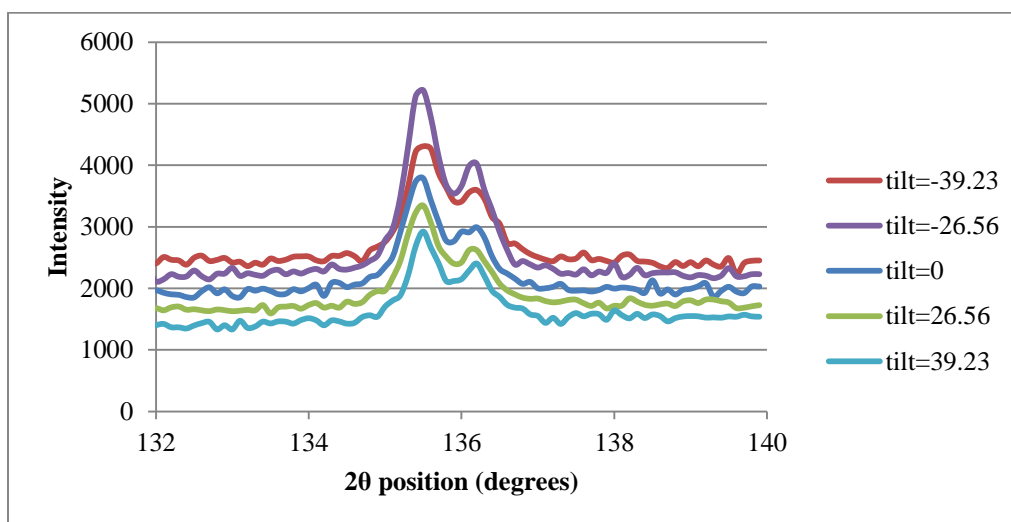


Figure 5: Example of a set of  $\theta:20$  scans for a  $20-\omega$  type scan.

In order to obtain a peak at a suitable  $2\theta$  position to reduce experimental error, the TiC phase was evaluated with Cu  $K\alpha$  (1.54 Å), and the Nickel phase was evaluated with Cr  $K\alpha$  (2.29Å) radiation [10]. The optics are presented in Table 5. It is important to note that the nickel phase peak is below the recommended  $2\theta$  threshold of evaluation, even with the chromium source ( $2\theta=80^\circ$ ). Normally, this angle would be a point of concern due to the uncertainty in  $2\theta$  approaching the magnitude of the shift in  $2\theta$  due to residual stress. In the case of measurable residual stress in the titanium carbide phase however, the nickel phase is expected to exhibit a significantly higher stress. A simple upper-bound rule of mixtures calculation can be used to illustrate this concept using the typical ceramic to matrix ratio of 4 in metal bonded ceramics (assuming 80% ceramic 20% metal).

$$\sigma_{total} = v_{Ni}\sigma_{Ni} + v_{TiC}\sigma_{TiC}$$

$$v_{Ni}\sigma_{Ni} = -v_{TiC}\sigma_{TiC}$$

$$\sigma_{Ni} = -\frac{v_{TiC}}{v_{Ni}}\sigma_{TiC}$$

$$\boxed{\sigma_{Ni} = -4 \sigma_{TiC}}$$

Given the difference in thermal expansion coefficients of the ceramic (7.70  $\mu\text{m}/\text{m}^\circ\text{C}$ ) and binder (13.1  $\mu\text{m}/\text{m}^\circ\text{C}$  [11]), it is anticipated that the stress will be compressive in the TiC phase and tensile in the Ni phase. Despite the fact that the stress in the Ni phase is expected to be much larger, the small phase fraction and large grain size prevented its assessment. All the techniques mentioned above were utilized to assess the Ni (111) peak, for both Cr and Cu radiation. The slit sizes on the optics were changed to obtain the maximum irradiated area on the sample. Chi tilt measurements were also performed in order to have more options for tilt and even azimuth to find a measurement area where the nickel peak could be observed. Every experiment yielded either a peak at a single tilt value or no peaks at all, which prevented a

measurement of the change in interplanar spacing. This constitutes an inconclusive result since the Over 100 scans were performed to no avail.

In order to examine the DDG-X material for the presence of macro stresses, the stress in the titanium carbide phase is measured in multiple locations on the as-received material. If a variation in stress for a particular phase is spatially dependent, that will indicate that type I macro stresses are present. Figure 6 below shows the three spatial scans accomplished. Each scan was within a single quadrant of the full tile, and the irradiated area for each scan was approximately 1 inch apart. The reason for only examining one quadrant was the assumption that the symmetry of the shape and powder pressing processes would result in symmetry in the residual stress profile.

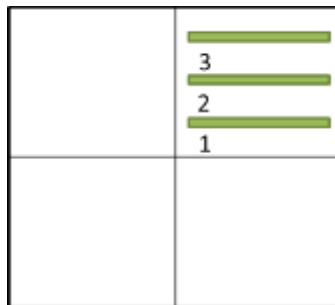


**Figure 6: Location of spatial residual stress measurements within the TiC phase.**

**Table 5: X'Pert diffractometer optics and instrument settings.**

<b>X-ray source</b>	
Radiation	Cu K $\alpha$ Cr K $\alpha$
Power Settings	45kV, 40mA (Cu) 55kV, 30mA (Cr)
Focus	Line Focus
<b>Incident beam optics</b>	
Soller Slits	.18"
Divergence slit (Cr only)	.5"
Parabolic Cu mirror (Cu only)	.18"
Width mask	10mm
<b>Divergent beam optics</b>	
Soller slits	.18"
Anti-scatter slit	.5"
K $\beta$ filter	Nickel (Cu) Vanadium (Cr)
<b>X-ray detector</b>	
Proportional Detector	

## 2.3. Results

### 2.3.1. Phase content

The x-ray diffraction pattern in Figure 7 below is representative of the DDG-X cermet tile. Given this pattern, the bulk sample is observed to contain both a titanium carbide (PDF #04-002-0405) phase and a nickel (PDF# 04-005-1701) phase, with no additional phases observed above the detection limit.

Table 6 shows the indexing of the peaks observed.

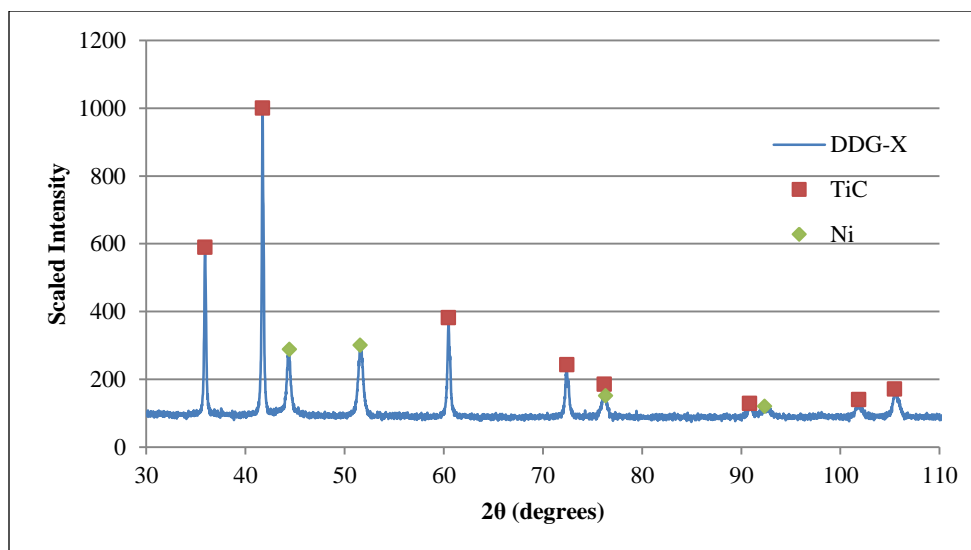


Figure 7: X-ray diffraction patterns of DDG-X cermet tile. Each observed peak is marked with its reference phase – either titanium carbide or nickel.

Table 6: TiC-NiMo bulk sample peak locations and intensities (experimental)

Angle (degrees)	$d_{hkl}$ (Å)	Scaled Intensity	Plane involved
35.92°	2.497	590	TiC (111)
41.73°	2.162	1000	TiC (200)
44.42°	2.037	290	Ni (111)
51.58°	1.770	300	Ni (200)
60.48°	1.529	382	TiC (220)
72.41°	1.304	244	TiC (311)
76.17°	1.248	185	TiC(222)
76.33°	1.246	151	Ni(220)
90.85°	1.081	129	TiC (400)
92.35°	1.067	120	Ni (311)
101.83°	0.992	140	TiC (331)
105.45°	0.968	172	TiC (420)

Based on current literature for TiC cermets with a Ni matrix, very small amounts of molybdenum could have been added (<3wt%) in order to promote the wetting of Ni on the TiC surface. No molybdenum solid solution, other binary, ternary or quaternary phases are observed within the detection limits of this scan. This absence of a bcc Mo phase is not surprising, since

TiC has significant solubility for Mo, and Ni has a small amount of solubility for Mo. The Ni does have a significant solubility for Ti. In the carbide, Mo can substitute for Ti up to 10 weight percent [7]. This is consistent with the collected diffraction patterns, as the peaks for both phases are shifted in agreement with the principle of Vegard's law [12] when compared to the corresponding PDFs. Further studies are conducted in chapter 4 to obtain a more robust analysis of the chemistry. Application of Vegard's law was not conducted.

Upon repeat measurements, it was observed that the nickel peaks fluctuated greatly in intensity. In some cases they could not even be detected above the background. Figure 8 below gives examples of how the nickel peak relative intensities fluctuated for a single sample when the sample position on the stage is shifted. This indicates that the Ni has a very large grain size. No metallographic preparation was found which could prove or refute this hypothesis.

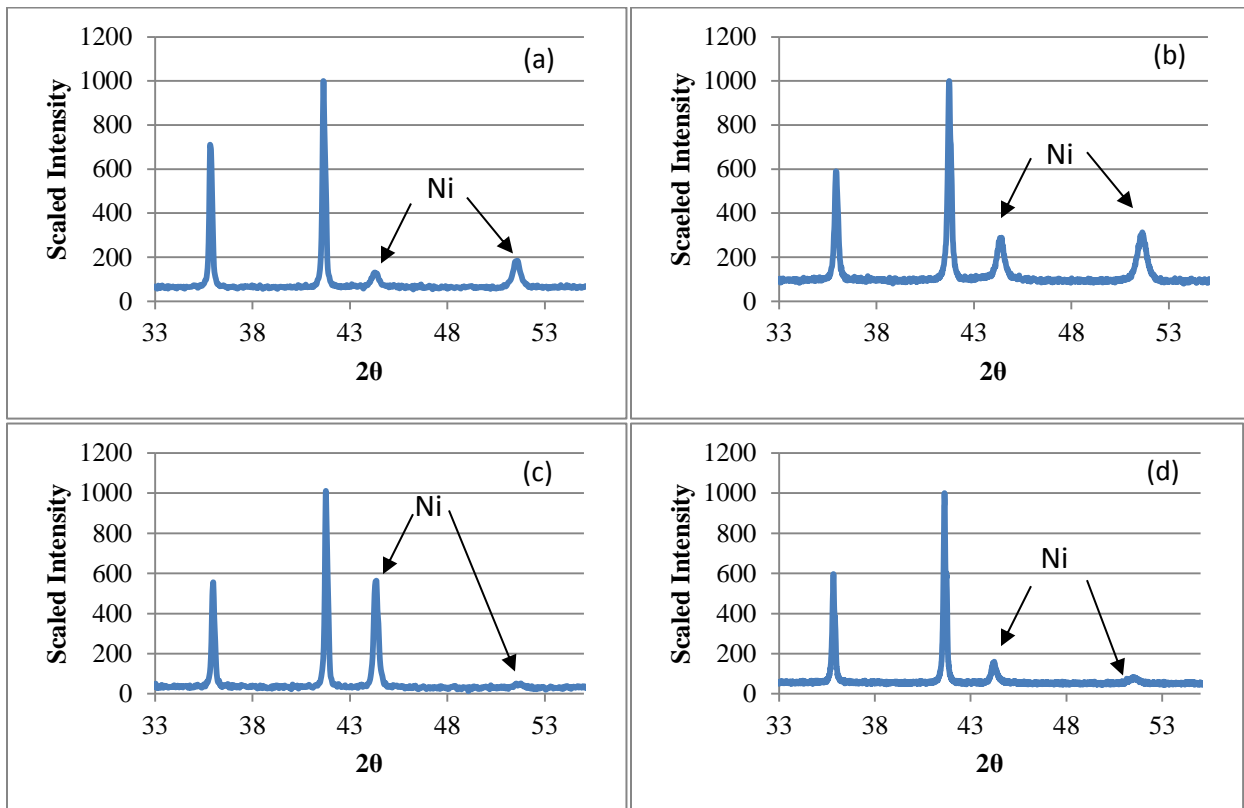


**Figure 8: Sample bragg-brentano scans of the first four peaks of the cermet in the as-received condition. The first two nickel peaks are observed to fluctuate greatly in repeat measurements in which the sample is moved.**

### 2.3.2. Phase volume fractions

Prior to evaluating the DDG-X cermet tiles, the three methods explored were compared to determine the most accurate option for evaluation given the instruments available. Figure 9 below shows the evaluation of the three methods. Each of the three methods utilized proved to be acceptable in their respective analyses, but statistically, the direct comparison method was determined to be the most accurate. Values shown in the graph below are in volume percent.

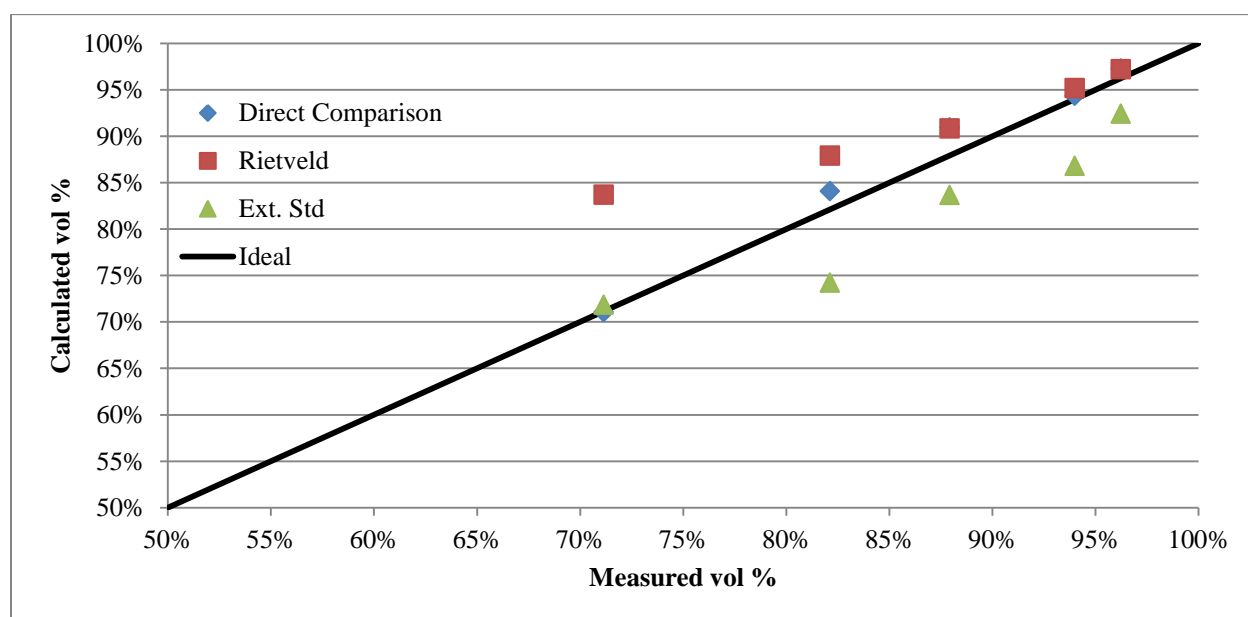


**Figure 9: Comparison of three quantitative phase identification methods. The black line (measured) is a reference line that each method is measured against.**

When applied to the DDG-X cermet tile, the direct comparison method, utilizing the (111) peak intensities from both phases, revealed that the relative phase volume fractions for titanium carbide and nickel are 0.82 and 0.18, respectively. The external standard method was used to develop the calibration curve presented in Figure 10 below. The curve is used to estimate

the volume fraction of Ni in the cermet as 0.19 based on the measured intensity of the Ni (111) peak. Lastly, the Rietveld refinement performed estimated a nickel volume fraction of 0.16. A summary of these results can be found in Table 7 below.

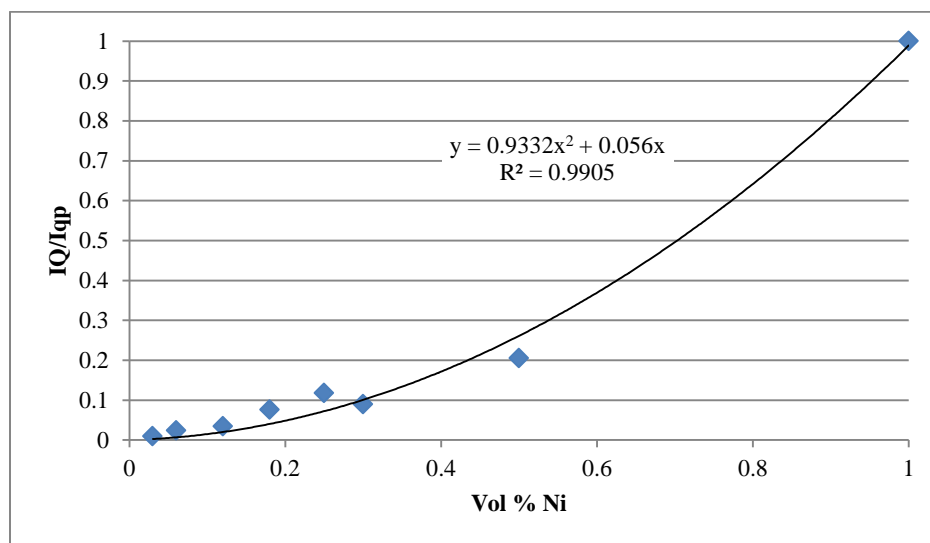


**Figure 10: Calibration curve produced by external standard method. The measured intensity of the Ni (111) peak in the sample of interest is used to determine its weight percentage.**

**Table 7: Summary of phase volume fractions that were estimated by the direct comparison method, Rietveld refinement, and the external standard method.**

Method	TiC	Ni
Direct Comparison	.82	.18
Rietveld	.84	.16
External Standard	.81	.19

The given results have revealed that the DDG-X cermet is a two phase material with titanium carbide and nickel. With the given phase content determined in section 0, the literature suggests that molybdenum or another wetting element would have been added to the mixture to improve the bonding between the phases, thereby improving the density [7]. Without Mo, the observed density was very poor. This is consistent with the minor shift in the position of the Bragg peaks.

In chapter 3, the chemistry of individual phases will be determined, permitting theoretical density calculations. In chapter 4, volume fractions will be assessed by image analysis. Subsequently, it will be possible to compare the phase fractions and porosity levels indicated by different techniques.

### 2.3.3. Crystallographic texture

Both the TiC and the Ni phases were revealed to be essentially randomly textured (see Figure 11 and Figure 12 below). The Ni phase was also revealed to be coarse grained, which manifests itself as “spottiness” in the (200) pole figure presented below.

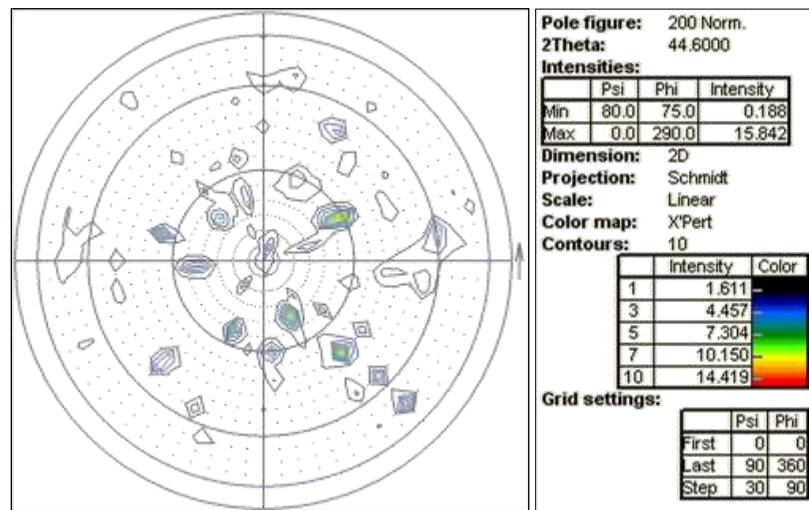
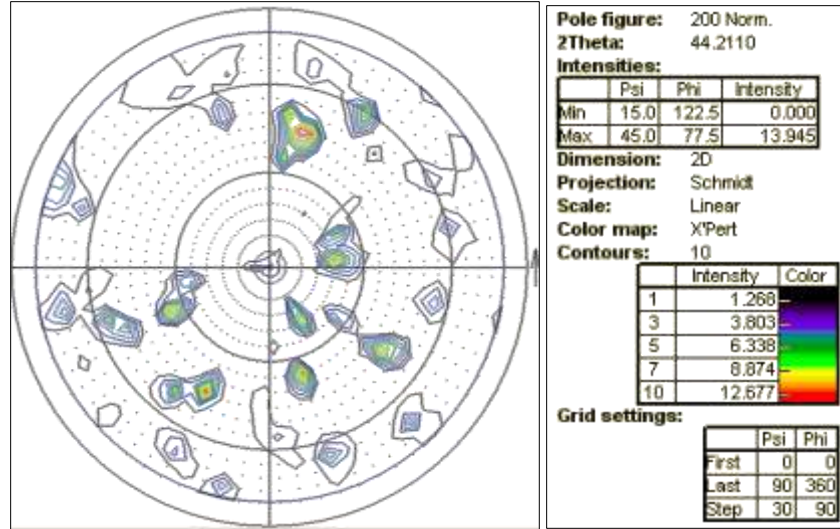


Figure 11: Ni (200) pole figure. The plot shown is a 2-dimensional Schmidt plot with a normalized linear scale



**Figure 12: TiC (111) pole figure. The plot shown is a 2-dimensional Schmidt plot with a normalized linear scale.**

#### 2.3.4. Residual stress

Figure 13 below shows the change in interplanar spacing for the TiC (511) peak with a change in  $\omega$  tilt. From this data, the equation introduced in section 2.2.3 is used to calculate the stress to be 165 MPa in compression at the center of the entire as-received plate. The two other locations mentioned previously in section 2.2.3 all produced the values of residual stress within the experimental uncertainty, leading to the conclusion that there are no macro-stresses. Figure 14 and Figure 15 below show the results for the HIPed and stress-relieved conditions, respectively. The stress measured in the HIPed condition reveals a compressive stress of 285MPa – much higher than in the as-received material. Since the HIP cycle used reached a maximum temperature of 1250°C, it is likely that the difference in coefficient of thermal expansion between the two phases caused thermal stresses to form during cooling. Details of the entire HIP cycle can be found in appendix A. The stress-relieved condition was found to have a negligible magnitude for residual stress, as it was below the error in the measurement itself.

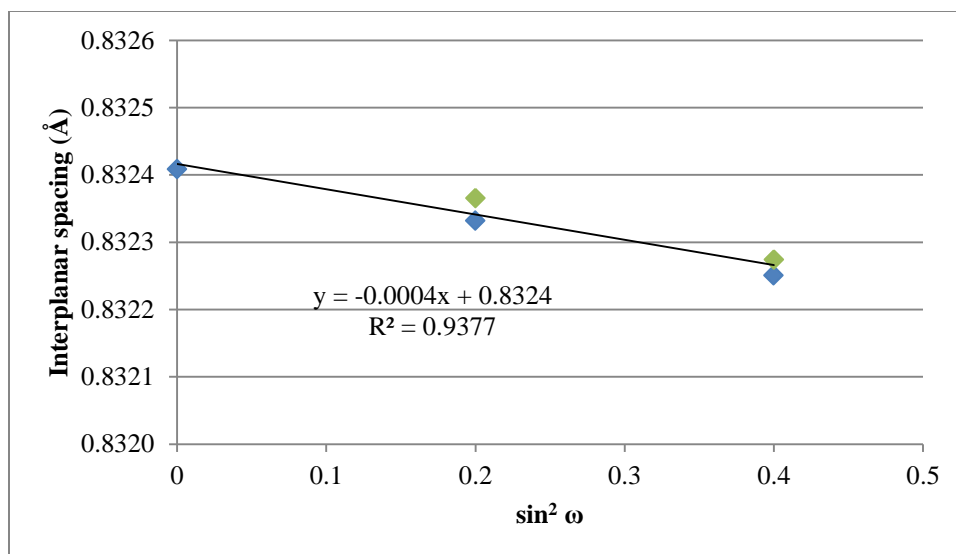


**Figure 13:** This figure shows the  $d$  vs.  $\sin^2 \omega$  behavior for TiC (511) peak at  $2\theta=134.95$  with Cu radiation for positive (green) and negative (blue)  $\omega$  tilts. 165 MPa of compressive stress is observed in this phase.

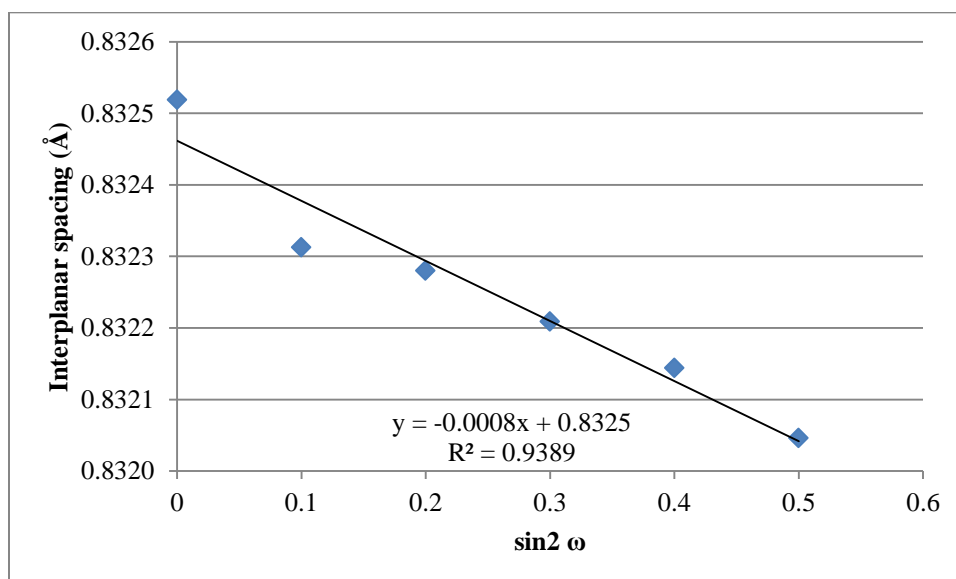


**Figure 14:**  $d$  vs.  $\sin^2 \omega$  behavior for TiC (511) peak at  $2\theta=134.95$  with Cu radiation in the HIPed condition. 285 MPa of compressive stress is observed in this phase.

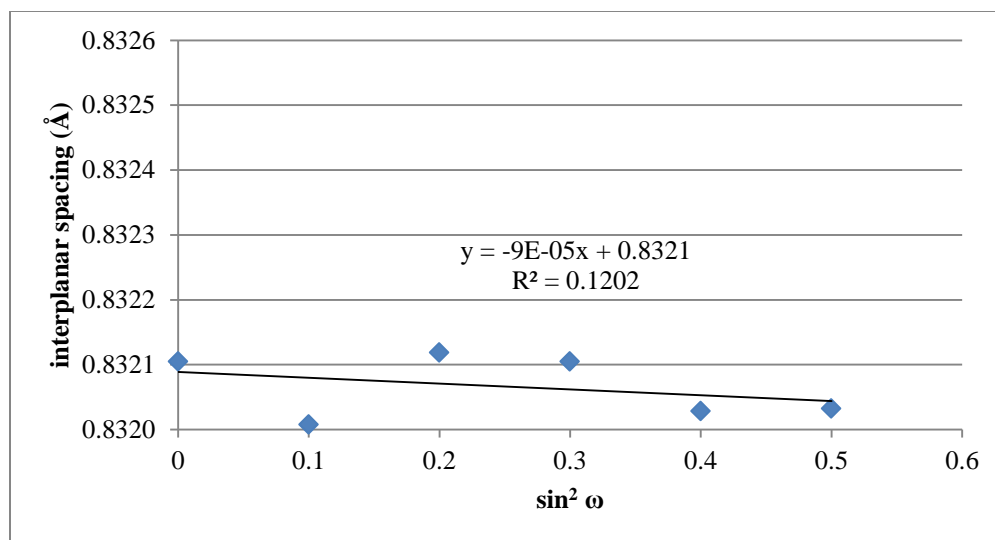


**Figure 15: d vs.  $\sin^2 \omega$  behavior for TiC (511) peak at  $2\theta=134.95$  with Cu radiation in the stress-relieved condition. No evidence of stress was found in this phase.**

The positional measurements obtained revealed that type I macro stresses are not present within the as-received tiles, although there is significant variation in the results from one position to another. As mentioned in 2.2.4, three positional scans were completed in order rule out the possibility in positional variance in the residual stress. Table 8 below shows the residual stress values measured for three positions across the as-received plate. Note that the average value obtained for this set of experiments is equivalent to the single measurement shown above.

**Table 8: Residual stress values for positional scans.**

Scan position	Residual stress (MPa)	R <sup>2</sup> value
1	-147	.753
2	-224	.852
3	-126	.936
Average	-166	n/a

## 2.4. Conclusions

The results obtained from the methods employed in this chapter allow the following conclusions to be made:

- All diffracted peaks are attributed to two phases present within the cermet – titanium carbide (TiC) and nickel (Ni). No other phases are detected above the background radiation.
- A systematic shift in the peaks of both the TiC phase and Ni phase suggests that there are elements in solid solution within both of the phases. These assertions are supported by the analysis presented in the subsequent chapter on chemical analysis.
- Although the texture analysis did not reveal the presence of crystallographic texture, it did make it apparent that there are likely very large grains of the nickel phase, which explains the fluctuation in the observed intensity of the nickel (111) peaks between different scans.
- The fluctuation observed in the Ni (111) peak could also affect the phase volume fractions as measured by the direct comparison method. The Rietveld method and external standard methods should not be as vulnerable, as they utilize multiple peaks for the analysis.
- There is a measurable residual stress in the TiC phase of  $-165 \text{ MPa} \pm 15 \text{ MPa}$ .
- The Ni phase presumably has a large tensile residual stress in the as-received condition, based upon the requirements for equilibrium. However, due to the large grain size, it was not possible to irradiate enough nickel at the tilt values needed to measure residual stress. The use of a poly capillary X-ray lens or neutron diffraction would be required.

- After the stress-relief heat treatment, the residual stress in the TiC was reduced to an immeasurably low value (i.e. less than experimental uncertainty 15 MPa).
- After the hot isostatic pressing, the stress in the TiC increased to a value of  $-324 \text{ MPa} \pm 15 \text{ MPa}$ . This is likely the result of thermal stresses forming during the cooling part of the HIP process, as the cermet was cooled at a rate of  $50^\circ\text{C}/\text{min}$ .

### **3. Image based analysis of phase volume fractions and porosity**

#### **3.1. Introduction**

Controlling the microstructure is one of the most potent means by which the materials engineer can control the properties of a material. Since cermets are composites consisting of a hard phase embedded in a metal binder, its mechanical properties are particularly sensitive to changes in volume fraction of the phases. With the DDG-X cermet in particular, the contrast in properties of the carbide and metal phases makes properties such as thermal conductivity, fracture toughness, hardness, wear resistance, and elasticity highly dependent on the relative fraction of the hard phase to the binder. The carbide particle size distribution within the metal matrix has also been shown to influence properties such as hardness and toughness of the cermet. In particular it was shown that a finer grain size can decrease the toughness, because it decreases the mean free path in the binder [13].

#### **3.2. Experimental procedure**

##### **3.2.1. Sample preparation**

Samples of the cermet tile about 10mm x 10mm were sectioned from the as-received DDG-X cermet tile with a low speed saw equipped with a diamond blade. Once sectioned, each sample is mounted in a 3 cm diameter cylindrical mount composed of Konductomet ©, and polished using the regimen shown in

Table 9 below.

**Table 9: Nickel bonded titanium carbide polishing regimen**

<b>Grinding/Polishing Disc</b>	<b>Grit Size</b>	<b>Time polished (min)</b>
<b>MD Piano</b>	220	1:30
<b>MD Piano</b>	500	1:30
<b>MD Piano</b>	1200	1:30
<b>MD-Allegro</b>	9 $\mu$ m	1:30
<b>MD-DAC</b>	9 $\mu$ m	4:00
<b>MD-DAC</b>	3 $\mu$ m	4:00
<b>MD-DAC</b>	1 $\mu$ m	4:00
<b>MD-CHEM</b>	.25 $\mu$ m	4:00

It must be noted that the grinding discs utilized in steps 1-3 are all diamond impregnated. The grit size noted is comparable to the grit size of standard SiC grinding discs. However, the SiC discs were found to be completely ineffective in grinding the cermet due its overall hardness – in particular the high hardness of the TiC phase.

After polishing, the samples are imaged within a scanning electron microscope with a beam voltage of 20 keV and a probe current of .03 nA. Note that no etching procedure was required. The average atomic number of the two phases is so different that there is strong contrast between the phases [14]. This is why scanning electron microscopy was employed, even though the level of magnification employed is easily obtained with optical microscopy. The contrast in the optical microscope images is vastly inferior for this application. All images are collected at a magnification of 400x, and a focal working distance of 10.7 mm. This makes the sampling area of each image approximately .012 mm<sup>2</sup>. After the micrographs are collected, they are inspected to ensure that there is no polishing damage present. A random sampling of 15 micrographs was collected from each specimen to be used in analysis described below.

### 3.2.2. Phase volume fraction determination

For this study, all images were collected with the secondary electron signal via a scanning electron microscope (SEM). Even though this imaging technique is less sensitive than back-scattered electron imaging, even secondary electron yield has a weak dependence upon atomic number [14]. Thus, the grayscale of the SEM micrograph can be related to the average atomic number ( $Z$ ) value of the sample's constituent elements, and the micrographs can be used to distinguish between the phases based on their gray scale value provided there is a large enough difference between the average  $Z$  values of the two phases. The images presented in this chapter will demonstrate that this is indeed the case for TiC vs. Ni binder.

Utilizing the freeware program UTHSCSA ImageTool ©, the pixels in each image were parsed into number values that represented its place on the grayscale (from perfectly black, 0, to pure white, 255). Next, the data was represented as a histogram, to show how many pixels belong to a particular value on the grayscale. Figure 16 below shows an example of the histogram obtained from the micrograph shown.

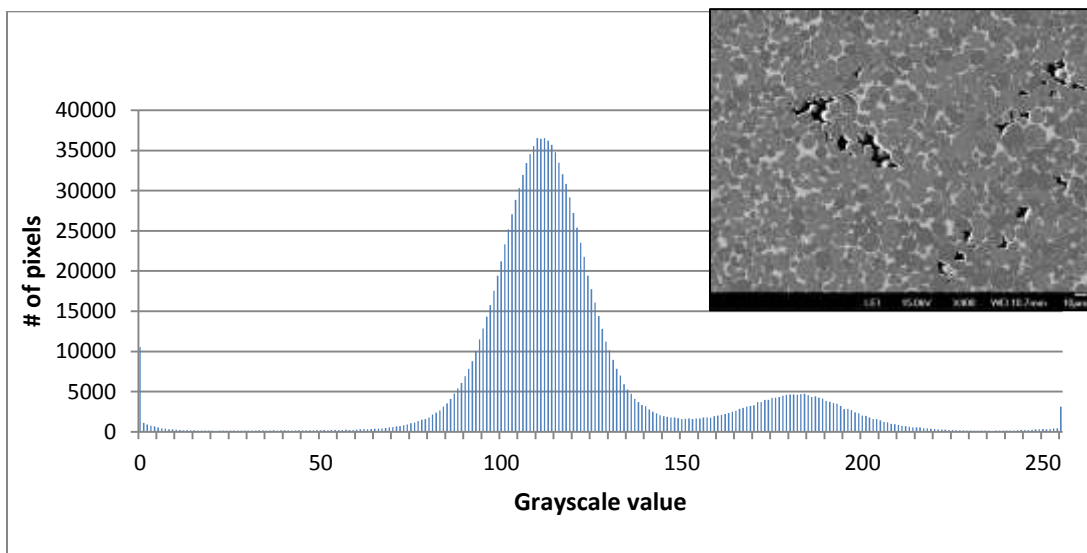


**Figure 16: Representative histogram of pixels for each grayscale value where 0 is pure black and 255 is pure white. Notice the bimodal distribution, with a small percentage of black pixels as well.**

Once the data is parsed into a histogram, it is observed that the pixels fall into a bimodal distribution. The two gray scale modes correspond to the low Z dark phase titanium carbide, and high-Z binder phases observed, respectively. We can deduce that the mode with the lower grayscale value represents the carbide phase, and the other mode represents the binder.

In order to determine the number of pixels that represent each mode, the profiles must first be fit. In considering each mode separately, a Gaussian function is used to represent the shape of the distribution, as shown in Figure 17 below.

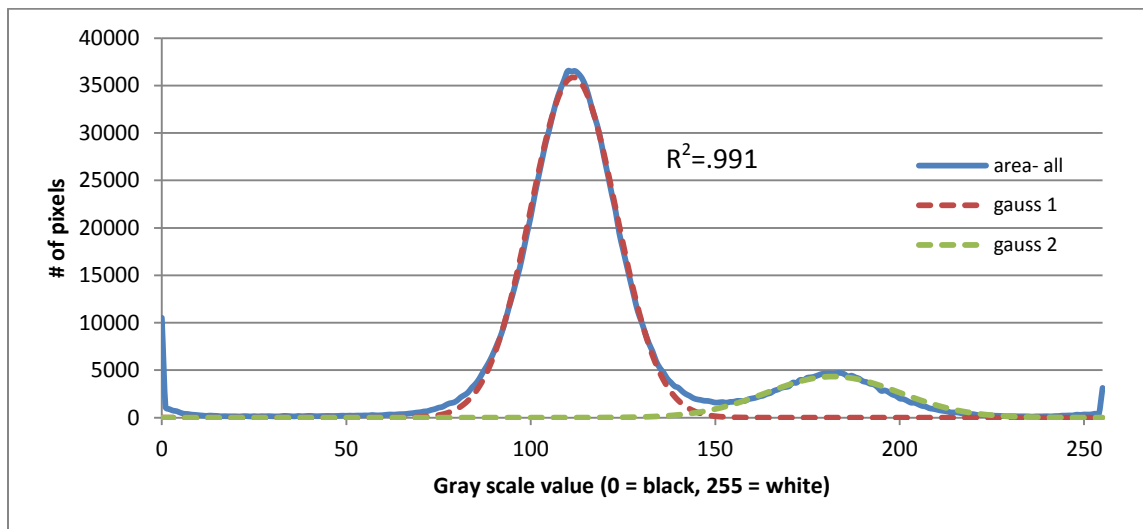


**Figure 17: Example Gaussian fits for generated histogram of grayscale values (same as Figure 16 above). The areas underneath the Gaussian fits are used to estimate the volume percentage of each phase, and deduce the porosity.**

Although the coefficient of determination ( $R^2$ ) value indicates an adequate fit (some as high as  $R^2 = 0.999$ ), it was also observed that the Gaussian function was systematically underestimating the total area beneath the curves. In particular, the fit is not adequately estimating the tails of the distribution. As such, a pseudo-Voight profile fit was employed. The equation below shows the approach utilized for each peak:

$$y_i = I_0[\eta L(x) + (1 - \eta)G(x)]$$

Where  $L(x)$  and  $G(x)$  represent a Lorentzian and Gaussian function, respectively, and  $\eta$  is the Lorentzian fraction of the fit. Table 10 below shows the functions used for  $L(x)$  and  $G(x)$ , and examples of each of these fits can be found in appendix B.

**Table 10: Lorentzian and Gaussian functions used within Pseudo Voight profile fit.**

$L(x)$	$y_i = y_0 + \left(\frac{2A}{\pi}\right) \left(\frac{w}{4(x - x_c)^2 + w^2}\right)$
$G(x)$	$y_i = y_0 + \left(\frac{A}{w\sqrt{\pi/2}}\right) \exp\left(-2\left(\frac{(x - x_c)}{w}\right)^2\right)$

As shown in Figure 18 below, a pseudo-Voight profile improves the fit for this particular curve by from an  $R^2$  value of 0.991 to 0.994. Though the numerical advantage is small, utilizing this fit eliminates a source of systematic error that can be avoided.

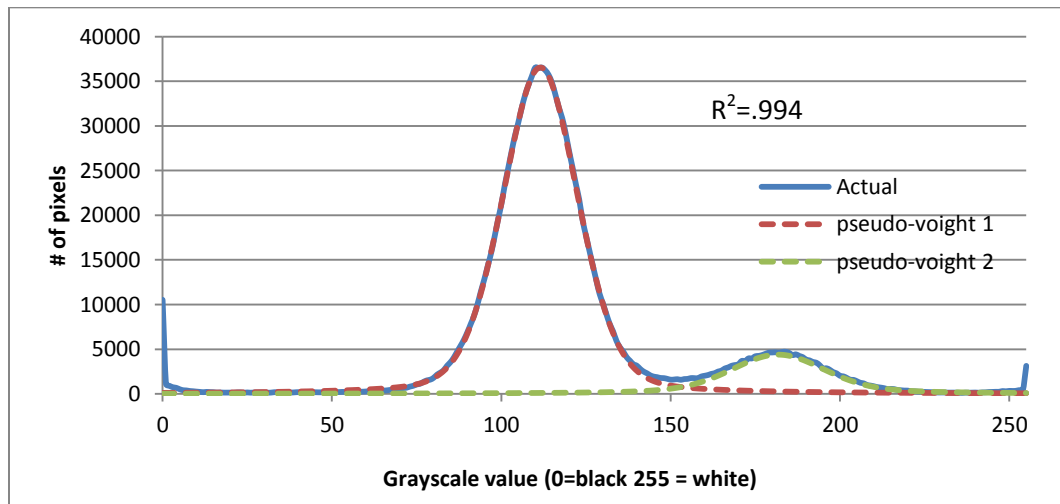


**Figure 18: Example of pseudo-Voight fits for generated histogram of grayscale values (Same as Figure 16 and Figure 17 above).**

Each pixel represents an equal amount of area within the micrograph, so the total number of pixels in a given mode represents its total area in the micrograph. By comparing this to the total number of pixels in the micrograph, the area percentage for each phase is estimated. Regardless of the direction in which the as-received sample was sectioned, the particles have circular cross sections in the micrographs. With this information, it is clear that the particles are spherical in nature. With this assumption, one can assume that the area percentage is directly proportional to the volume percentage of the particles [15]. These phase fraction values can be compared with those obtained using the x-ray diffraction methods outlined in Chapter 2.

In addition to the two modes, there is also a population of pixels that do not represent either phase and appear black (typically, grayscale value below 70). These pixels represent the area of the micrograph which is absent of binder or carbide (see Figure 19a). The area represented by these pixels is associated with the porosity observed in the sample. This assumption is susceptible to some error, since some pixels with grayscale value of 0 could represent polishing damage (leading to overestimation). The edges of the pores also often appear bright white which could lead to underestimation of the true porosity. Finally, some regions of pores are not pure black. Nevertheless, such a porosity estimate will be shown to agree well with the other methods employed.

Observations of the sample by eye revealed a characteristic difference in the appearance of the polished samples for different areas of the specimen. When observed under an optical microscope, this difference is related to a difference in the level of porosity for different sections of the plate. As such, a sampling of micrographs from across the entire specimen is utilized to assess the overall porosity and to provide a quantitative assessment of the porosity distribution. The area percent of porosity is determined with the method established above for the binder and

carbide phases. The porosity is also determined via an alternate method for clarification. This alternate method converts a given micrograph into a black and white image. The threshold is set between the lower bound of the carbide phase, and the upper bound of the porosity (grayscale value of 70). Once the image is parsed into black and white, the black pixels represent the area % of porosity, and the white pixels represent the other two phases together. An example of the raw SEM micrograph and its black and white conversion is shown below in Figure 19.

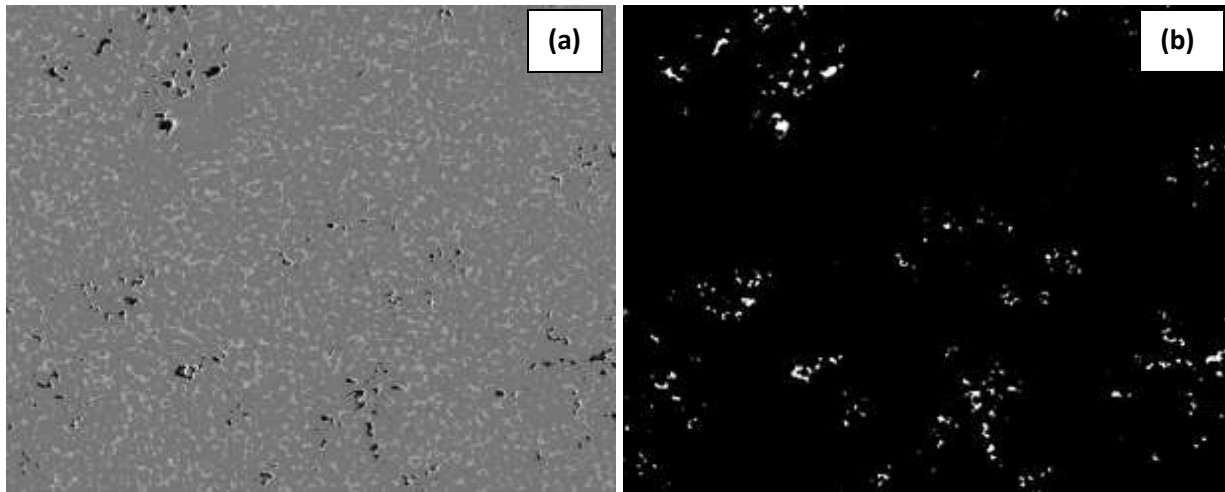


**Figure 19: (a) Example of SEM micrograph, and (b) its black and white conversion for estimation of porosity.**

### **3.3. Results**

#### **3.3.1. Microstructural characterization**

Figure 20 below shows a micrograph of the DDG-X cermet in both the as-received (left), and post-HIP (right) conditions. Recall that no etching procedure was required to obtain good contrast between the phases in the secondary electron imaging mode. The difference in average atomic number of the two phases is sufficient to provide the contrast needed [14]. In both conditions, the particles are observed to be circular in two dimensional sections from all

directions, and therefore, apparently spherical. This morphology is consistent with observations made in combustion-synthesized TiC-Ni compounds [9-10].

A core-rim structure is also observed, similar to what is reported in literature [7]. This core-rim structure is observed primarily in particles with an overall diameter less than or equal to  $7\mu\text{m}$ . In the as-received condition, the core-rim structure is observed to have more “rims” than in the post-HIP condition. This could be a result of diffusion during the high temperature HIP process. Since the HIPed specimens do not originate from the same as-received specimens as were studied in detail here, the HIP process cannot be considered a causal factor in the difference observed here. On the other hand, given that the HIP process occurs at  $1250^\circ\text{C}$ , it is conceivable that the titanium and/or molybdenum (Mo has solid solubility within the TiC phase) is equilibrating across the carbide, leading to a more uniform composition and contrast in the SEM image. The particles within the post-HIP condition also exhibit increased agglomeration, unlike the as-received condition. Along with this agglomeration, the ratio of carbide to binder visually appears different between the two samples observed in as-received and HIPed conditions, respectively. This observation is supported by the results in the next section.

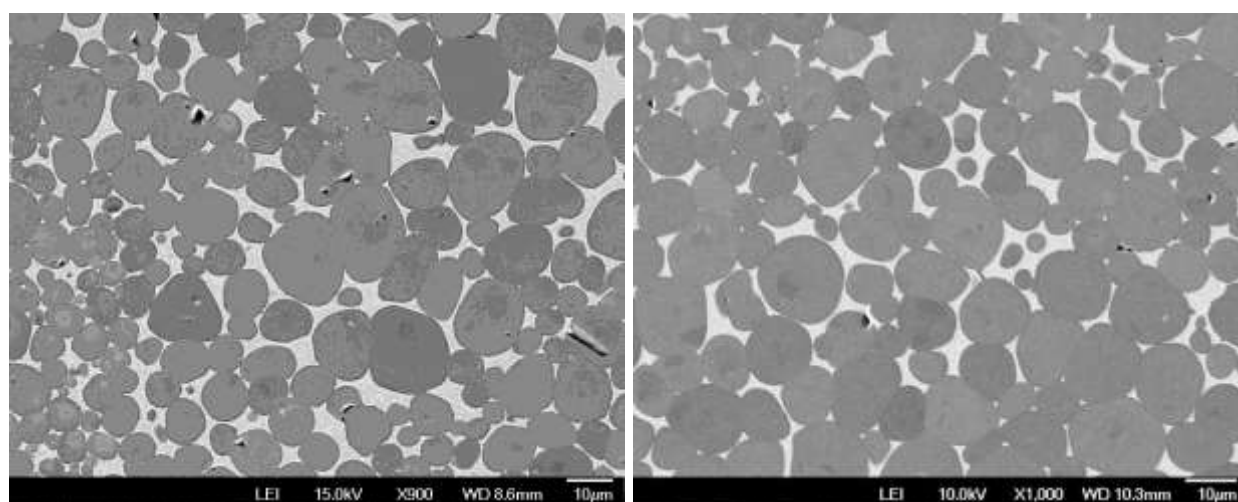


**Figure 20: (Left) SEM micrograph of as-received DDG-X cermet tile, and (right) SEM micrograph of DDG-X cermet after undergoing HIP treatment.**

Figure 21 below shows an example of the final polished specimen for a case in which 0.11 % (left), 0.94% (middle), and 1.8% porosity is observed (right). This variation in porosity was observed in multiple specimens, and seems to be directly related to the location of the micrograph as it related to the compaction axis from the initial processing of the cermet. The increased amounts of porosity are observed at one edge of the plate, and after a certain depth, the porosity drops to less than half of a percent (approximately). This dropoff distance is approximately 3mm into the depth of the plate, which is about half of the total depth of the 6mm plate that was measured.

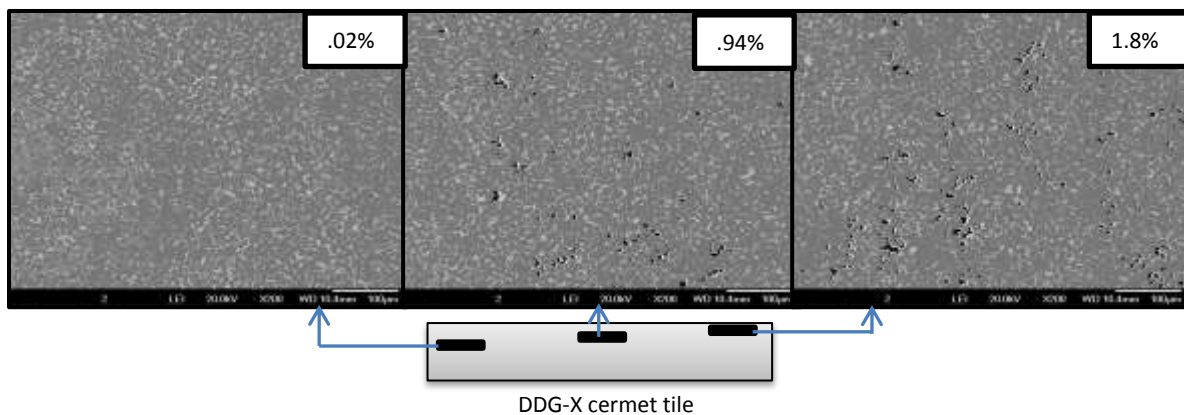


**Figure 21: Representation of variance of porosity with depth of the plate.**

Figure 22 below has a more complete profiling of another sample that shows how the porosity changes with depth. This analysis was also from a 6 mm plate and it profiles the entire plate. The fact that the porosity drops off to a minimum after a certain distance suggests that it may be the result of a single action press used during processing. With a single action press, a

pressure gradient develops between the active press and the inactive press. Since sintering processes are governed by the pressures within the compact, a pressure gradient could potentially lead to a gradient in density.

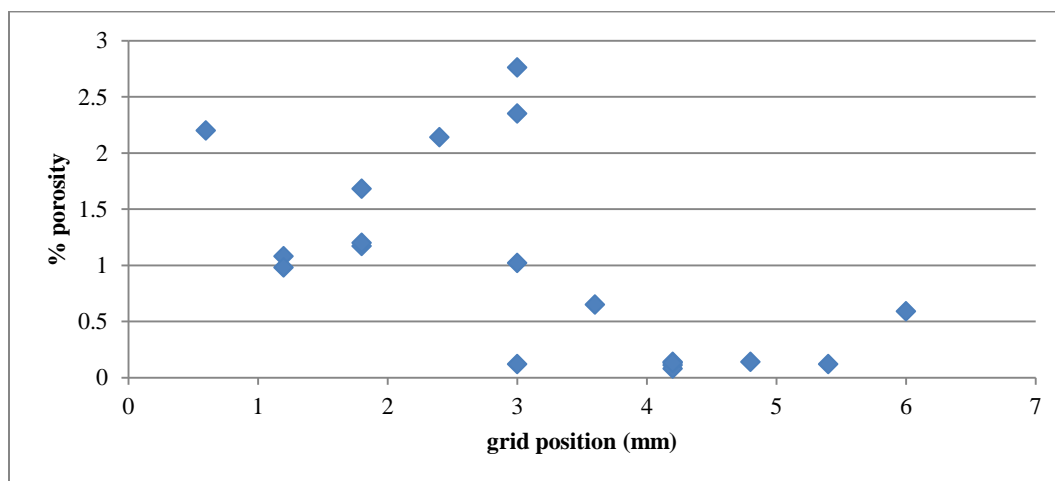


**Figure 22: Change in porosity observed with depth of plate...each increment is 600 $\mu$ m**

A particle size distribution was also determined for both the as-received and HIPed material. The sampling analyzed three micrographs for the same sample of each condition. As mentioned previously, the microstructure is consistent with compounds that have been produced via combustion synthesis. In those types of samples, the final particle sizes observed have been confirmed to correlate with the original metal powder particle size. For example, a cermet that was created from metal powders with a nominal size between 3-5 $\mu$ m will have smaller particles than one originating from metal powders with a nominal size between 8-10 $\mu$ m [16]. The as-received sample has an average particle size of  $9.12 \pm 3.68 \mu\text{m}$ , and the HIPed sample had an average particle size of  $10.13 \pm 3.82 \mu\text{m}$ . Even though the mean values are statistically distinct from one another, it cannot be definitively concluded that the difference in size is a result of the HIP process, since the HIPed sample was not produced from the analyzed as-received sample. As shown in Figure 23 below, the 2D apparent particle diameters appear to be normally

distributed. This observation is confirmed with quantile-quantile plots which are observed for each sample, which can be found in Appendix C.

The 3D particle size diameters can be determined by utilizing the factor of .7943, which relates the mean intercept diameter (2D diameter) to the 3D diameter [17]. This yields a mean 3D particle size of  $11.49 \pm 3.68\mu\text{m}$  for the as-received sample, and  $12.78 \pm 3.82\mu\text{m}$  for the HIPed sample.

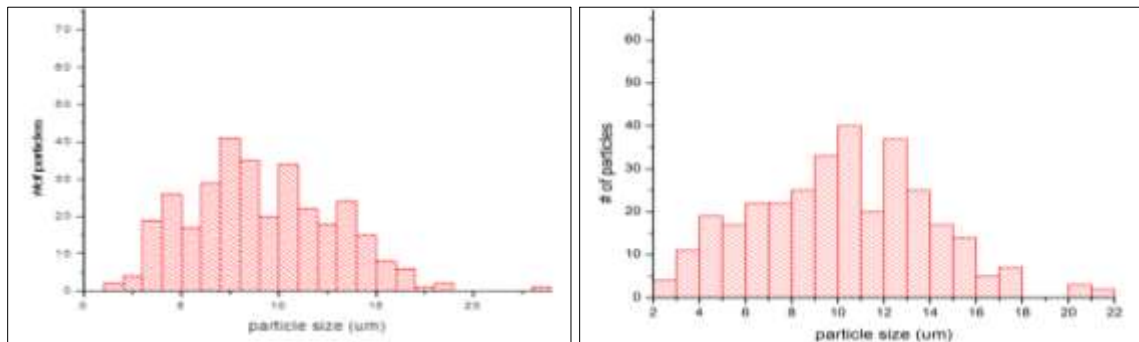


**Figure 23: Particle size distributions of as-received (left) and HIPed samples (right).**

### 3.3.2. Phase volume fraction and porosity

Table 11 below shows the average volume percentages of the carbide phase, binder phase, and porosity as determined via image analysis. Full tables with the observations from each sample, along with their goodness of fit values can be found in Appendix D. The porosity is also measured to have an average of 1.4% for the same as-received sample, and 1.12% for the same HIPed sample evaluated above. Table 11 shows the compiled phase fraction results from all methods employed. Thus, it is observed that although the volume percentage of porosity is virtually unchanged between samples which were examined in the as-received and HIPed conditions, the ratio of carbide to binder phase is affected. Since only one bulk sample of HIPed material was analyzed, the variation could be a result of sample-to-sample discrepancies.

**Table 11: Volume fractions for carbide, metal binder, and porosity as determined by image analysis.**

Specimen type	Vol % carbide	Vol % binder	Vol % porosity	R <sup>2</sup> value
As-received	0.8318	0.1516	0.0166	0.996
Post - HIP	0.8694	0.1117	0.0188	0.995

The porosity is also measured to have an average of 1.4% for the same as-received sample, and 1.12% for the same HIPed sample evaluated above. Table 12 shows the compiled phase fraction results from all methods employed.

**Table 12: Summary of phase fraction results from chapter 2 and chapter 3**

	vol % TiC	vol % Ni	vol % porosity
<b>External Standard</b>	81	19	0
<b>Direct Comparison</b>	82	18	0
<b>Rietveld</b>	84	16	0
<b>Image analysis</b>	83	15	1.6

### 3.4. Discussion

The results from this section give a significant amount of evidence that the as-received specimens are created via reaction synthesis, coupled with some pressing action to achieve the high density observed. First, the spatial discrepancies identified with porosity indicate that there is some directionality associated with the samples during synthesis. (I.e. there is more porosity on one side of the plate than the other, suggesting that a single action press may have been employed.) If produced by combustion synthesis plus a pressing action, the bulk samples would have been first compressed into a green compact, then ignited, and continuously pressed during the reaction (see Figure 2 in section 1.2). A single-action press produces a gradient in the porosity because friction between the particles results in a pressure gradient, and it is the pressure which drives densification over the sintering forces alone [18]. Second, the microstructure

consists of spherical TiC particles embedded in a Ni matrix. In literature, this topology for TiC/Ni-Mo cermets is observed to be a result of combustion synthesis [9-11]. Liquid phase sintered compacts of this same material system have been observed to produce intermetallic phases [19].

The image analysis method employed is also established as a consistent and precise way to measure phase volume fractions of this cermet. All known systematic errors have been addressed, and the uncertainty for each result is not larger than the amount of porosity detected. The X-ray diffraction methods are incapable of assessing porosity, or attributing it to a specific phase. Thus, the image-based techniques permit estimation of important structural features (particle size, porosity, level of agglomeration, etc.), which are not possible via any of the three methods employed in Chapter 2. The results suggest that the amount of Ni binder in the cermet could be overestimated by the X-ray diffraction methods. . The carbide to binder ratio estimated from the image analysis (without porosity) is .85 to .15, respectively.

### **3.5. Conclusions**

From these results, we can make a number of affirmations for the method of analysis used, as well as some of the results obtained from the previous chapter on x-ray diffraction.

- First, the cermet consists of spheroidal TiC particles embedded in the Ni matrix. The topology is such that nearly every TiC particle is fully surrounded by the Ni matrix. There are, however, some regions where TiC particles appear to touch one another or be separated by areas of localized porosity. This is consistent with the combustion synthesis-based powder metallurgy process suspected and relevant to fracture modes observed.

- The average particle size of an as-received plate was determined to be 11.49 $\mu\text{m}$  and the particle size distribution is also observed to be normal.
- These results confirm that the difference in average atomic number of the TiC and Ni phases was large enough such that the contrast between them in the SEM micrographs was enough to delineate the pixels that belong to each phase.
- The pseudo-Voigt fits used to approximate for the pixel distributions for each phase was effective and consistent in determining the volume fraction for each phase, yielding a coefficient of determination values of  $R^2 > 0.996$ . This helps to establish the method as self-consistent.
- Porosity within the sample is observed as an absence of binder between TiC particles. The level of porosity observed by thresholding the images (1.4%) or via the fitting routine discussed above (1.6 %) is consistent with that determined from theoretical density calculations provided in the next chapter.
- The porosity is also observed to be spatially dependent through the thickness of the as-received tiles (i.e. there is more porosity on one side of the plate relative to the other). This suggests that the as-received cermet underwent a single action pressing operation during synthesis. A single action press would produce a gradient in pressure within the green compact, resulting in a subsequent gradient in density of the final synthesized tiles would result.
- The volume fractions measured in the as received sample via image analysis are: TiC: 0.83, Ni: 0.15, porosity: 0.016. The values obtained via Rietveld whole pattern fitting and direct comparison method are the closest to this analysis, with measured volume fractions of TiC: 0.82, Ni: 0.18 and TiC: 0.84, Ni: 0.16, respectively.

## 4. Compositional Analysis of DDG-X Cermet tiles

### 4.1. Introduction

The previous chapters reveal the presence of a titanium carbide and nickel solid solution phase within the DDG-X, with relative volume fractions of 0.83 and 0.15, respectively. However, it is noted that the X-ray diffraction peaks are systematically shifted a la Vegard's law [12], suggesting that there are additional elements present in solid solution. In order to gain more understanding of the chemical composition of the cermet, further analysis of the composition by phase is needed. Inductively coupled plasma optical emission spectroscopy (ICP-OES) and energy dispersive x-ray spectroscopy (EDS) were conducted on the bulk material in order to determine both the overall, and phase by phase composition of the material, respectively. Greater confidence is given to the ICP-OES method than the EDS, because without proper standards for the material in hand, EDS is essentially a qualitative measure of the chemical composition [20]. For example, it will be shown that the EDS results suggest that molybdenum fluoresces in the presence of nickel characteristic x-rays. This would mean that this material would have a tendency to overestimate the amount of molybdenum, while underestimating the amount of nickel present. With that cautionary note, this chapter will show that the phase by phase composition obtained by EDS is in fact consistent with the overall composition determined by ICP-OES.

It must also be noted that neither EDS nor ICP are capable of effectively analyzing the presence of light elements ( $Z < 10$ ). Some microscopes allow for analysis of elements as light as carbon, but even with a ZAF correction ( $Z$  - atomic number,  $A$  - absorption, and  $F$  - fluorescence),

the uncertainty in these values is often unknown [20]. As such, the EDS results obtained in this chapter will be analyzed from a “metals only” approach. This means that the results will be used to obtain the relative weight and atomic percentages of the metals.

## **4.2. Experimental procedure**

### **4.2.1. Inductively coupled plasma optical emission spectroscopy**

Inductively coupled plasma provides a quantitative measure of the elements present in inorganic materials through the detection of the “spontaneous emission of photons from atoms and ions that have been excited in a RF discharge [21]. The sample is introduced in liquid form, and subsequently nebulized and directed into the plasma. Since the inductively coupled plasma remains at temperature in excess of 10,000 K, the sample is vaporized, and the resulting atoms are excited. Finally, the atom returns to its ground state, emitting a photon of characteristic wavelength in the process. Individual elements weight percentages are quantified by observing the energy for a given wavelength. The quantities are calibrated against a standard solution of the constituent elements made from elemental standards of known weight percentages, as well as an internal standard.

In order to analyze the Ti(Mo)C-Ni cermet tile via inductively coupled plasma optical emission spectroscopy, 200 mg of the bulk tile digested in solution of 5 ml Nitric acid (99.99% HNO<sub>3</sub>), and 5 ml sulfuric acid (99.99% H<sub>2</sub>SO<sub>4</sub>). The solution is then placed in a warm (50°C) bath with periodic sonication until the bulk sample is completely dissolved. Samples were obtained from two different plates, with the overall digestion of the cermet lasting for approximately two weeks.

Next, the standards must be prepared. Five standards were utilized to ensure a well calibrated, quantitative measure of the elements present. The first three standards each contain titanium, carbon, nickel, and molybdenum at the same ratio, but have different concentrations through dilution. Table 13 below shows the different concentrations in each of the three standards. There is also an internal standard of yttrium (Y) that is used to flush the system prior to and between each sample, and an external standard of zinc (Zn) that is used to calibrate the emission.

**Table 13: Standard solutions prepared for ICP - OES analysis**

	High (ppm)	Mid(ppm)	Low (ppm)
Titanium (in HNO <sub>3</sub> )	600	60	6
Carbon (in HNO <sub>3</sub> )	100	10	1
Nickel (in HNO <sub>3</sub> )	150	15	1.5
Molybdenum (in NH <sub>4</sub> OH)	150	15	1.5

Since the standards are received at an overall concentration of 1000 ppm (each already in solution), they are diluted with water to achieve the concentrations noted above. Each standard has a constant volume of 15 mL.

Once all standards are prepared, a zinc sample at 2 ppm concentration is used to calibrate the system. The internal standard of yttrium that runs constantly throughout the analysis, and additional Y is used to flush the system between samples. Results from the ICP-OES are given in weight percentages.

#### **4.2.2. Energy dispersive spectroscopy**

Energy dispersive spectroscopy (EDS) is a chemical analysis technique that is most commonly used within a scanning electron microscope (SEM). First, a focused beam of electrons

is used to excite the electrons within the lower orbitals of all atoms present in the sample, leaving electron holes behind. For each atom present, another electron drops from a higher shell to electron hole, and an x-ray of characteristic wavelength is released. By measuring the energy and amount of x-rays detected over a given collection time, it is possible to resolve the elements present, and their relative weights. Figure 24 below gives a graphical account of this process.

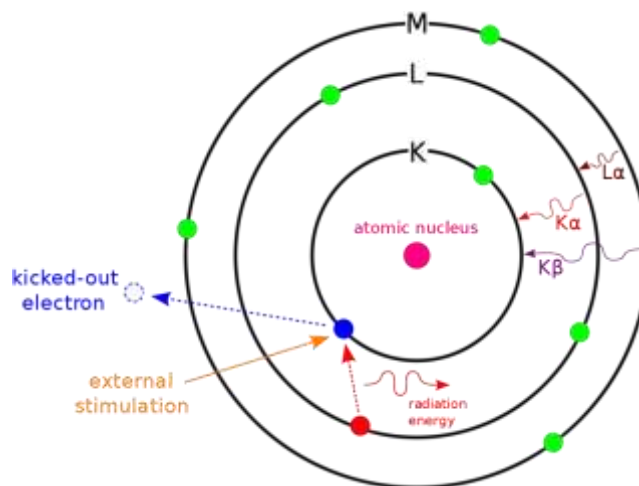


**Figure 24: Graphical representation of theoretical basis of energy dispersive spectroscopy (EDS)<sup>1</sup> [22]**

In some cases however, the emitted x-ray can be absorbed by another element in the sample with a lower  $Z$  value. As a result, an electron within the lower  $Z$  element is excited, and an x-ray with its characteristic wavelength is subsequently emitted. This process is known as fluorescence [23], and it causes a suppression of the amount of x-rays detected for the higher  $Z$  element, and inflation in the x-rays detected for the lower  $Z$  element. The ratio at which this occurs, known as the  $k$  ratio, is specific to the interaction between two elements. Standards with known weight percentages of sets of elements are used to determine and correct for these ratios in order to yield a truly quantitative result. In the absence of standards, a so-called ZAF

<sup>1</sup> This image is licensed under the Creative Commons Attribution-Share Alike 3.0 Unported license. It is open for all to copy, reuse, and distribute with attribution to author.

correction is commonly employed, which allows an adjustment for atomic number (Z), absorption (A), and fluorescence (F). [23]

### 4.3. Results

#### 4.3.1. Overall chemistry

Two sample types were examined: one from a DDG-X plate which was 6 mm thick and one from a plate which was 10 mm thick. Two samples of each type were measured and the average results reported below. A complete listing of the data and uncertainties can be found in appendix E, which reveals that none of the samples varied in composition from the others outside of the experimental uncertainty. This suggests that the David Defense Group has good compositional control over the synthesis process.

For the ICP analysis, the presence of carbon, molybdenum, nickel, and titanium was assessed against a reference peak for the respective element. In some cases, multiple reference peaks were chosen to avoid interference effects that may diminish the presence of one peak.

Table 14 below shows a compilation of the results, including the atomic and weight percent collected for each. Atomic and weight percentages are average values for elements that are evaluated against multiple peaks.

**Table 14: Average chemical composition of the DDG-X plates determined by ICP -OES**

	Reference wavelengths (nm)	atomic weight	wt. %	at %
Ti	192.8, 323.9, 351	47.9	59.4	46.6
C	193.0	12	10.8	33.6
Ni	221.6, 231.6	58.7	22.6	14.5
Mo	202,204.5	95.9	7.28	2.85
<b>Total</b>			<b>100</b>	<b>97.44</b>

### 4.3.2. Phase-by-phase chemistry

Without a proper standard for the DDG-X cermet, energy dispersive spectroscopy is regarded as a semi-quantitative technique. As such, this method is used to gain a relative understanding of how the composition varies spatially within the microstructure. First, an EDS spectrum of a 600  $\mu\text{m}$  x 600  $\mu\text{m}$  sampling of the DDG-X cermet tile to obtain the overall weight percentages. Next, point probe analysis is utilized to obtain an EDS spectrum that is specific to the carbide, and then the binder. Finally, a line scan is performed in order to determine if there are any spatial differences in the individual phases. Table 15 following scan parameters were utilized during the area, point, and line scans.

**Table 15: EDS scan parameters**

<b>Live Time</b>	<b>150s</b>
<b>Dead Time</b>	<b>11.51%</b>
<b>Beam Current</b>	<b>.03 nA</b>
<b>Beam Voltage</b>	<b>15 keV</b>
<b>Takeoff Angle</b>	<b>29</b>

Energy dispersive spectroscopy confirmed the presence of molybdenum in the DDG-X cermet tiles. Nickel, Molybdenum, Titanium, and Carbon are the only elements detected within the system. EDS does not detect elements at concentrations less than 0.1 wt% [24], so it is possible that some trace elements may exist. This method is also not as accurate when detecting elements with  $Z < 10$ , so carbon ( $Z=6$ ) values are viewed with some suspicion. Figure 25 below shows the area from which the broad spectrum is collected. A relatively low magnification was selected in order to sample as much area as possible.

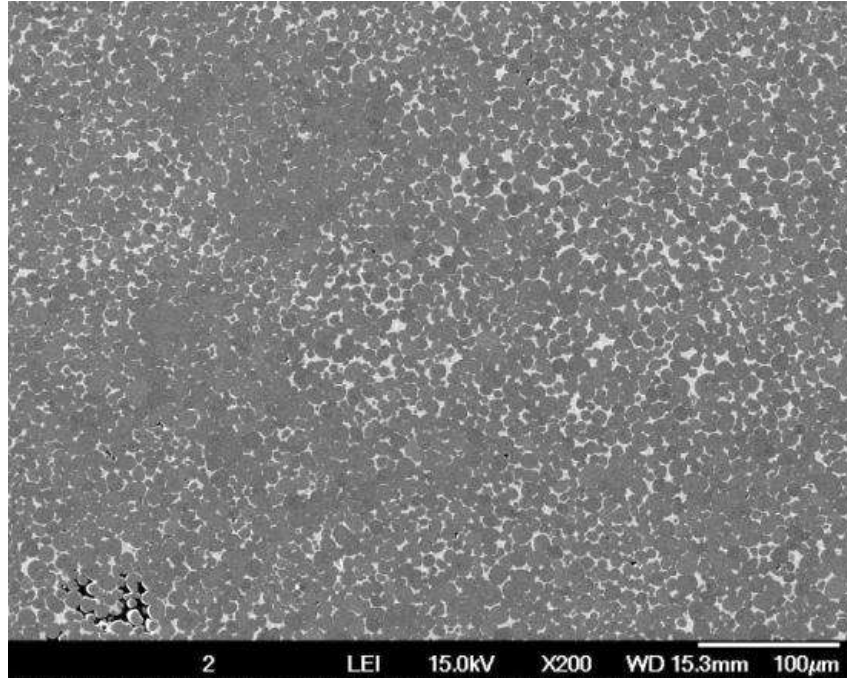


**Figure 25: SEM Micrograph of total area examined for EDS broad spectrum. Total area is roughly  $1200\mu\text{m}^2$**

Figure 26 below shows the overall composition of the cermet within the parameters of this technique. The horizontal scale is keV, and the vertical axis is simply counts detected. Table 16 below shows the overall composition as determined by EDS. It is notably different from the results from ICP-OES as reported in section 4.3.1 above. In particular, the Ni and Mo content estimated are distinctly different, despite the ZAF corrections made within the software. However, the phase-by-phase compositional analysis does not seem to be affected as much as the broad spectrum, as subsequent analyses in this chapter will show.

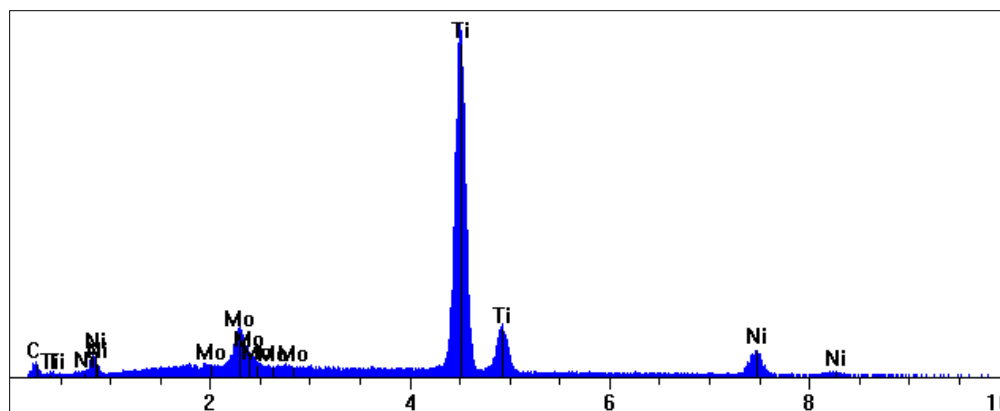


Figure 26: EDS compositional analysis of entire microstructure

Table 16: EDS compositional analysis of entire microstructure

Element	ZAF Correction	Line	Wt.%	Wt.% Metals	At%	Chi Squared
<b>Ti</b>	1.045	KA1	63.2	69.1	54.4	11.4
<b>C</b>	2.891	KA1	8.46	n/a	29.1	1.12
<b>Ni</b>	1.060	KA1	15.7	17.2	11.1	0.79
<b>Mo</b>	1.179	LA1	12.6	13.8	5.43	1.83
<b>Total</b>			<b>100.00</b>	<b>100.00</b>	<b>100.00</b>	<b>6.48</b>

Figure 27 below indicates the probe locations used to collect EDS data from the binder and the carbide phases separately. Figure 28 and Figure 29 below show the EDS spectra generated for the binder phase and the carbide phase, respectively.

Table 17 and Table 18 below show the respective weight and atomic percentages detected, with ZAF corrections applied. Within the binder, it is observed that it is mostly nickel, but also contains titanium and a small amount of molybdenum. Given the interaction volume of the probe within the binder, it is also possible that some of the carbide phase could be detected beneath the binder phase. If so, this would exaggerate the C and Ti content within the binder. For the results reported below, multiple spectra were collected from the binder regions, and the one with the lowest observed Ti and C were employed to determine the binder chemistry without contributions from the TiC.

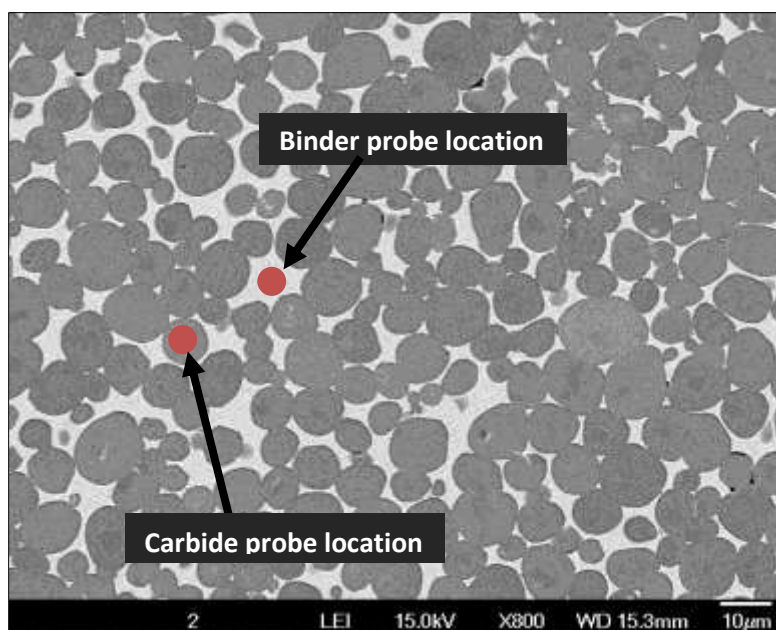


Figure 27: Binder and carbide probe locations

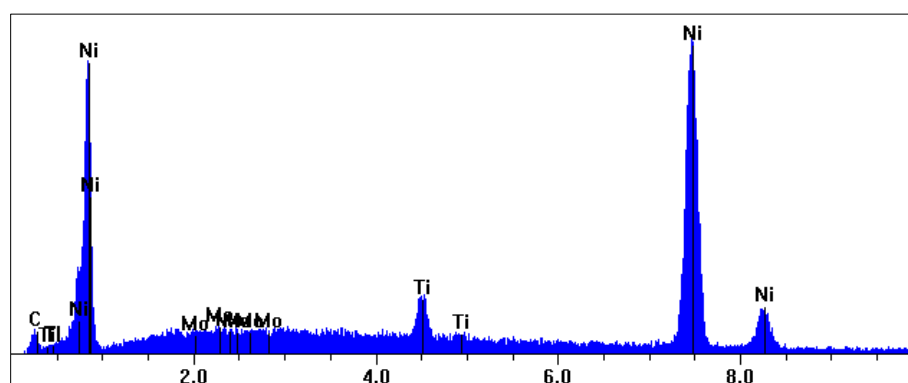


Figure 28: EDS compositional analysis of binder

Table 17: EDS compositional analysis of binder

Element	Line	ZAF Correction	Wt.%	Wt.% Metals	At%	Chi Squared
Ti	KA1	1.018	4.83	5.43	4.12	2.55
C	KA1	7.713	11.0	n/a	37.4	1.32
Ni	KA1	1.044	83.7	94.1	58.3	8.63
Mo	LA1	1.532	0.45	0.51	0.19	1.17
<b>Total</b>			<b>100.00</b>	<b>100.00</b>	<b>100.00</b>	<b>6.22</b>

Within the carbide phase, it is observed that molybdenum is definitively present. However, no nickel is observed in the carbide phase. This provides good evidence that the interaction volume of the electron probe is not spilling out of the carbide and into the surrounding binder, since that is primarily Ni. Since the carbide is primarily Ti and C, two relatively low Z elements, the interaction volume is likely to be larger in the carbide than in the nickel rich binder. This is encouraging, since it gives more confidence in the binder composition as well. However, the binder has narrower dimensions, so there is still reason to be concerned about the composition.

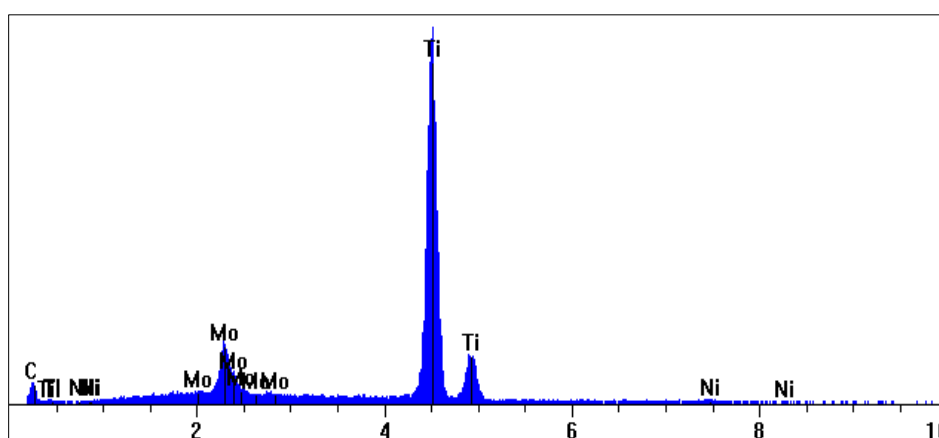


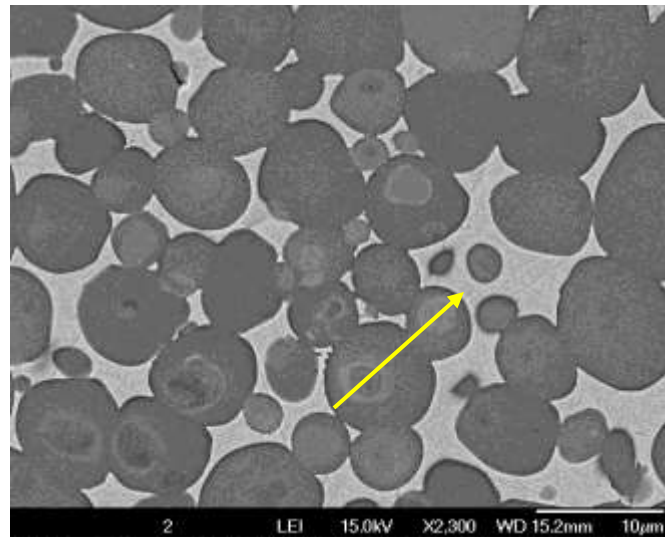
Figure 29: EDS compositional analysis of carbide

Table 18: EDS compositional analysis of carbide

Element	Line	ZAF Correction	Wt.%	Wt.% Metals	At%	Chi Squared
Ti	KA1	1.073	61.16	88.2	32.62	57.85
C	KA1	3.018	30.64	n/a	65.17	4.11
Ni	KA1	1.126	0.19	0.27	0.08	1.12
Mo	LA1	1.125	8.02	11.6	2.14	2.14
<b>Total</b>			<b>100.00</b>	<b>100.00</b>	<b>100.00</b>	<b>36.48</b>

Owing to the fact that one of the contrast mechanisms of a scanning electron microscope (SEM) micrograph is directly related to a material's constituent element's atomic numbers (or Z values), it is observed that the nickel-rich binder appears bright, relative to the lower average Z

carbide. At a more detailed level, it is observed that the composition of each of the carbide particles seems to vary, since there are contrast variations within individual carbide particles. Some carbide particles are darker than others, implying that they have lower molybdenum content. As shown in Figure 30 below, a core-rim structure, as previously observed by LaSalvia [7], is observed to be present. In some cases, more than one rim is observed. In the figure below, the carbide serves as both the core, and the outermost rim. Instances of a carbide core with a molybdenum rim are also observed. Figure 31 below shows the corresponding line scan for the micrograph in Figure 30. The two little peaks on the left hand side of the in the Mo compositional trace (Figure 31) correspond with the light colored ring in the first particle. The broader peak on the right hand side of the Mo trace correspond to the lighter colored “bulls eye” in the middle of the second particle interrogated.



**Figure 30 : SEM Micrograph illustrating core-rim structure within carbide**

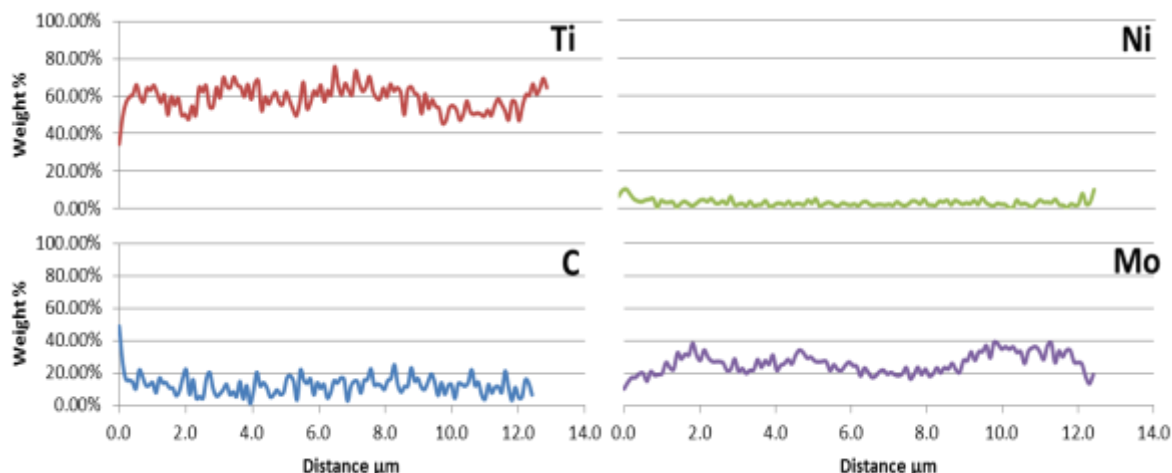


**Figure 31: Linescan across core-rim structure illustrating the change in molybdenum content.**

This core-rim structure is evidence that the DDG-X cermet tiles have been processed via combustion synthesis with elemental powders, as opposed to liquid phase sintering of homogenous TiC particles within a Ni-rich binder, which produces a cubic TiC core-rim structure [25]. In order to explore this core-rim structure further, a line scan is performed to gain perspective on how the composition varies within a phase, and to determine the relative compositions between phases. The results, as shown in Figure 32 and Figure 33 and below, give additional confirmation that the molybdenum exists almost entirely in the carbide phase. This makes sense, given that titanium carbide has a high solid solubility for molybdenum whereas nickel has almost no molybdenum solubility, as evidenced by the phase diagrams which can be found in appendix F. At all points throughout the scan, molybdenum is detected at a higher weight percentage than both the EDS broad spectrum and point scans. This provides some additional evidence that when within the binder phase; the point probe interaction volume may be picking up some carbide particles just beneath the surface. Again, this was avoided in the point probe measurements by selecting spectra with the lowest content of Ti and C.

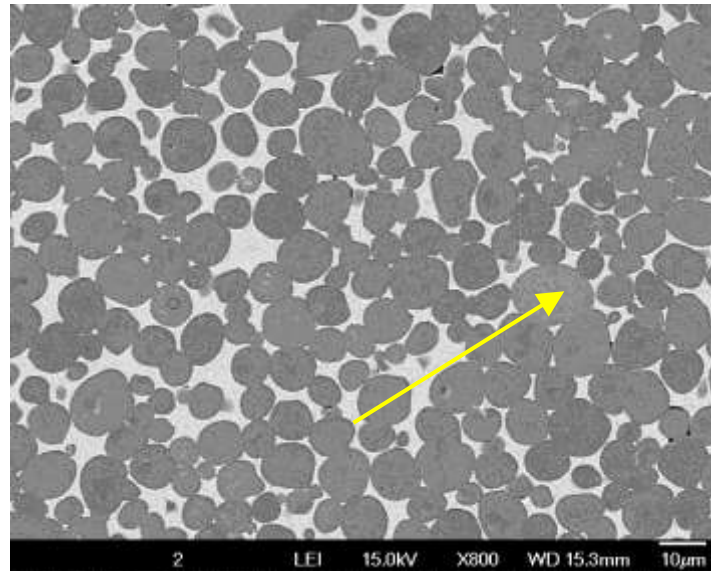


**Figure 32: SEM micrograph showing probe path for line scan analysis.**

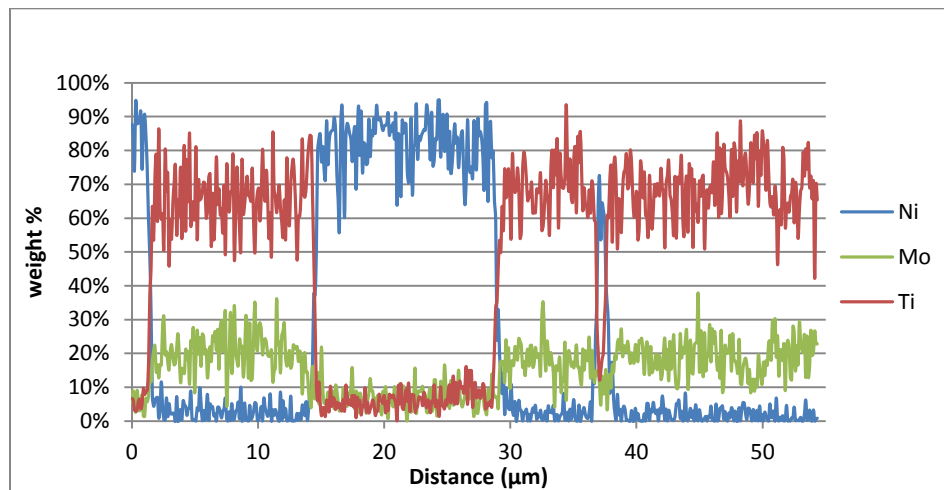


**Figure 33: Line scan results showing change in metal composition over a span of 55µm. The titanium weight percentage can be used to track when the probe was within the carbide or binder phase.**

These results also pose a few questions that may be useful to answer. First, what drives the molybdenum into solution with the titanium carbide as opposed to the nickel binder? One can assume that there is a thermodynamically based reason that this occurs, but for the purpose of creating the core-rim structure intentionally, it would be very helpful to know. Authors suggest that the core-rim structure is a result of non-equilibrium conditions produced when there are Mo-

rich areas within either the carbide or binder melt during formation [26]. Other authors who have studied these kinds of materials have mentioned the presence of molybdenum as a wetting agent, and it has also been found to have some implications to macro scale properties such as fracture toughness [7].

#### **4.4. Discussion**

Both methods of chemical analysis have their own respective strengths and limitations. First, the method of EDS analysis can sometimes suffer from interactions between the constituent elements, such as secondary fluorescence. The detector is only capable of distinguishing the energy (or wavelength) associated with an emitted x-ray, so a standard is the only way to quantify how much the output values need to adjust. ICP, on the other hand, is only capable of giving the overall composition of a material since all samples must be in solution prior to analysis. With these known limitations, the two methods are combined to provide a robust solution for the DDG-X cermet.

At first glance, it looks as if the nickel is fluorescing the molybdenum, since the Ni is low and Mo is high in the overall EDS data, relative to the composition determined by ICP-OES. Interestingly, however, phase-by-phase analysis reveals that the Mo content in the binder is almost nil, and the Mo content in the nickel-poor carbide is rated to be only 8 wt %. Thus, it is hard to see how the overall Mo composition could possibly be 13 wt %, as shown in Table 16 above. The following calculations are made based on the phase volume fractions obtained by x-ray (Chapter 2) or image (Chapter 3) analysis with the initial (to be tested) assumption that the individual phase compositions via EDS are correct.

Given the known crystal structures of the two phases determined by x-ray diffraction (Chapter 2), and assuming the chemistries obtained by EDS are approximately correct, one can determine the theoretical densities of the individual phases. With the added information of the individual phase volume percentage (including porosity), one can determine the theoretical density of the plate overall. The formula below gives the theoretical basis upon which the phase densities were calculated:

$$\rho = \frac{n'(\sum A_C + \sum A_A)}{V_C N_A}$$

Where  $n'$  is the number of formula units per cell,  $A_C$  is the average atomic mass on the cation lattice sites,  $A_A$  is the average atomic mass on the anion lattice sites,  $V_C$  is the unit cell volume, and  $N_A$  is the constant Avogadro's number. Table 19 below shows the method used to calculate the inputs used in the density formula above, and Table 20 below shows the values utilized. The atomic fractions are generated using the phase by phase atomic percentages from the EDS analysis presented earlier in this chapter.

**Table 19: Methods for calculating parameters used in theoretical density evaluation**

	$n'$	$A_C^*$	$A_A$	$V_C$
<b>Nickel</b>	4 (cF4)	$f_{Ni}A_{Ni} + f_{Ti}A_{Ti} + f_{Mo}A_{Mo}$	n/a	$(3.52 \text{ \AA})^3$
<b>Titanium Carbide</b>	4 (cF8)	$f_{Ni}A_{Ni} + f_{Ti}A_{Ti} + f_{Mo}A_{Mo}$	$A_{Carbon}$	$(4.93 \text{ \AA})^3$

*\*f represents the atomic fraction of the respective element in the given phase as calculated by EDS. This number is calculated using the relative fractions of the metals only.*

**Table 20: Atomic fractions and atomic mass values used in theoretical density calculation**

	$f_{Ni}$	$A_{Ni}$	$f_{Ti}$	$A_{Ti}$	$f_{Mo}$	$A_{Mo}$	$f_C$	$A_C$	$\rho$ (g/cc)
<b>Nickel</b>	.9312	58.68	.0658	47.87	.003	95.94	0	12.01	5.17
<b>Titanium Carbide</b>	.0023	58.68	.9362	47.87	.0614	95.94	1	12.01	8.63

Once we have the weight fractions of the individual phases, we can determine the overall composition of the composite. This number can be determined by converting the calculated volume fractions per phase (from image analysis TiC: 0.83, Ni: 0.15, porosity: 0.016) to a weight percentage [27]. For example, the Mo content in the cermet as a whole: 11.6 wt.% (metals basis) in the carbide  $\times 74 \text{ wt\% carbide}^2 + 0.5 \text{ wt\% in the binder} \times 26 \text{ wt\% binder}$  yields 8.7 wt %, which is within 1% of the ICP result (8 wt% metals basis). However, when you scan over the whole sample in the SEM you get a value of 13% (which is bigger than both of the individual phases and makes no sense). This suggests that one cannot do reliable standardless corrections of the EDS data from multiphase broad area scans, but the data from individual phases does seem fairly reliable. Similarly, with the numbers for Ni: 94wt% in the 26wt% binder + 0.3 wt.% in the 74wt% carbide we obtain an overall Ni content of 25 wt% which is essentially equal to the ICP result of 25 wt.%. The analysis of Ti is similarly encouraging: 88wt% (metals basis) in the 74 wt% carbide + 5.4 wt% in the 26wt% binder yields an overall Ti content of 66.7 wt%, again very similar to the overall ICP result of 66.5 wt%.

With regard to the interstitial alloying element, C, it is observed in the EDS spectrum of the binder phase. However, carbon is such a light atom ( $Z=6$ ), that it is not possible to accurately quantify the amount with this method. The high level of C suggested may result from spilling of the electron interaction volume from the binder into the carbide phase. If one makes an estimate of the C content based upon an assumption of 100% site occupancy in the Ti(Mo)C and nil C in the binder, based upon the very small solubility for C in Ni at low temperatures (see Appendix F), one obtains 19.1wt% in the carbide which means (given the 74wt% phase fraction of TiC in the cermet) there should be about 14wt% overall. This is significantly higher than the ICP-OES

---

<sup>2</sup> In order to determine the wt% from the known vol%, we employ the theoretical density for each phase (calculated below)  $vol\% = 1/[1 + \rho_f/\rho_m (1/(wt\%) - 1)]$ , where  $\rho_f$  is density of the TiC phase and  $\rho_m$  is density of the matrix.

estimate of 11wt%. Given the relatively high eutectic solubility for C in Ni, it is possible that the overall C content is even higher. The actual C content remains unknown at this point. One interesting follow-up question would be to determine the C site occupancy in the TiC phase. Previous researchers have struggled to obtain complete site occupancy in monolithic TiC [31-32]. It would be interesting to know how combustion synthesized carbide in the present cermet compares.

With regard to substitution alloying additions, there is 6.14 wt.% Mo in the TiC and there is 6.58 wt.% Ti in the Ni-binder. As mentioned previously, this makes sense as TiC has a moderate solid solubility for Mo whereas it is nearly insoluble in Ni. Similarly, Ti is quite soluble in Ni. This partitioning of Mo in the TiC phase is also observed by a study performed by LaSalvia and Meyers [7] in which they investigate the effect of Mo content on the properties of the cermet. They also note the appearance of a Mo-rich shell, core, or both as described as a “core-rim” structure as observed here. There also is effectively no nickel in the carbide phase, and no molybdenum in the nickel phase. This is also consistent with the phase behavior for these systems, as TiC has little solubility for Ni and Ni has no solid solubility for Mo. In addition, there was no observation of any Ni-Ti intermetallics which frequently form at the interface between the binder and the carbide during liquid phase sintering [28]. This is additional evidence that the material was produced by combustion synthesis. All relevant phase diagrams may be found in appendix F.

From this point, a simple rule of mixtures calculation can be used to obtain the compound’s theoretical density as shown below:

$$\rho_{total} = v_{Ni}\rho_{Ni} + v_{TiC}\rho_{TiC}$$

The volume fraction values from Rietveld analysis (84% TiC, 16% Ni) can be used to estimate the theoretical density at 5.72 g/cc. When compared with the geometrically measured density of 5.52 g/cc, this yields an estimated porosity of 3.7%, which is a bit higher than the value of 1.6% obtained from the image analysis. However, it should be noted that depending on the assumptions made, the calculated density can fluctuate. For example, if one assumes that the highest estimate of carbide volume fraction obtained in this study (85% TiC, 15% Ni via image analysis) one obtains a theoretical density of 5.69 g/cc, yielding a porosity of 3.0%. If one assumes the lowest estimate of carbide (81% TiC, 19% Ni via direct comparison XRD), one obtains a theoretical density of 5.83 g/cc, yielding a porosity level of 5.3%. Further, assuming only 88% site occupancy of carbon in the TiC lattice and the volume fractions from Rietveld analysis, the theoretical density is calculated as 5.62 g/cc, which yields an estimated porosity of 1.8%. The calculated density could fall anywhere within the range of 5.59 g/cc (highest carbide fraction and 88% C site occupancy), and 5.83 g/cc (lowest carbide fraction and 100% C site occupancy). In summary, the porosity level obtained by image analysis is within the range of values one would compute based on reasonable estimates of the theoretical density. If anything, these estimates would suggest a slightly higher level of porosity may be present than the image analysis indicates.

#### **4.5. Conclusions**

These results combined with those from Chapter 3 allow us to make a number of conclusions regarding the elements of the cermet microstructure which will affect the mechanical properties. They are listed below:

- The inductively coupled plasma-optical spectroscopy shows the overall chemistry in weight percent of the cermet as 59% TiC, 11% C, 23% Ni, and 7% Mo. Other elements

were not present in quantities above the detection limit of the technique. Notably, the C content appears to be underestimated based upon the known carbide volume fraction and reasonable assumptions regarding C site occupancy.

- Energy dispersive spectroscopy (EDS) of the overall chemistry of the cermet was found to be inaccurate. This is likely a result of complex interactions that happen between the phases and/or secondary fluorescence.
- Although EDS is not effective in determining the overall chemistry, it provides a phase by phase metals-basis chemistry (in the nickel-rich binder: 94%Ni, 5.4%Ti, <1% Mo, and in titanium carbide: <1%Ni, 88% Ti, 11%Mo, all wt%). Given the known phase fractions from XRD and image analysis, it was shown that the overall chemistry determined by EDS was equivalent with to within 1% of the overall chemistry as determined by ICP-OES. Since carbon is too light ( $Z=6$ ) to be estimated effectively by this method, the phase by phase chemistry is determined with a metals only analysis.
- The theoretical density is calculated using a rule of mixtures to be between 5.59 g/cc and 5.83 g/cc with the phase chemistry found by chemical analysis and volume fractions found by image analysis. The geometrically measured density is 5.52 g/cc. With these values, the expected porosity is between 1.2 – 5.6%. The measured value of 1.8 % from image analysis falls within the lower end of this range.

## **5. Mechanical properties of Ti(Mo)C-Ni cermets**

### **5.1. Introduction**

Cermets are structural composites in which the majority phase is a brittle ceramic and a minority (< 20 volume %) phase “binder” consisting of a ductile metal. They can be designed to exhibit a desirable combination of mechanical properties characteristic of both ceramics and metals such as high hardness, wear resistance, and acceptable levels of fracture toughness. Since these materials are primarily ceramic by volume fraction, the properties tend to be closer in behavior to that of the ceramic. As such, due consideration must be given to the presence of microstructural defects (pores, micro cracks, and surface irregularities) when evaluating mechanical properties.

### **5.2. Experimental procedure**

#### **5.2.1. Pulse-echo ultrasonic measurement of elastic moduli**

The elastic properties of the Ti(Mo)C – Ni sample were measured via the pulse-echo ultrasonic technique. In the ultrasonic technique, the speed of sound in the medium is measured, and the components of the stiffness tensor can be obtained given density. Given that the crystallographic texture has been confirmed to be random (see section 2.3.3), the material is assuredly isotropic via Neumann’s principle. Hence, the linear elastic stiffness tensor has only two independent components. For example, the components  $C_{11}$  and  $C_{44}$  can be determined using

measurements of the ultrasonic velocity of longitudinal (compression) waves and shear waves, respectively.

Samples are prepared as squares (of arbitrary size, provided the area is considerably larger than the ultrasonic transducer which are employed), each with a thickness that is less than 10mm. Thicker samples of this material would suffer from too much attenuation making the echoes difficult to resolve on the oscilloscope. In order to obtain precise measurements, the sample surfaces must be as flat and parallel as possible. As such, each sample was polished to a finish of  $1\mu\text{m}$ , with a slope less than .01 mm over the entire length ( $\sim 30\text{mm}$ ) of the specimen. The thicknesses of the samples were averaged across multiple measurements with a micrometer, across the plate as shown in Figure 34 below. Samples in both the as-received and HIPed condition are examined, and the determined thicknesses are shown in Table 21 below. The uncertainty in the thickness measurements is evaluated considering two possible sources: the resolution of the micrometer and the repeatability of the measurement.

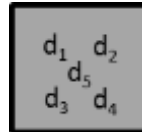


**Figure 34: Schematic of location of thickness measurements.**

**Table 21: Average thickness values of samples, standard deviation and total experimental uncertainty (with 95% confidence level)**

Sample	$d_{av}$ , mm	$\sigma_d$ , mm	$u$ , mm
AR1	5.5836	0.0121	$\pm 0.00546$
AR2	5.7422	0.0081	$\pm 0.00370$
AR3	3.4232	0.0076	$\pm 0.00348$
HP	5.3960	0.0089	$\pm 0.00405$

In order to measure the elastic modulus, a sinusoidal pulse is emitted from a Panametrics 5072PR pulser-receiver pulse generator to a Panametrics ultrasonic transducer with a center frequency of 2.25MHz, either longitudinal or shear. The signal then propagates through the medium, and reflects off of the back of the specimen. Finally the reflected wave is collected by the Tektronix TDS 3032C digital phosphor oscilloscope, and the time of flight can be observed as the time between two reflected peaks. In order to obtain a more accurate time of flight, the time between four reflected peaks is measured and the average spacing between two peaks is determined. Once the time-of-flight is obtained, the speed of sound in the medium is calculated with the classic kinematics formula,

$$v = \frac{2d}{t}$$

where  $v$  is the velocity (longitudinal or shear) of sound in medium,  $d$  is the sample thickness, and  $t$  is the time of flight. Once the velocities are known, components of the elastic stiffness tensor can be obtained with the following formulae:

$$v_L = \sqrt{\frac{C_{11}}{\rho}},$$

$$v_T = \sqrt{\frac{C_{44}}{\rho}},$$

If we assume that the material is isotropic,  $C_{11}$  and  $C_{44}$  are related to the Young's modulus,  $E$ , shear modulus,  $G$ , and the Poisson's ratio,  $\nu$ , as follows:

$$C_{44} = G; \quad C_{11} = \frac{E(1-\nu)}{(1+\nu)(1-2\nu)}; \quad G = \frac{E}{2(1+\nu)}$$

From these relationships,  $E$ ,  $G$ , and  $\nu$  can be calculated to be the following:

$$E = \frac{v_L^2 \rho (1+\nu)(1-2\nu)}{(1-\nu)}; \quad G = v_T^2 \rho; \quad \nu = \frac{\frac{1}{2} - \left(\frac{v_T}{v_L}\right)^2}{1 - \left(\frac{v_T}{v_L}\right)^2}$$

Figure 35 below shows a schematic of the setup used to collect the time of flight of both the longitudinal and shear waves through the cermet medium. Both the longitudinal and transverse transducers have a contact diameter of 1", and have a frequency of 2.25MHz. The ultrasonic transducer and oscilloscope system was operating at a pulse energy = 4 (104  $\mu$ J), pulse-receiver frequency (PRF) = 1 kHz, gain = 2.4 dB, damping = 3 (50  $\Omega$ ) using both high-pass and low-pass hardware filters.

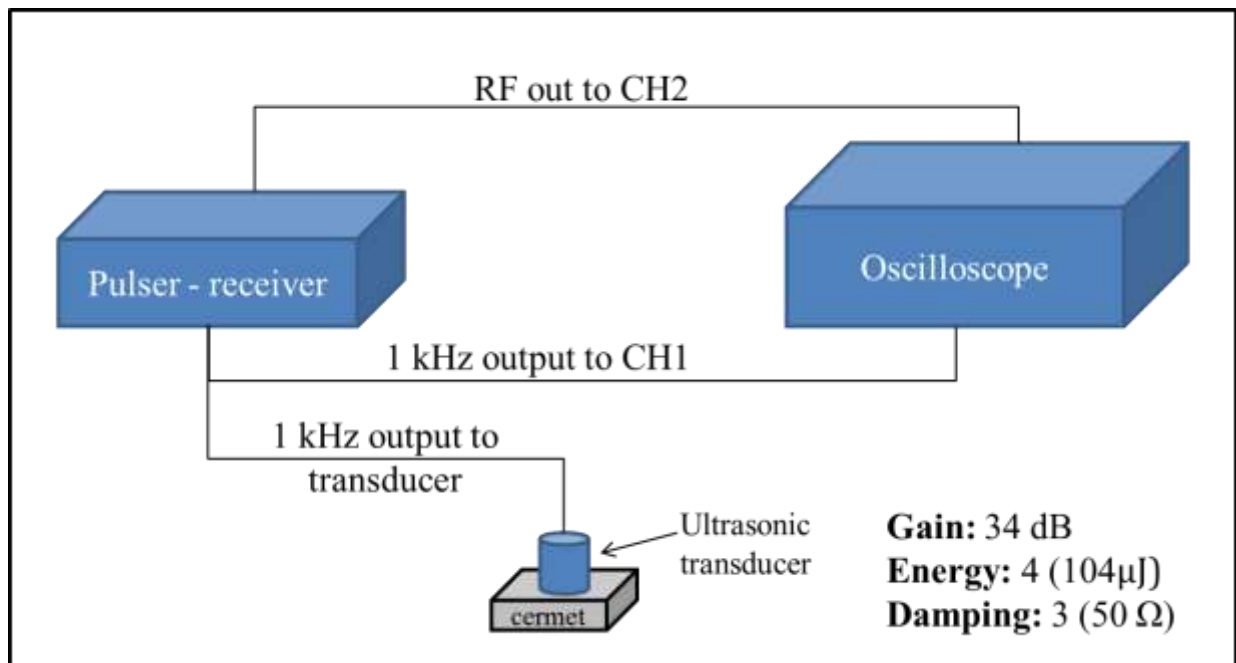


Figure 35: Schematic of experimental setup for ultrasonic elastic modulus measurements.

### 5.2.2. Hardness and Strength (Compressive and Flexural)

A standard Vickers pyramidal diamond indenter was used to determine the hardness of the cermet tile. Ten indents each were made on the as-received and HIPed material with a load of 1 kg and a dwell time of 15 s. The indent size was measured using an optical microscope and computer that permit digital image capture and analysis which are coupled with the indenter. Vickers hardness was calculated using the following formula:

$$HV = \frac{1.8544F}{d^2}$$

Compression testing was conducted on cylindrical samples of the cermet in accordance with ASTM standard E9-89a. The sample chosen was a right cylinder with a height to diameter ratio of 2.5:1, which is the recommended ratio for cemented carbides. Actual samples were 10 mm in diameter and 25 mm tall. Testing was completed on both the as-received and HIPed material, where the yield strength and elastic modulus were determined using ASTM standards E9-89a and E111, respectively. It is important to note that a limited number of samples were tested to failure due to the damage inflicted on the platens used. The platens were made of hardened steel with a Rockwell hardness of 975 HV, which is lower than the hardness observed for the cermet. Each sample was pre-loaded to 2 kN, loaded into 120 kN (which, given the cross-sectional area is still below the yield stress), and subsequently unloaded back to 2 kN. During the unload portion, the elastic modulus is measured. Next, the samples were either loaded until nonlinearity in the load-displacement curve was observed or to failure. Although expected to be very strong, the cermet is also suspected to be fairly brittle due to its high carbide content. It is expected to fail in a catastrophic manner that could damage the extensometer that is used to measure strain. As such, the extensometer is removed after the unload portion of the test. Utilizing the load-extension data from the remainder of the test, a compliance factor is determined and used to estimate the actual stress-strain curve for the cermet.

In order to assess the DDG-X cermet performance in bending, flexural testing was also performed. This testing was performed in accordance with ASTM standard C1161: Standard Test Method for Flexural Strength of Advanced Ceramics at Ambient Temperature. This method is preferred over the standards for metallic materials because it takes into account the flaws present in the cermet. The metallic method assumes a much higher tolerance for strain, which is

not expected in the cermet due to its high volume fraction of ceramic. This analysis is completed for 10 samples each of the as-received and the stress-relieved condition. The samples are rectangular bend beams which are nominally 8 mm x 52.5 mm x 3.5 mm. They are tested in four-point bending in which the outer span (40 mm) is exactly twice the inner span (20 mm). Load-deflection data is collected for the specimens as the samples are loaded until failure. Flexural strength is computed using the following formula:

$$\frac{3PL}{4bd^2}$$

Where  $P$  is the load,  $L$  is the difference between the outer and inner span,  $b$  is the width, and  $d$  is the thickness. After the load-deflection data is collected, the maximum load reached is used to calculate the flexural strength with the equation above. A small subset of samples for the flexural test was imaged after failure occurred in order to examine the failure surface.

### **5.2.3. Single edge v-notched beam fracture toughness testing**

Several recognized methods are available today for the evaluation of the fracture toughness of ceramic based material such as the single edge pre-cracked beam (SEPB), and the single edge notched beam (SENB). Due to unstable crack propagation properties however, these methods are often extremely difficult to realize. As a result modified methods have been developed and tested against traditional methods to compare reliability.

The method applied in this study is the single edge v-notched beam (SEVNB) method, as pioneered by Awaji et al. [29]. This method is a slight modification of the ASTM standard method E-399 in which the fatigue pre-crack at the end of the machined notch is replaced with a sharp notch. Results reported by Awaji show that this method is effective in estimating the plane

strain fracture toughness. A round robin study conducted by the Versailles Project on Advanced Materials and Standards also confirmed that this method provides consistent results, as long as the notch radius is maintained below twice the largest microstructural feature [30]. Considering the larger particles within the cermet, the notches in this experiment should be However, it has been shown that in the case of larger defects near the notch tip, the notches need not be as small [31]. The notches were introduced via polishing with a standard razor blade (thickness of about 250  $\mu\text{m}$ ), coupled with a 9  $\mu\text{m}$  diamond suspension followed with finishing with both a 3  $\mu\text{m}$  and 1  $\mu\text{m}$  diamond suspension. Due to the high hardness of the cermet, the notch in each specimen took an average time of 4 hours to introduce. Since the samples were also ground to 1200 grit on their faces (taking .5 hours) and 19 samples were prepared, this aspect of the research entailed many weeks. Figure 36 below shows a schematic of the sample geometry that was EDM wire cut from a bulk tile. The polished notch was introduced at the tip of the machined notch, as shown in Figure 37 below. A table of the notch radii and initial crack lengths can be found in appendix G.

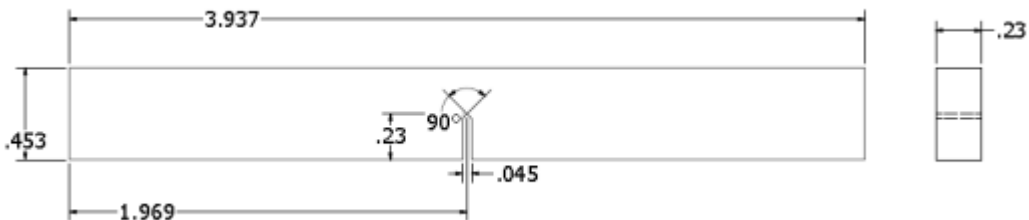


**Figure 36: Schematic of fracture toughness sample geometry. All dimensions are in inches.**

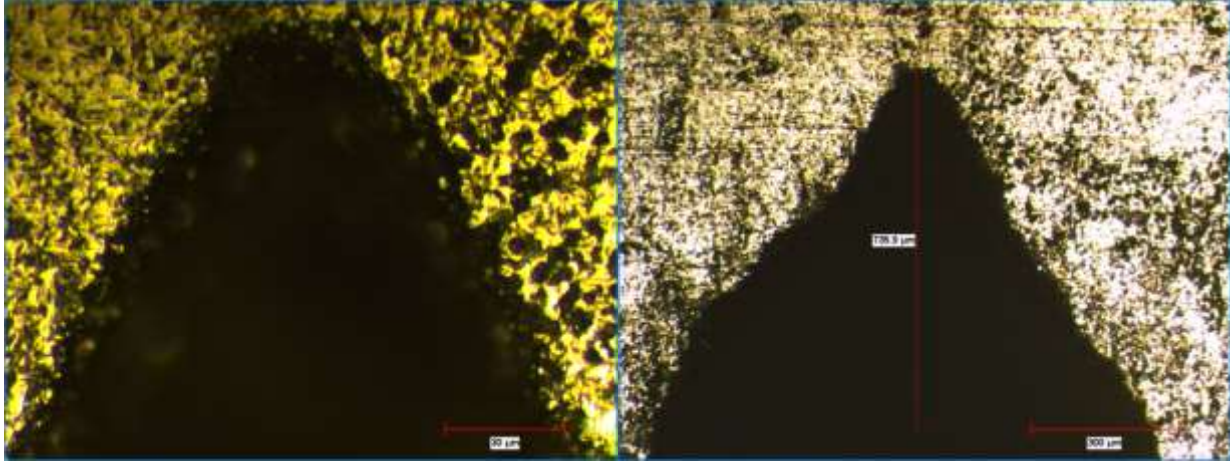


**Figure 37: Optical images of the polished notch prior to testing. The radius at the notch tip is approximately 30 $\mu$ m.**

In order to determine the effect of porosity on the fracture toughness values, samples were EDM wire cut from different sections of an 18 mm plate, to exploit the spatial differences in porosity observed. Four samples each were machined from opposite sides of one plate, since it was shown (in section 3.3.2) that there is strong through-thickness variation in the porosity. Tests were also completed for the HIPed sample to attempt to measure whether or not any advantage is provided over the as-received conditions.

The fracture toughness of the cermet was evaluated for both the as-received and post-HIP condition utilizing the equation developed by Wakai et al [29] :

$$K_I = \frac{3PS}{2BW^{2/3}} a^{1/2} Y$$

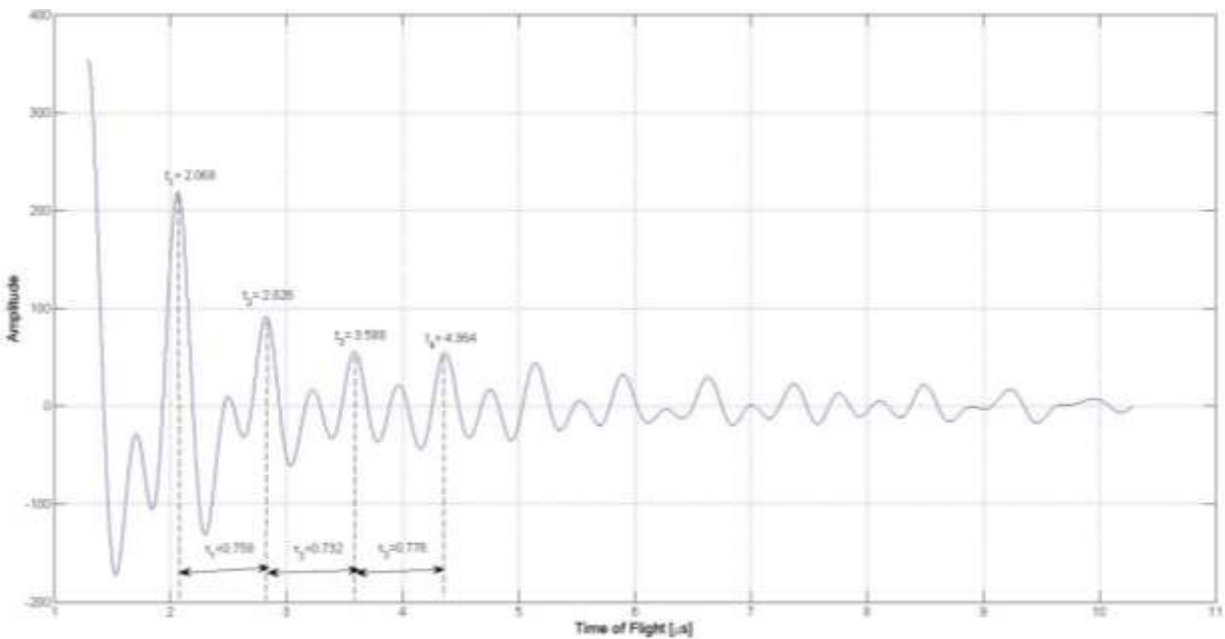
$$Y = 1.964 - 2.837 \alpha + 13.711 \alpha^2 - 23.250 \alpha^3 + 24.129 \alpha^4 ; \alpha = \frac{a}{W}$$

Where  $P$  is the maximum fracture load,  $S$  is the span,  $B$  is the thickness,  $W$  is the width,  $a$  is the pre-crack length, and  $Y$  is a shape factor.

## 5.3. Results

### 5.3.1. Elastic moduli

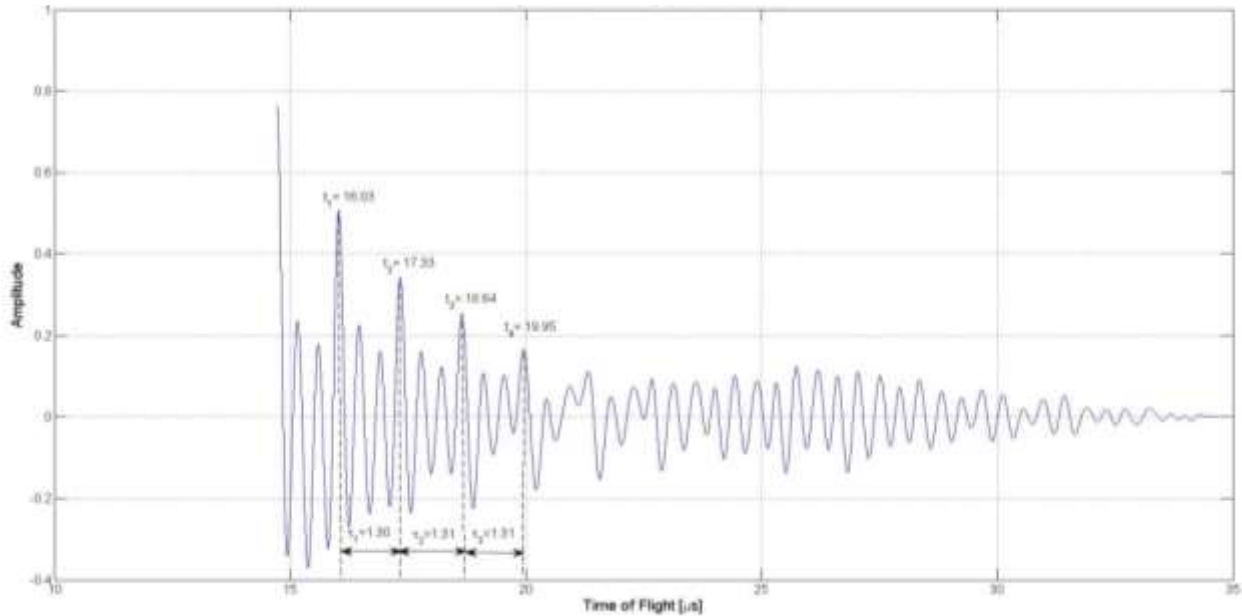
Four different samples were employed in this study – 3 as-received samples (denoted AR) and 1 HIPed sample (denoted H). Each of the samples is from a different initial bulk plate, with thicknesses varying from 8mm to 18mm. Figure 38 and Figure 39 below show examples of the longitudinal and shear waveforms obtained from each of the samples. In order to accurately determine the time of flight, an autocorrelation function is employed. Peaks in the autocorrelation are more readily identified than those shown in the raw data shown in Figures 38 and 39 below. Table 22 and Table 23 below show the collected time of flight measurements for each one, along with the associated uncertainty in each measurement. A detailed description of how the uncertainties are calculated can be found appendix H.



**Figure 38: Representative longitudinal waveform for an as-received sample. Waveform comes from sample AR3, and time of flight measurements are shown within.**

**Table 22: Average longitudinal measured time-of-flight and uncertainty**

Sample	$\tau_{av.}, \mu\text{s}$	$\sigma_{\tau}, \mu\text{s}$	$u, \mu\text{s}$
AR1	1.256	0.004	$\pm 0.003$
AR2	1.267	0.004	$\pm 0.003$
AR3	0.755	0.022	$\pm 0.013$
HIP	1.217	0.002	$\pm 0.002$

**Figure 39: Representative shear waveform for an as-received sample. Waveform comes from sample AR3, and time of flight measurements are shown within.****Table 23: Average shear measured time-of-flight and uncertainty**

Sample	$\tau_{av.}, \mu\text{s}$	$\sigma_{\tau}, \mu\text{s}$	$u, \mu\text{s}$
AR1	2.096	0.0058	$\pm 0.008$
AR2	2.153	0.0058	$\pm 0.008$
AR3	1.307	0.0058	$\pm 0.008$
HP	2.037	0.0058	$\pm 0.008$

Table 24 below shows a summary of the longitudinal and shear velocities along with the corresponding elastic constants. Taking an average of these four values, the elastic modulus of the material can be calculated as  $E=383$  GPa, the shear modulus as  $G = 155$  GPa, and Poisson's ratio as 0.232 using the equations shown in section 5.2.1.

**Table 24: Pulse- Echo Modulus results summary**

Sample	$v_L$ , m/s	$v_S$ m/s	$C_{11}$ , GPa	$C_{44}$ , GPa	E, GPa	G, GPa	$\nu$
AR1	8891	5326	436	156	382	156	0.22
AR2	9066	5333	454	157	387	157	0.23
AR3	9064	5239	454	151	378	151	0.25
H	8865	5298	434	154	378	154	0.22
AVG	8972	5299	445	155	382	155	0.23

### 5.3.2. Hardness and strength (compressive and flexural)

The hardness of the cermet in both its as-received and HIPed condition was measured to be  $1136 \pm 168$  HV and  $1373 \pm 265$  HV, respectively. The complete list of measurements can be found in appendix I. The hardness of the HIPed sample is significantly larger than that of the as-received condition, as confirmed by student's t-test.

For both the as-received and post-HIPed condition of the cermet, compressive failure was observed to be brittle in nature. The sample failed at a strain between 1-1.2% strain, having accumulated a plastic strain of only 0.3%. As such, the compressive strength is considered to be the compressive fracture strength. Table 25 below shows the compiled results for both conditions averaged over 6 samples (as-received), and 3 samples (HIPed). For the ultimate compressive strength, only two samples per condition were tested all the way to failure. Although it has been reported that evidence of localized shear and extensive micro cracking can be observed in polished samples after ballistic loading [32], no significant changes in the microstructure have been found between samples before and after deformation from the quasi-static loading. Imaging of the samples that were tested to failure could not be completed, as polishing the remains of the right cylinder samples was not possible due to the destruction of the sample. Figure 40 below shows compliance-corrected data for the compressive test. The data appear to be non-linear, which could potentially a result of simultaneous plastic deformation in the nickel phase, and

elastic deformation in the titanium carbide phase. A full listing of compression testing results can be found in appendix J.

**Table 25: Summary of mechanical properties obtained by compression testing**

	Property	Value	Standard deviation
<b>As-received</b>	.2 % yield strength	2.25 GPa	.21 GPa
	Elastic Modulus (unload)	330 GPa	60 GPa
	Ultimate compressive strength	2.67 GPa	.14 GPa
<b>Post-HIP</b>	.2 % yield strength	2.22 GPa	.17 GPa
	Elastic Modulus (unload)	323 GPa	30 GPa
	Ultimate compressive strength	2.62 GPa	.20 GPa

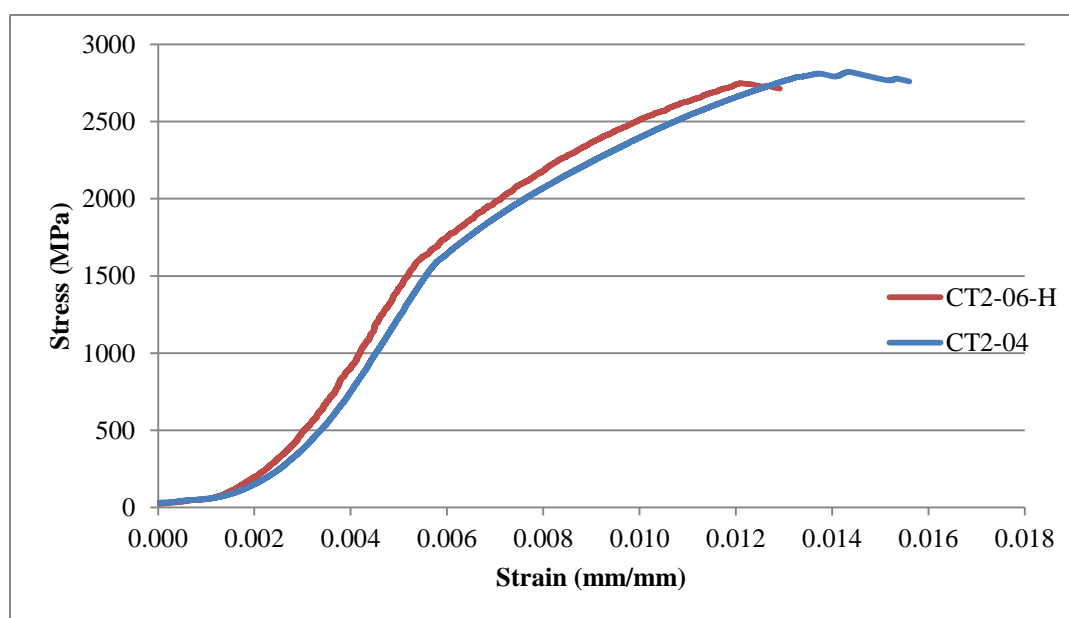


**Figure 40: Compression test results for as-received (blue) and HIP (red) cermet conditions**

Figure 41 below shows the results from the four point bending test. The results show that the flexural strength of the cermet is  $567 \text{ MPa} \pm 122 \text{ MPa}$ . The heat treatment is observed to have a flexural strength of  $528 \text{ MPa} \pm 148 \text{ MPa}$ , which is not significantly different from the as-

received material. As such, the entirety of the data can be used to perform a Weibull analysis on the results.

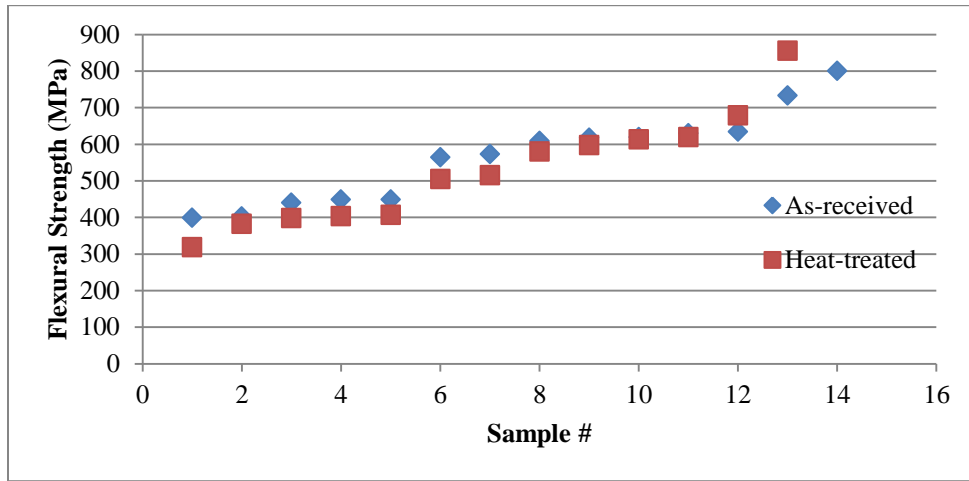


**Figure 41: Measured flexural strength of cermet for as-received and heat treated condition.**

Figure 42 below shows the Weibull distribution function for the flexural strength data. The red line indicates the probability of survival at a given stress level, and it is overlaid with the histogram data of the observed flexural strength. The Weibull distribution is given by the following equation [33]:

$$P_S(V_0) = \exp\left\{-\left(\frac{\sigma}{\sigma_0}\right)^m\right\}$$

Where  $P_S$  is the probability of survival for a given volume  $V_0$ ,  $\sigma_0$  is the Weibull characteristic strength (strength below which 37% of specimens will survive), and  $m$  is the Weibull modulus. In Figure 42 below, the dotted green line represents a probability of survival of 37%, corresponding to the Weibull characteristic strength, which can be used to calculate the Weibull modulus of 4.6. This value is much lower than the value anticipated by the vendor ( $m=15$ ) and indicates very stochastic behavior.

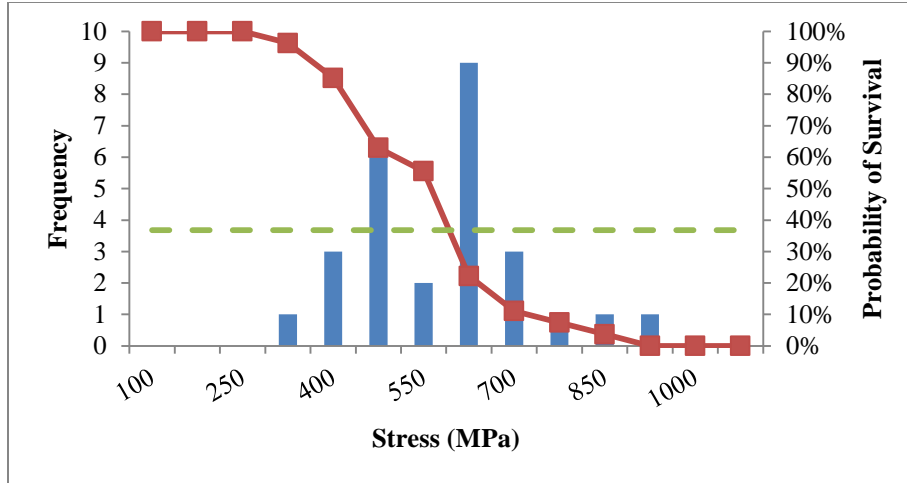


**Figure 42: Weibull distribution function overlaid with histogram data of the flexural strength testing. The red line indicates the probability of failure at the given stress level, and the dotted green line indicates a probability of survival of 37% (corresponds to the mean flexural strength).**

When compared with the compressive strength, the bend strength is observed to be significantly lower. As such, SEM microscopy of the failed bend beam samples was performed in order to determine the primary mode of failure. The micrographs revealed that fracture is the primary mode of failure. In Figure 43a and b multiple instances of fracture within the carbide phase is visible. Pores are also observed, and can be seen in Figure 43 a. Initially, the hypothesis was that large flaws within the cermet could be the cause of failure at such low stress levels. However, utilizing the conventional fracture mechanics formula

$$K_{1C} = \sigma \sqrt{\pi a_c}$$

where  $K_{1C}$  is the fracture toughness,  $\sigma$  is the applied stress, and  $a_c$  is the critical flaw size, the required pore size to cause such a failure can be calculated. Using the average bend strength measured, and the fracture toughness measured (see section 0), the critical flaw size is estimated

to be 230 $\mu\text{m}$ . After multiple specimens were examined in the SEM, this hypothesis was ruled out, as the largest flaws observed were on the order of 50 $\mu\text{m}$ .

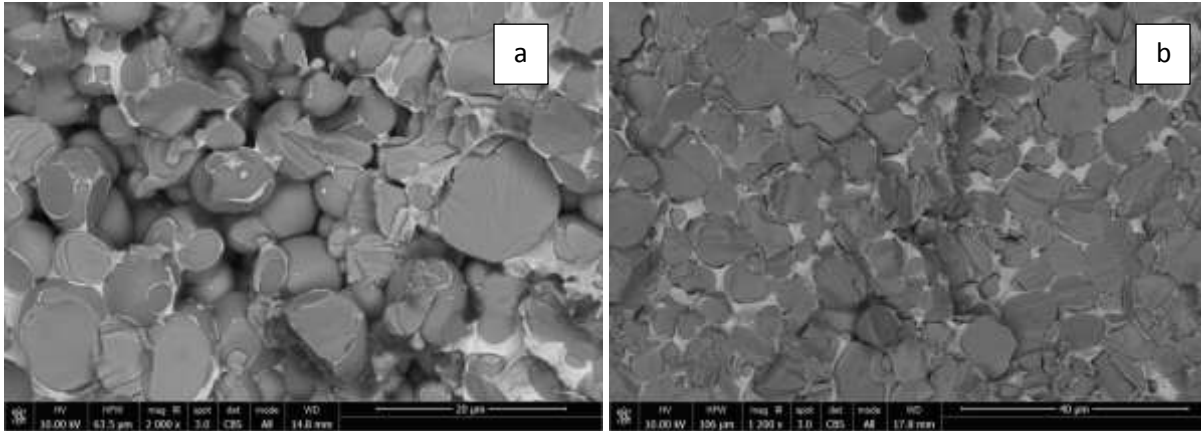


**Figure 43: Example SEM micrograph of fracture surface of bend beams after testing.**

### 5.3.3. Fracture toughness

The shape of the load curve revealed that the material fractures in a brittle manner, meaning that the maximum load is also the failure point of each specimen (see appendix K). Figure 44 below shows the results obtained for all of the as-received conditions, as well as the HIPed condition. The data reveal that the three as-received conditions are no different from one another. As such, their values can be averaged to yield an overall as-received fracture toughness of 15.2  $\text{MPa}\cdot\text{m}^{1/2}$ . The HIPed specimens have an average fracture toughness of 17.2  $\text{MPa}\cdot\text{m}^{1/2}$ .

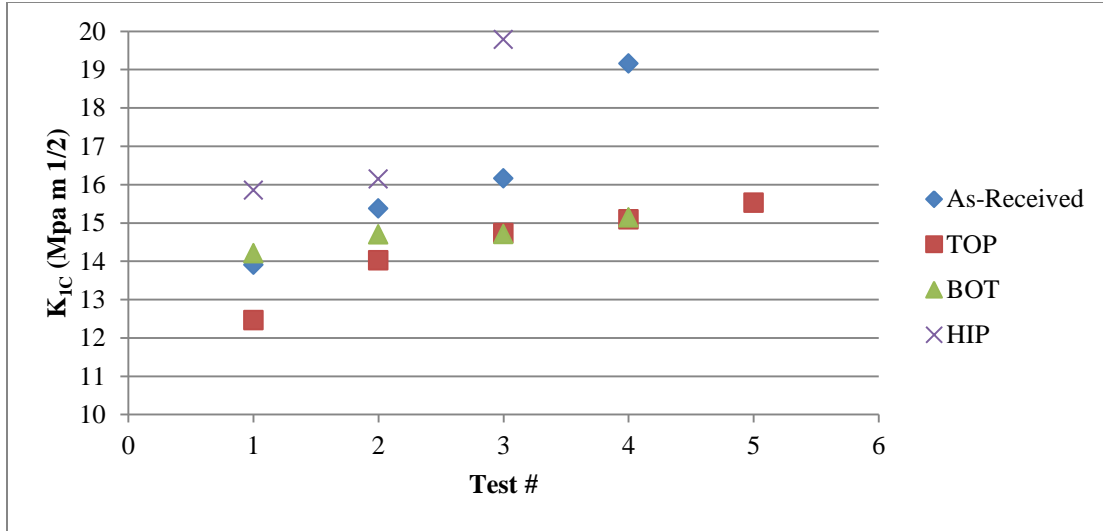


**Figure 44: Fracture toughness values for all conditions. As-received, top, and bottom all come from different as-received plates.**

**Table 26: Summary of fracture toughness results for all conditions**

	Sample condition	$K_{IC}$ MPa-m <sup>1/2</sup>	$\sigma$ MPa-m <sup>1/2</sup>
As-received	As-received	16.49	1.94
	Top	14.37	1.2
	Bottom	14.69	0.38
	<b>Average</b>	<b>15.2</b>	<b>1.2</b>
Hot Isostatic Pressed		17.26	2.19

The difference in properties of the two phases within the cermet is evident upon viewing the fracture surface. Figure 45 below shows a micrograph of the cermet that exhibits brittle fracture in the carbide particles as evidenced by flat, cleaved planes. The micrograph also shows the ductile nature of the metal matrix, which is observed as the elongation of the matrix around the carbide particles. Figure 45 also shows a characteristic porosity that is not immediately apparent from the sample preparation. On the portion of the micrograph labeled “porous”, it is observed that the carbide particles do not have any surrounding metal matrix. In each case, this

phenomenon is observed to be localized toward one side of the specimen, suggesting that it could be processing induced.

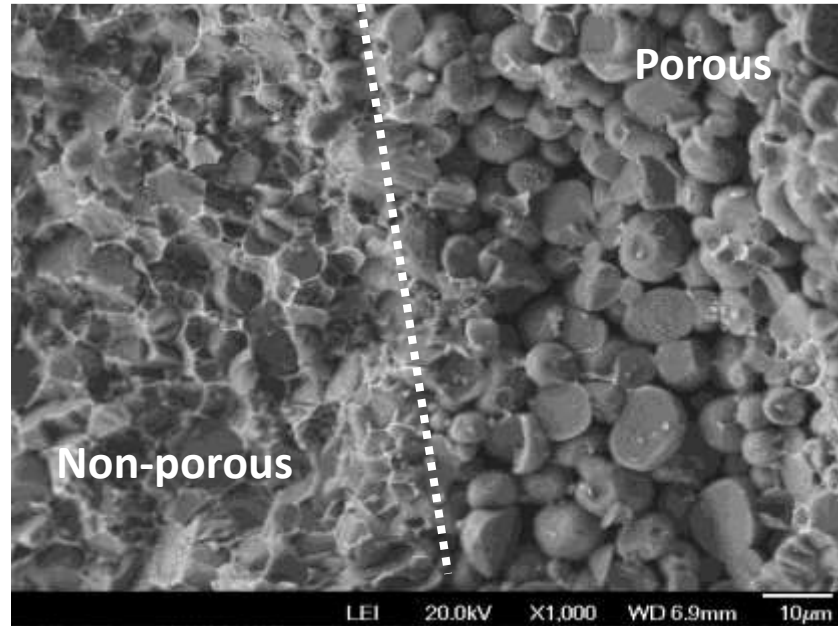


**Figure 45: Fracture surface of as-received DDG-X cermet**

#### 5.4. Discussion

The elastic modulus was also calculated via rule of mixtures to gain a point of reference. The moduli listed for titanium carbide and nickel are  $E_{TiC} = 436$  GPa,  $G_{TiC} = 193^3$  GPa,  $E_{Ni} = 207$  GPa,  $G_{Ni} = 76$  GPa [34]. Given these values, we can obtain the Poisson's ratio for both phases as  $\nu_{TiC} = 0.2$ , and  $\nu_{Ni} = 0.36$ . Applying the following Voight upper-bound rule of mixtures formula, and volume fractions calculated from the image analysis, the composite moduli are estimated to be  $E_C = 403$  GPa, and  $G_C = 172$  GPa, and  $\nu_C = 0.22$ .

$$Q_C = w_{TiC}Q_{TiC} + w_{Ni}Q_{Ni}$$

<sup>3</sup> Given as a range from 110-193 GPa.

Where  $Q$  is the given property ( $E$ ,  $G$ , or  $\nu$ ), and  $w$  is the respective volume fraction. In this case, the relation  $w_{TiC} + w_{Ni} + vol \% porosity = 1$ . The presence of porosity will cause a subsequent decrease in any property calculated, but given the measured porosity in the cermet the decrease is expected to be negligible. Applying the following Reuss lower bound rule of mixtures, the composite moduli are estimated to be  $E_C = 388$  GPa,  $G_C = 155$  GPa, and  $\nu_C = 0.22$ .

$$Q_C^{-1} = w_{TiC}Q_{TiC}^{-1} + w_{Ni}Q_{Ni}^{-1}$$

Where  $Q$  is the given property ( $E$ ,  $G$ , or  $\nu$ ), and  $w$  is the respective volume fraction. Lastly, the two obtained values can be averaged for a Hill estimate, which yields values of  $E_C = 395$  GPa,  $G_C = 160$  GPa, and  $\nu_C = 0.22$ .

It should be noted that the results for elastic modulus as obtained by compression (330 GPa) testing was much lower than measured with the ultrasonic technique (383 GPa), or even the lower bound rule of mixtures calculation (388 GPa). Figure 46 illustrates the upper (Voight) and lower (Reuss) bounds for a rule of mixtures with this material system and the ultrasonic measured modulus over the range of possible carbide phase volume fractions. It is shown that the measured value is well-bounded by the two limits which assume either equal strain (Voight) or equal stress (Reuss) between the two phases. Since this is not the ideal fiber-matrix case often considered (uni-directional, equal fibers embedded in a matrix), this cermet is expected to have a modulus in between the two bounds. At such a high volume fraction, the proximity of the particles is expected to have an impact. For example, wherever there is contact between two or more particles, a force chain can exist between them. This phenomenon is sometimes referred to as “jamming”, and it plays a large role in the observed properties at such high volume fractions [35]. The discrepancy in the modulus measured by compressive testing could also be a result of these complex interactions between the phases during testing.

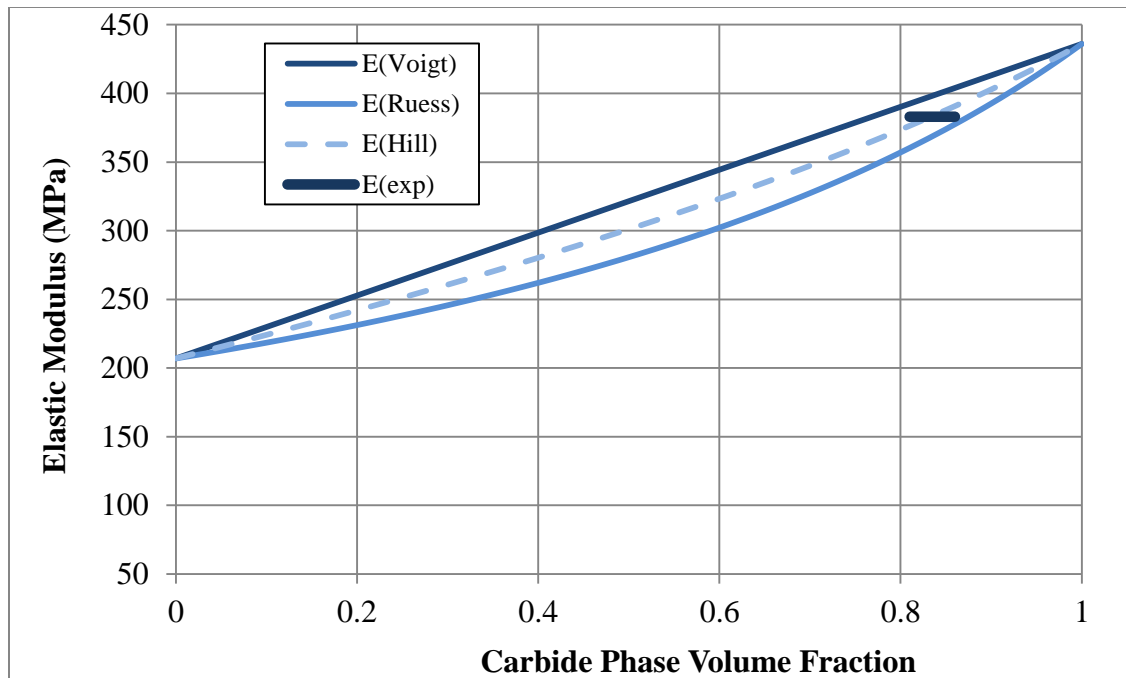


**Figure 46:** Plot illustrating upper (Voigt), lower (Reuss), and average (Hill) rule of mixture boundaries for elastic modulus.

It is likely that the Ni binder is deforming plastically while the TiC phase is still in its elastic region, which would explain the lower apparent modulus during the compression test. In a metallographic analysis after impact loading, Compton and Zok [32] observed significant plastic flow in the Ni binder, as well as micro cracking in the TiC phase. Although the nature of the loading is different, it provides confirmation that the two phases impose a constraint on one another such that they can be in drastically different states at the same time. Ultimately, the relationship between stress and strain for this composite material simply may not be linear.

The flexural strength (~520MPa) of the cermet was measured to be approximately 20% of its compressive strength (~2620 MPa). Much of the discrepancy is attributed to the cermet's poor tensile strength, but the magnitude of the difference suggests that there may be other influencing factors. As previously mentioned, with the average measured toughness of 15.2

$\text{MPa}\cdot\text{m}^{1/2}$ , a critical flaw size is estimated to be  $\sim 230\mu\text{m}$ , which is unreasonably large (calculated with conventional fracture mechanics relationship  $K_{1C} = \sigma\sqrt{\pi a}$ ). LaSalvia and Meyers [7] show that the flexural strength changes drastically with Mo content due to the change in bond strength between the two phases. It is possible that even a small amount of porosity in the specimens could affect the measured flexural stress. The obtained result is also much lower than estimated by the vendor (900-2000 MPa). It is unclear whether these values are measured or estimated based on other known properties of the cermet.

The full set of measured and inferred mechanical properties are summarized in

Table 27 below. Once these results are collected, some preliminary microstructure-process-property relationships can be speculated.

**Table 27: Property summary for Ti(Mo)C-Ni cermet**

<b>Property</b>	<b>Value</b>
<b>Bulk density</b>	5.52 g/cm <sup>3</sup>
<b>Average grain size</b>	9.13 $\mu\text{m}$
<b>Flexural Strength (4-pt-bend)</b>	520 MPa
<b>Compressive Strength</b>	2.72 GPa
<b>Elastic Modulus</b>	383 GPa
<b>Poisson's ration</b>	0.23
<b>Hardness (Vickers)</b>	1140 HV
<b>Fracture Toughness</b>	15.2 $\text{MPa}\cdot\text{m}^{1/2}$
<b>Shear Modulus</b>	155 GPa
<b>Bulk Modulus</b>	240 GPa
<b>Longitudinal Wave Velocity</b>	9007 m/s
<b>Transverse (Shear) wave velocity</b>	5300 m/s

Although the elastic properties were found to adhere to a rule of mixtures formula, the strength properties did not. This potentially indicates that the strength properties are sensitive to more than just the volume fraction of the phases. Compton and Zok [32] conclude that these properties are fairly dependent on the topology observed in the microstructure. The topology of this cermet can be described as discrete ceramic particles surrounded by a nickel matrix. Its

continuous nature allows for the softer metal matrix to flow plastically as the ceramic particles continue to absorb elastic energy from the loading source [32]. Other authors have found that a lack of continuity (in this case porosity), could lead to a decrease in the fracture toughness, as the crack propagation through the cermet is not slowed by the tougher metal binder [11,40]. In the TiC/Ni system, this continuity is addressed through the processing in two ways: improving the phase to phase wetting with an elemental add-in, and decreasing the porosity through a pressing action (which in this case is a lack of Ni binder).

A number of different factors can affect the fracture toughness measurement collected. First, the amount of binder between particles can toughen the bulk material by preventing a continuous fracture path through the TiC phase [28]. For this same reason, observed porosity in the solid could potentially accelerate fracture since the absence of material provides no resistance. The amount of molybdenum present in the sample can also affect the toughness measured. As molybdenum is added, it can affect the flow stress of the binder, which can change its ability to resist fracture [13]. The presence of residual stresses could also affect the toughness value. If there are macro stresses present, the material will fracture at a lower applied stress than the material property would indicate. These stresses could be introduced through either the material synthesis process, or potentially the EDM wire cutting of the samples due to the localized melting that occurs during the process. Lastly, with this method the radius of the notch introduced could affect the numerical value of the result obtained. Previous research has shown that notch radii that are greater than twice the largest microstructural feature could result in a false-high value [30]. In the case of this study, the largest particles observed have an approximate three-dimensional diameter of 22  $\mu\text{m}$ , meaning the largest acceptable notch radius is approximately 44  $\mu\text{m}$ . As shown in Figure 47, the majority of samples tested fall below that

limit. No definitive trend in the measured fracture toughness values was observed for an increase in notch radius.

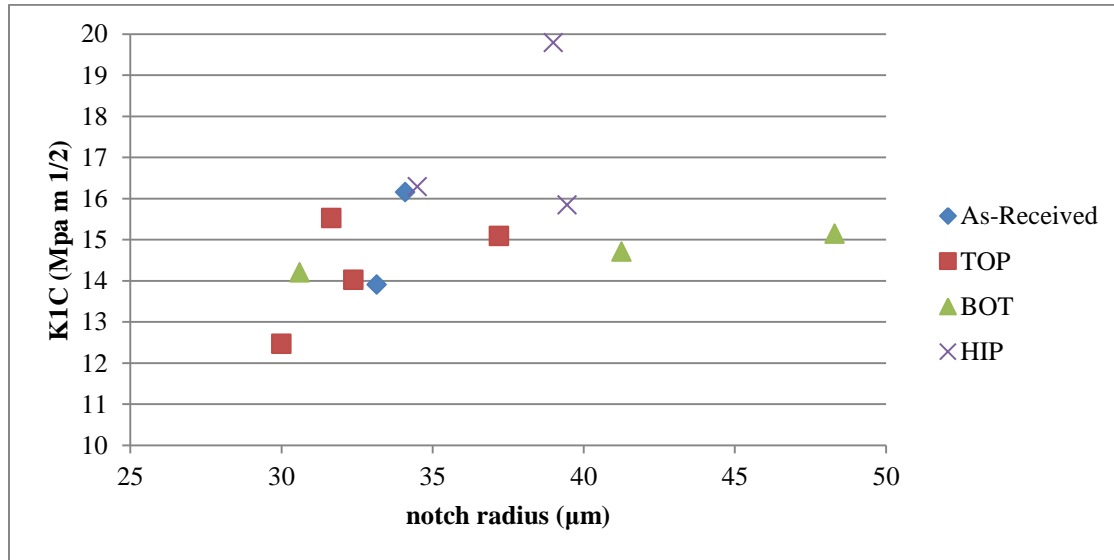


Figure 47: Fracture toughness versus notch radii for all samples tested via single-edge v-notch beam method.

## 5.5. Conclusions

- Elastic properties of the cermet is found via pulse-echo ultrasonic techniques to be  $E = 383$  GPa,  $G = 155$  GPa, and  $\nu = 0.23$  for the as-received condition. The HIPed condition is found to have values of  $E = 378$  GPa,  $G = 154$  GPa, and  $\nu = 0.22$ . The Hill rule of mixtures (with the given phase volume fractions) predicts these properties to be  $E = 382$  GPa,  $G = 156$  GPa, and  $\nu_c = 0.22$ , which is within 1% of the measured properties.
- Vickers microhardness testing show the cermet hardness to be  $1136 \pm 170$  HV for the as-received condition, and  $1373 \pm 265$  HV for the HIPed condition.
- Compression testing via ASTM E9-89a reveals the as-received cermet to have a 0.2% yield strength of  $2250 \pm 210$  MPa, and an ultimate compressive strength of  $2670 \pm 139$

MPa. The HIPed material is found to have a 0.2% yield strength of  $2220 \pm 170$  MPa, and an ultimate compressive strength of  $2620 \pm 200$  MPa.

- Flexural testing via ASTM C111 reveal the modulus of rupture via four point bending to be  $570 \pm 120$  MPa for the as-received condition, and  $530 \pm 150$  MPa for the stress-relieved condition.
- The Weibull modulus is calculated to be 4.6, meaning that the mechanical properties have a great amount of variability, and the probability of a survival for a given sample decreases very rapidly as its stress constant value is reached. This cermet is estimated to have a stress constant of
- The fracture toughness is measured via the single-edge v notched beam technique to be  $15.2 \pm 1.1$  MPa·m<sup>1/2</sup> for the as-received material, and  $17.3 \pm 2.2$  MPa·m<sup>1/2</sup> for the HIPed material.
- There is no significant difference between the properties as-received, stress-relieved, and HIPed conditions. The results for elastic modulus, compressive strength, flexural strength, density, hardness and grain size were all found to be within experimental uncertainty to one another. Although a small increase in the fracture toughness is observed for the HIPed condition, the sample size is not large enough to assert that the average value is not comparable to that of the as-received condition.

## 6. Joining of cermet structures using brazing

*In the interest of full disclosure, the author would like to highlight that a portion of the material contained in this chapter represents work conducted by colleagues Dong et al. [36]. This unpublished material is complementary to the present project and provide an application of the results obtained throughout the rest of this thesis project. Such results will be highlighted with attribution to those scientists.*

### 6.1. Introduction

The mechanical properties of the Ti(Mo)C-Ni cermet are being evaluated for use in octet- truss sandwich panel structures consisting of a truss core encased by two solid face sheets. This particular truss design is known to be stretch governed. This means that the observed compressive strength of the structure scales with its relative density  $\bar{\rho}$ , which provides a great advantage over bending-governed designs which scale with  $\bar{\rho}^{-1.5}$  [5]. If very thin members of the cermet were employed, an Euler elastic buckling limit could be approached. If the loading resulted in buckling, bending could become a factor even within this stretch-governed design. However, the aspect ratio of the members employed (see below) make the bending fracture limitation less likely. Even if the joints within the cellular structure were of infinite strength, the fracture behavior of the cermet members would still limit the strength of the structure. As such, the target of the joining process is to develop a joint with integrity which is able to survive loads and moments in excess of those which the cermet can survive.

Metal joining techniques are sufficiently strong to hold stainless steel sandwich panels together, but it is currently unknown how most of these techniques would work with the cermet. All techniques that involve drilling, fasteners, or forming were not considered as they would likely cause fracture in the joining process. Diffusion bonding, which has successfully been employed for Ti-based cermets [37], was not considered either. Welding is not an option because

the melting point of the TiC majority phase is approximately 3065 °C. Vacuum furnace brazing emerges as the most viable option, since it does not require sectioning, but the potential of inducing large thermal stresses or producing a weak joint are legitimate concerns that must be addressed. The work presented in Chapter 2 provides guidance for the avoidance of thermal residual stresses during high temperature processing.

Vacuum furnace brazing operates by joining two materials (typically metals) by melting a filler metal. Through capillary action, the filler metal will alloy with the base material, thus producing a metallurgical bond [38]. The strength and performance of the joint produced depends directly on the compatibility of the filler metal chosen, and the type of joint used. Since the ability of the filler metal to exhibit capillary flow is affected by the wetting behavior and surface roughness of the base material, three surface configurations were examined. One pair each of (i) electric discharge machine, (ii) ground was analyzed.

For this study, only one filler metal and joint type was examined in order to get a preliminary idea of how viable this method is for joining cermet to cermet for sandwich panel structures. This information was then used in a related study, which performed a preliminary test of three different unit cell geometries to ascertain whether or not the joint would be a limiting factor in the design. The results from this complementary study are also presented in the results section.

## **6.2. Methods**

The filler metal chosen for this study was Nicrobraz 51 ©, which boasts a strength higher than that of stainless steel as well as good oxidation and corrosion resistance. This filler has a composition (in wt.%) that is 65 % nickel, 25% chromium, and 10% phosphorous. The majority of the phosphorous is expected to be released in the brazing process, which leaves the nickel and

chromium to form an alloy with the Ti(Mo)C-Ni cermet. Since the vast majority of the metal binder in the cermet is nickel, which has a high solid solubility with chromium, the compatibility of the joint is expected to be high. The chosen joint configuration is a simple lap joint formed by two rectangular bars of size 45mm x 11.5mm x 8.11mm. The lap joint area was approximately 11.5mm x 11.5mm.

Per the filler metal manufacturer instructions, the Nicrobraz 51 © filler metal powder is combined with its recommended water-based gel suspending agent (Nicrobraz 'S' Binder ©) in order to create a paste (88% powder, 12% gel). The paste is then applied to the intended joint area of the cermet, and the two pieces of cermet are held in place for a minimum of 8 hours to allow the paste to dry. The target gap size of the braze in the joint is 50µm [38]. The gel binder will completely volatilize during the brazing process.

Once the braze joint is completely dry, the vacuum process may be started. First, the vacuum furnace chamber is vented, and the braze joint is placed on a boron nitride tile inside. Next, the chamber is evacuated to a vacuum pressure below  $10^{-6}$  torr. Once the vacuum is achieved, the furnace cycle is started. The furnace cycle consists of a series of temperature ramps and hold segments at values recommended by standard industry practice [39]. The first hold segment of 5 minutes (150°C) allows for outgassing of any solvents to prevent holes in the final brazed joint. The second hold segment of 5 minutes (550 °C) allows for the gel binder and the phosphorous in the braze paste to become gaseous and evaporate. The next hold segment is for 30 minutes at the braze temperature (1050 °C), and it is at this point that the braze melts and begins to flow within the joint, and ideally form alloys with the base material. The final hold segment of 10 minutes (800 °C) simply allows for the brazed joint to reach thermal equilibrium in its solid state. All ramps have a rate of 15°C/min to prevent thermal cracking due to the

mismatch in coefficient of thermal expansion of the various phases (carbide, Ni binder, and various Ni-rich and Cr-rich phases which form in the braze filler metal). The full cycle can be viewed in Figure 48. Recall that a cooling rate of 15 °C/min was revealed (in Chapter 2) to minimize thermal residual stresses in the cermet itself, and the thermal mismatch between the braze phases and the cermet phases are no greater than those inherent to the cermet itself.

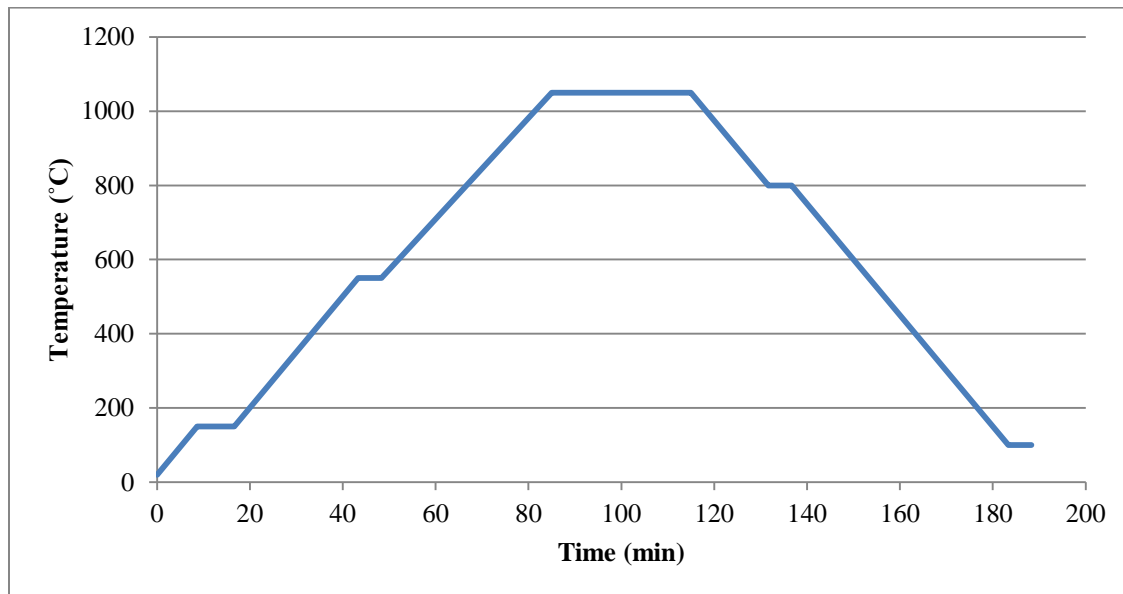


**Figure 48:** Graph of furnace temperature cycle for brazing of cermet to cermet with Microbraz © filler metal.

After the brazed joints had completely cooled, the two joints were polished and micrographs were collected to examine the gap size, and the bond made between the two rectangular solids. This analysis was also completed for the midsection of the joint to confirm that it was the same throughout. EDS was also performed in order to determine the alloys that were formed during the brazing process. Table 28 below shows the polishing regimen for these samples.

**Table 28: Polishing regimen for brazed joint samples.**

Grinding/Polishing Disc	Grit Size	Time polished (min)
MD Piano	220	1:30
MD Piano	500	1:30
MD Piano	1200	1:30
MD-Allegro	9 $\mu$ m	1:30
MD-DAC	9 $\mu$ m	4:00
MD-DAC	3 $\mu$ m	4:00
MD-DAC	1 $\mu$ m	4:00
MD-CHEM	.25 $\mu$ m	4:00

After demonstrating successful brazes (result below) using the above protocol, this same brazing cycle was used for the assembly of the cermet unit cells for use in a sandwich panel in a parallel study conducted by Dong et al. [36]. In this study, three relative density unit cells were assembled, and tested in compression. Figure 49 below shows how the trusses were assembled utilizing the vacuum furnace brazing for a relative density of  $\bar{\rho} = 4.97\%$ . The trusses are EDM wire machined into shapes that will “snap-fit” into the face sheets, and the braze paste is placed within the joint. The final assembly is then tested in compression at a loading rate of 0.2 mm/min until failure occurs.

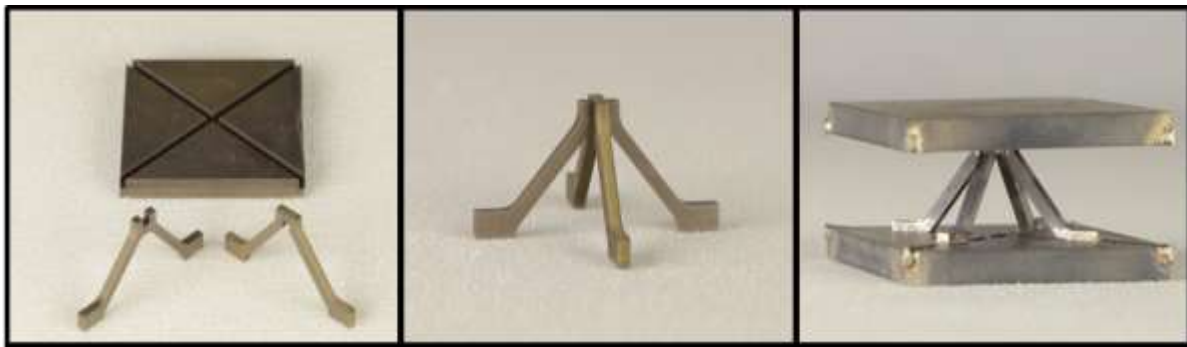


**Figure 49: Assembly process of pyramidal truss structures assembled in a parallel study [36]**

### 6.3. Results and Discussion

Figure 50 below gives representative images of both the joints produced with the ground surfaces and the EDM wire cut surfaces. It is observed that the gap size achieved with the EDM surfaces is smaller than achieved with the ground surfaces, and much closer to the recommended size of 50 $\mu\text{m}$ . This is fortunate because EDM fabrication is used to cut the snap-fit truss members employed later in this study. It is encouraging that the surfaces appear sufficiently smooth to making quality braze joints. Chromium-rich particles can be observed within the center of the joint, and throughout the metal binder of the cermet as dark grey solid shapes. This is confirmed by the EDS analysis presented later. Both joints seem to have good contact with the surfaces of the two solids joined together.

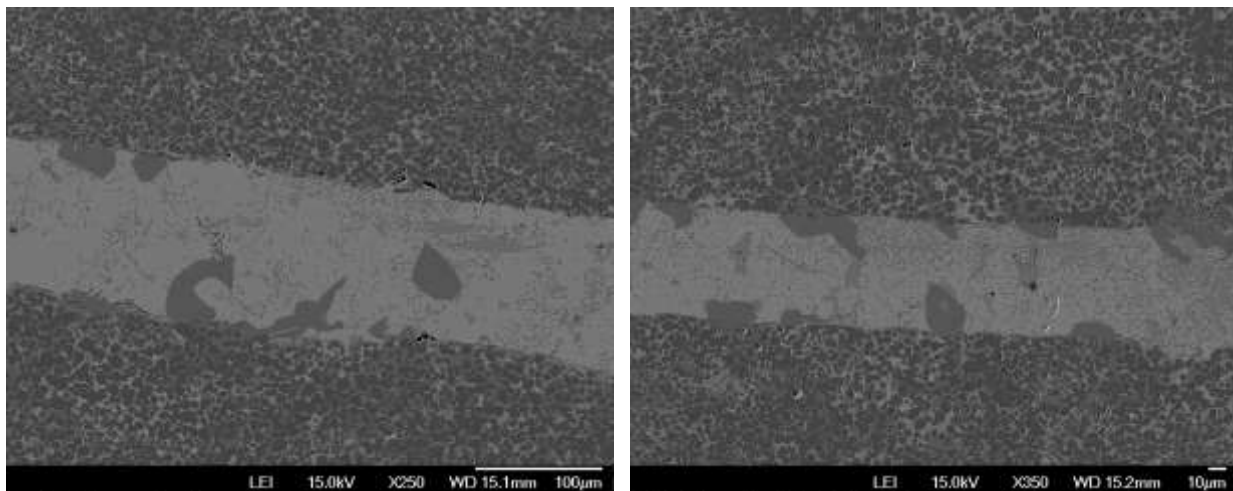


**Figure 50: Representative images of the braze joints for the ground surfaces (left) and the EDM surfaces (right).**

A metals only EDS line scan analysis was performed to gain some clarity on the location of the metals that are known to be present. As shown in Figure 51 and Figure 52 below, the medium gray particles (darker than the Ni binder for the cermet, lighter than the TiC) are

confirmed as chromium. It is also observed that these chromium particles are observed as far away from the joint as 300 $\mu\text{m}$ .

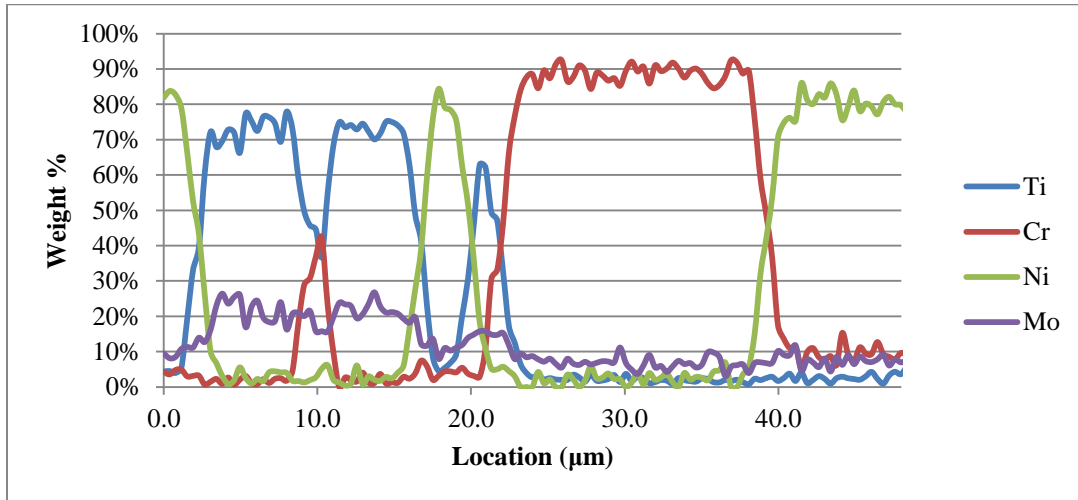


**Figure 51: Line scan analysis of EDM surface braze joint. The dark grey solids within the joint and within the binder are confirmed as Cr based particles.**

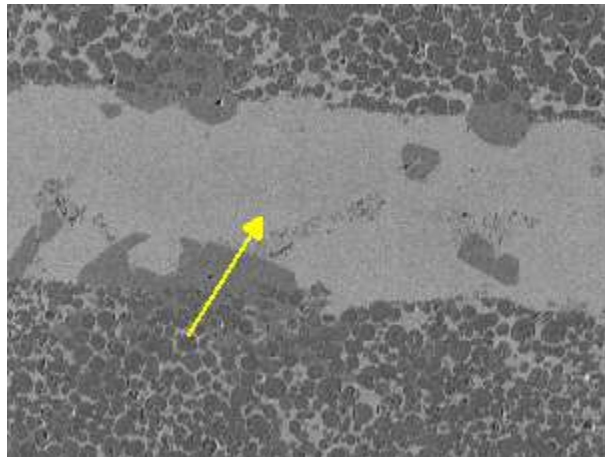


**Figure 52: Micrograph corresponding to line scan analysis in the above figure.**

When tested in compression, the pyramidal lattice structure exhibited the stress-strain response shown in Figure 53 below. The unit cell was observed to fail in the base material, and not at the braze joint. This confirms that the brazed joint is of adequate strength to be used in the assembly of sandwich panel structures with cermet materials.

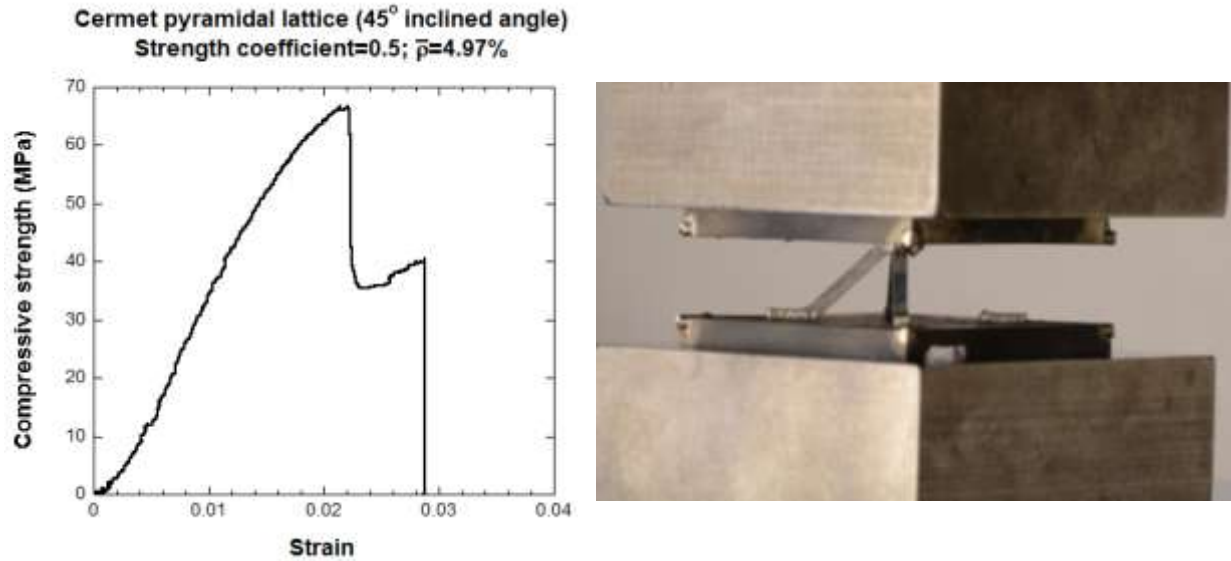


**Figure 53: Stress-Strain response of cermet pyramidal lattice structure with relative core density of 4.97% (left), and image of failed sample (right). This testing was completed in a parallel study [36]**

The result obtained shows that the unit cell has a strength of  $\sim 70\text{MPa}$ . As mentioned previously the relative density of this unit cell is 4.97%. The effective density of the unit cell can be calculated as  $270\text{ g/cc}$ . Once this result is obtained, the performance can be placed on the same strength-density plot as mentioned in Chapter 1. It is shown in Figure 54 below as a red dot, and it is observed that the performance falls just outside of the desired range for impact loading.

The performance is however consistent with the relationship defined by Deshpande and Fleck for an out of plane compression mode [46-47] as described below:

$$\sigma_c = \sigma_{strut} \bar{\rho} \sin^2 \omega = (2670\text{ MPa})(.0497) \sin^2 45 = 66.3\text{ MPa}$$

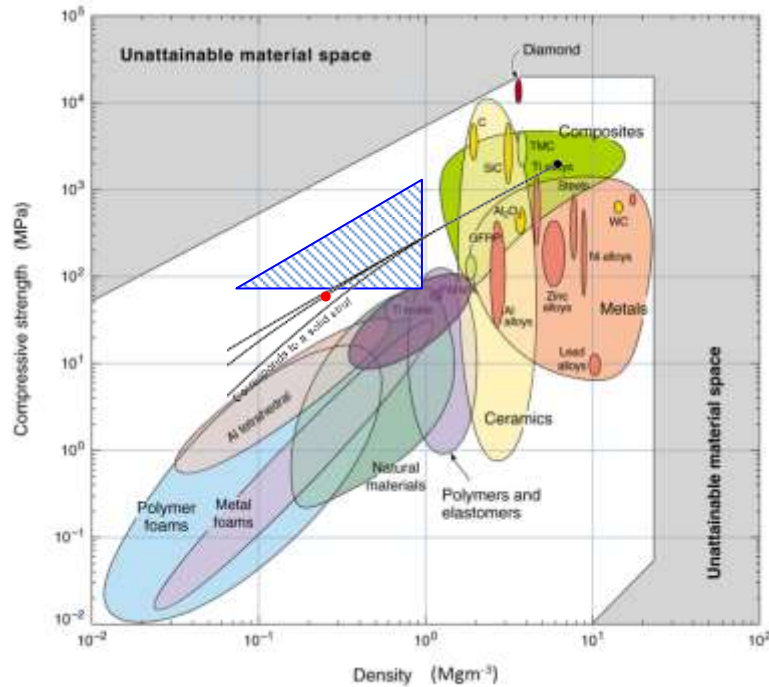


Figure 54: Ashby style plot of compressive strength vs. density. The grey unattainable material space is defined by the Hashin bound. The TiC/Ni cermet used in this study is shown by the black dot. The properties observed for the unit cell structure is shown by the red dot. [2]

## 6.4. Conclusions

- The EDM surface provides sufficient roughness for an adequate braze joint.
- From these joining results, we can conclude fairly simply that brazing is an adequate method for use with cermet-based sandwich panel structures. Since failure occurred within the strut, and not within the joint itself – the strength of the braze joint is not a limiting factor in the design.
- The pyramidal unit cell (relative density of 4.97%) was found to have a compressive strength of  $\sim 70$ MPa. This result confirmed that the response of the structure adheres to the relationship developed by Deshpande and Fleck [40] to describe the performance of pyramidal lattice structures.

## 7. Conclusions and Future Work

### 7.1. Conclusions

The following is a summary of the results obtained by all of the methods employed in this thesis. All of these facts together confirm that TiC/Ni cermets are promising candidates for use in sandwich panel structures.

The morphology and spatial dependence in porosity suggest that the tiles were produced via combustion synthesis coupled with a single action pressing action. A single action press would produce a pressure gradient in the green compact, and a subsequent gradient in density observed in the final synthesized tiles. The theoretical density is calculated using a rule of mixtures to be between 5.59 g/cc and 5.83 g/cc with the phase chemistry found by chemical analysis and volume fractions found by image analysis. The geometrically measured density is 5.52 g/cc. With these values, the expected porosity is between 1.2 – 5.6%. The measured value of 1.8 % from image analysis falls within the lower end of this range.

Property	Symbol	Value	HIP Value
Elastic modulus	E	383 GPa	378 GPa
Shear modulus	G	155 GPa	154 GPa
Poisson's ratio	$\nu$	0.23	0.22
Vickers microhardness	HV	1120±170 HV	1570 ± 230 HV
Compressive Yield Strength (.2%)	$\sigma_{YS}$	2250 ± 210 MPa	2220 ± 170 MPa
Compressive strength	$\sigma_{UTS}$	2670 ±139 MPa	2620 ± 200 MPa
Flexural Strength		570 ± 120 MPa	530 ± 150 MPa
Fracture Toughness*		15.2 ± 1.1 MPa·m <sup>1/2</sup>	17.3 ± 2.2 MPa·m <sup>1/2</sup>
Residual Stress (TiC phase)		148 MPa ± 35 MPa (compressive)	

There is no significant difference between the properties as-received, stress-relieved, and HIPed conditions. The results for elastic modulus, compressive strength, flexural strength, density, and hardness were all found to be within experimental uncertainty to one another. Although there was an apparent increase in the fracture toughness is observed for the HIPed condition, the sample size is not large enough to assert that the average value is not comparable to that of the as-received condition. The Weibull modulus of the bending strength is calculated to be 4.6, indicating a high degree of variability.

The preliminary unit cell compression testing showcased in chapter 6 suggests that brazing is an effective joining method. For the single case examined, the failure of the structure was governed by the properties of the base material, not the joint. The EDM surface provides sufficient roughness for an adequate braze joint. The pyramidal unit cell (relative density of 4.97%) was found to have a compressive strength of  $\sim 70$ MPa. This result agrees well with predictions based upon the relationship developed by Deshpande and Fleck [5] to describe the performance of cellular materials.

## 7.2. Future Work

Now that the material is well characterized and a unit cell has been tested, there are a number of next steps that can be taken to further assess the use of this cermet as a base material for sandwich panel structure. First and foremost, a larger sampling size of the HIP samples for fracture toughness is critical. The results from chapter 5 revealed definitively that the fracture toughness of the as-received material is about  $15 \text{ MPa}\cdot\text{m}^{1/2}$ . However, considering the Weibull characteristics of the cermet, a larger sample size is needed to conclude whether or not the HIP process has an appreciable effect on the toughness properties.

Once the full characterization is complete, a logical next step would be the development of constitutive models to predict the properties of the cermet based on its composition. It would be a significant contribution to be able to predict the behavior of cermets based on their constituent phases and their corresponding volume fractions. Many authors have already explored this arena with WC-based cermets [48-51], so understanding the underlying mechanisms of the TiC/Ni would help to increase the robustness of cermet modeling.

The capability of monolithic cermet plates to resist impact loading has already been assessed by Compton and Zok [32], and three different pyramidal unit cells have been assessed on a preliminary basis by Dong [36]. With this information now in place, it would be of interest to construct a full sandwich panel with a pyramidal truss (or octet truss) core and determine the response to impact loading.

## APPENDICES

### A. Hot isostatic pressing (HIP) pressure and temperature parameters

A hot isostatic pressing (HIP) process is typically used to decrease the porosity of a solid, thereby pushing its density closer to its relative value. A HIP process could also induce a favorable change in the mechanical properties of a solid. With the nickel-bonded TiC system, this decrease in porosity could increase the fracture toughness, by improving the continuity between phases. Pores offer no fracture resistance. As such, the as-received cermet was subjected to a HIP cycle in order to determine if this post-process offered any advantages for used in a sandwich panel. If either the density or strength values fluctuate, a more favorable value of the material index outlined in Chapter 1 could be the result. Figure 55 below shows the parameters used to establish in the HIP cycle.

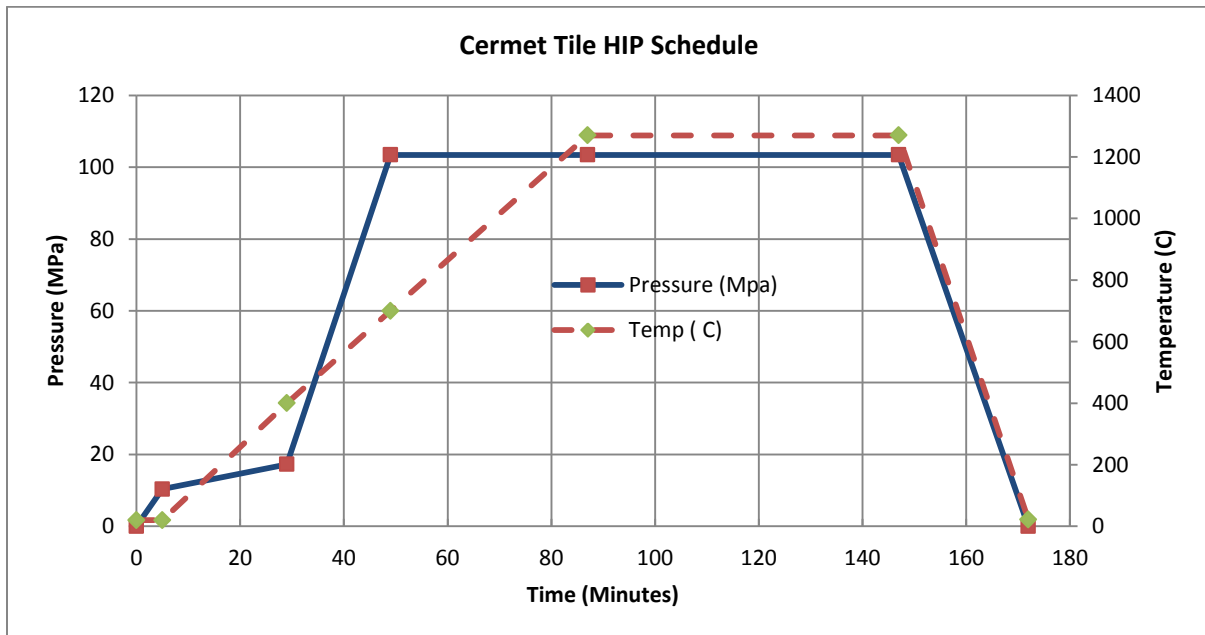


Figure 55: Temperature and Pressure parameters used in HIP run for DDG-X cermet tiles.

## B. Example of Lorentzian and Gaussian fits used in image analysis

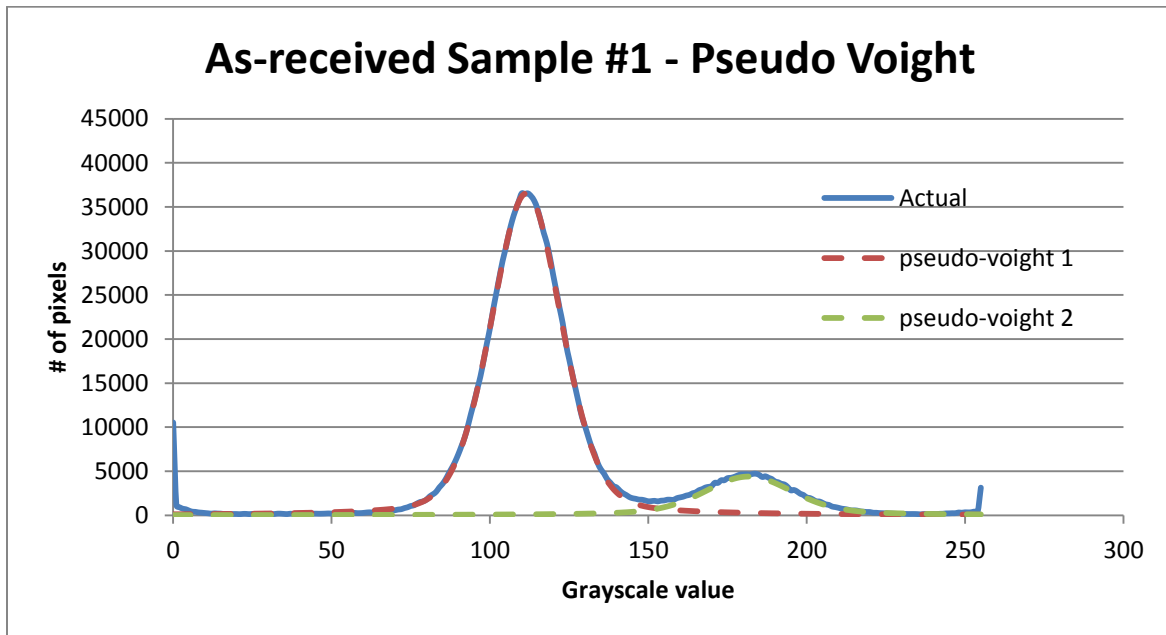


Figure 56: Example Pseudo-Voigt profile fit.

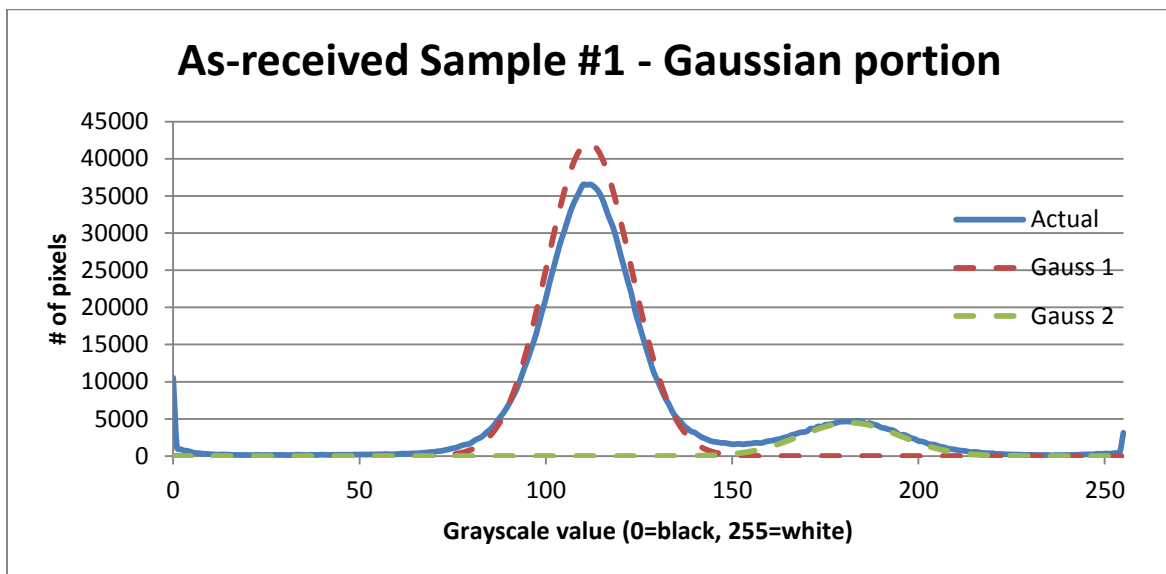


Figure 57: Gaussian portion of example pseudo-voigt fit shown in Figure 56.

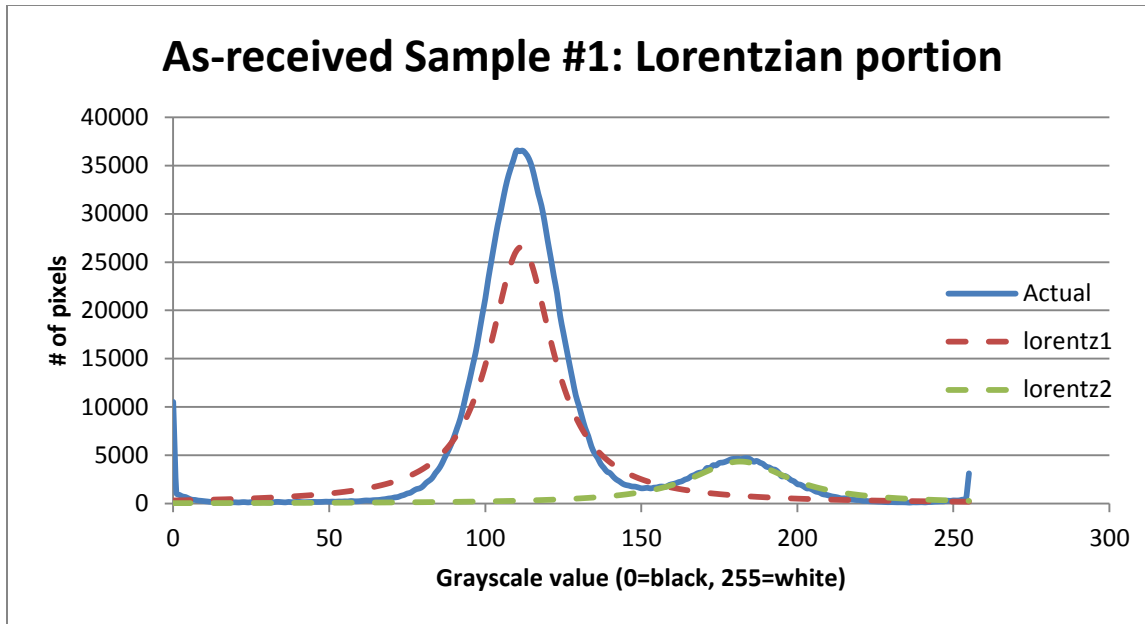


Figure 58: Lorentzian portion of example pseudo Voight fit shown in Figure 56.

### C. Quantile-quantile plot for particle size distribution analysis

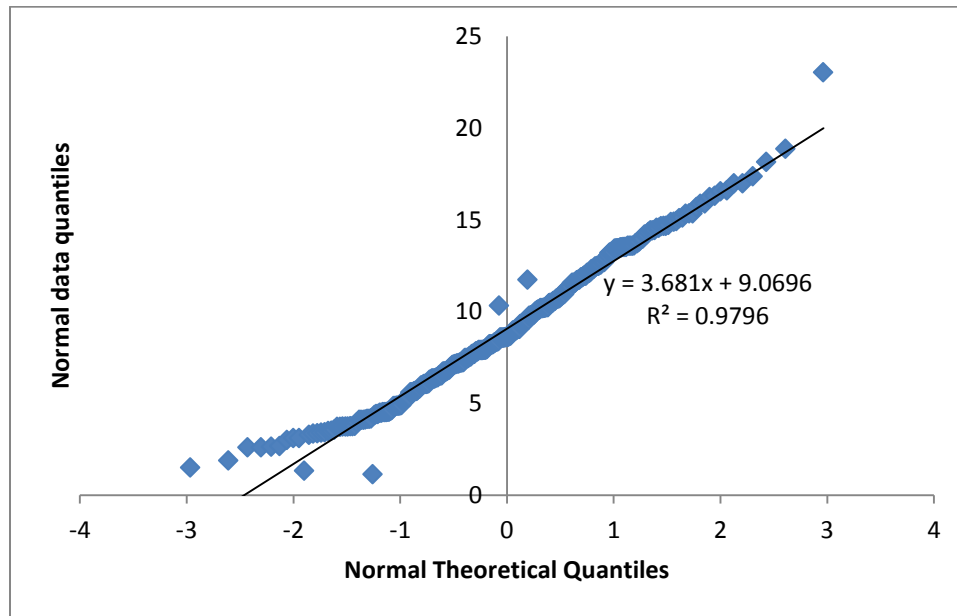


Figure 59: Quantile-quantile plot for as-received particle size distribution

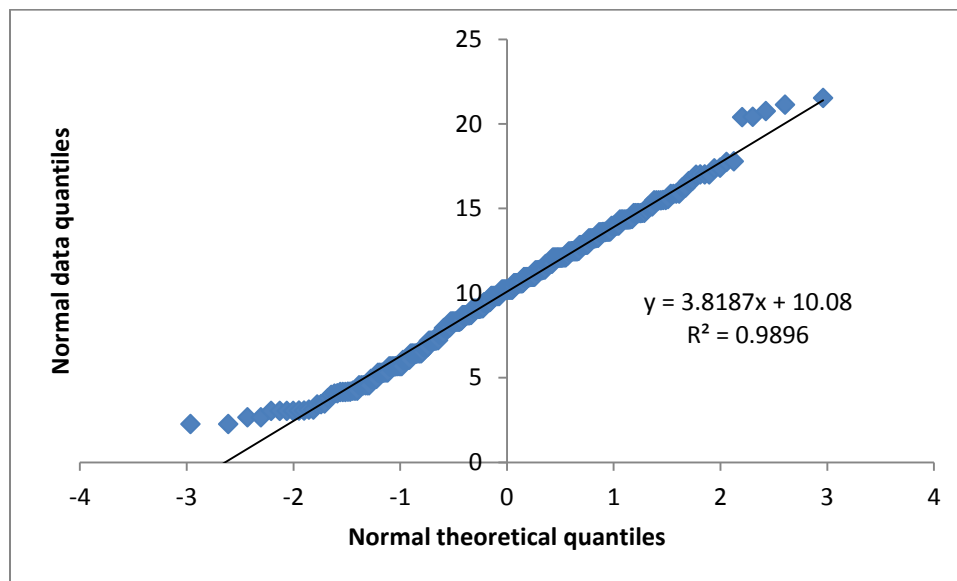


Figure 60: Quantile-quantile plot for HIPed particle size distribution

## D. Full porosity results for as-received and HIPed material

**Table 29: Phase fraction and % porosity results for as-received material, complete with coefficient of determination for pseudo-voight profile fitting**

<b>Sample</b>	<b>%TiC</b>	<b>%Ni</b>	<b>%porosity</b>	<b>R<sup>2</sup></b>
<b>1</b>	84.39	13.47	2.12	0.994
<b>2</b>	78.14	19.05	2.80	0.988
<b>3</b>	84.47	14.86	0.665	0.999
<b>4</b>	83.87	13.94	2.18	0.994
<b>5</b>	83.99	14.97	1.03	0.999
<b>6</b>	83.53	15.04	1.41	0.998
<b>7</b>	84.45	14.22	1.32	0.998
<b>8</b>	83.94	14.93	1.12	0.999
<b>9</b>	80.28	17.38	2.32	0.995
<b>10</b>	84.70	13.69	1.60	0.997
<b>AVG</b>	83.18	15.15	1.66	0.996
<b>ST DEV</b>	2.17	1.75	.673	0.003

**Table 30: Phase volume fraction and % porosity results for HIPed sample, complete with coefficient of determination for pseudo-voight profile fitting**

<b>Sample</b>	<b>%TiC</b>	<b>%Ni</b>	<b>%porosity</b>	<b>R<sup>2</sup></b>
<b>1</b>	84.39	12.94	02.66	0.990
<b>2</b>	86.28	12.15	01.56	0.997
<b>3</b>	85.75	10.76	03.47	0.983
<b>4</b>	89.31	9.41	01.26	0.999
<b>5</b>	87.80	10.99	01.19	0.999
<b>6</b>	88.11	10.75	01.12	0.999
<b>7</b>				
<b>8</b>				
<b>9</b>				
<b>10</b>				
<b>AVG</b>	86.94	11.17	1.88	0.995
<b>STD DEV</b>	1.79	1.22	0.967	0.006

## E. Full results for ICP and EDS analyses

**Table 31: Inductively Coupled Plasma results for as-received sample**

<b>Sample 1-1</b>					
	at wt.	wt.%	at %	wt.% (no C)	at % (no C)
<b>C</b>	12.01	11.80	36.88		
<b>Mo</b>	95.94	7.17	2.81	8.13	4.44
<b>Ni</b>	58.69	22.29	14.25	25.27	22.58
<b>Ti</b>	47.86	58.72	46.05	66.59	72.96
<b>Sample 1-2</b>					
	at wt.	wt.%	at %	wt.% (no C)	at % (no C)
<b>C</b>	12.01	9.69	30.28		
<b>Mo</b>	95.94	7.39	2.89	8.18	4.47
<b>Ni</b>	58.69	22.93	14.66	25.39	22.70
<b>Ti</b>	47.86	59.98	47.03	66.42	72.82
<b>Sample 1-3</b>					
	at wt.	wt.%	at %	wt.% (no C)	at % (no C)
<b>C</b>	12.01	15.32	49.78		
<b>Mo</b>	95.94	5.76	2.34	6.80	3.76
<b>Ni</b>	58.69	29.87	19.86	35.28	31.94
<b>Ti</b>	47.86	49.03	39.99	57.91	64.29

**Table 32: Second Run of Inductively coupled plasma results for as-received sample**

<b>Sample 2-1</b>					
	at wt.	wt.%	at %	wt.% (no C)	at % (no C)
<b>C</b>	12.017	10.273	33.372		
<b>Mo</b>	95.940	7.786	3.168	8.677	4.755
<b>Ni</b>	58.698	22.362	14.871	24.922	22.320
<b>Ti</b>	47.867	59.579	48.589	66.401	72.925
<b>Sample 2-2</b>					
	at wt.	wt.%	at %	wt.% (no C)	at % (no C)
<b>C</b>	12.017	12.472	40.514		
<b>Mo</b>	95.940	7.821	3.182	8.717	4.776
<b>Ni</b>	58.698	22.596	15.027	25.183	22.554
<b>Ti</b>	47.867	60.064	48.984	66.941	73.518

## F. Useful binary and ternary phase diagrams

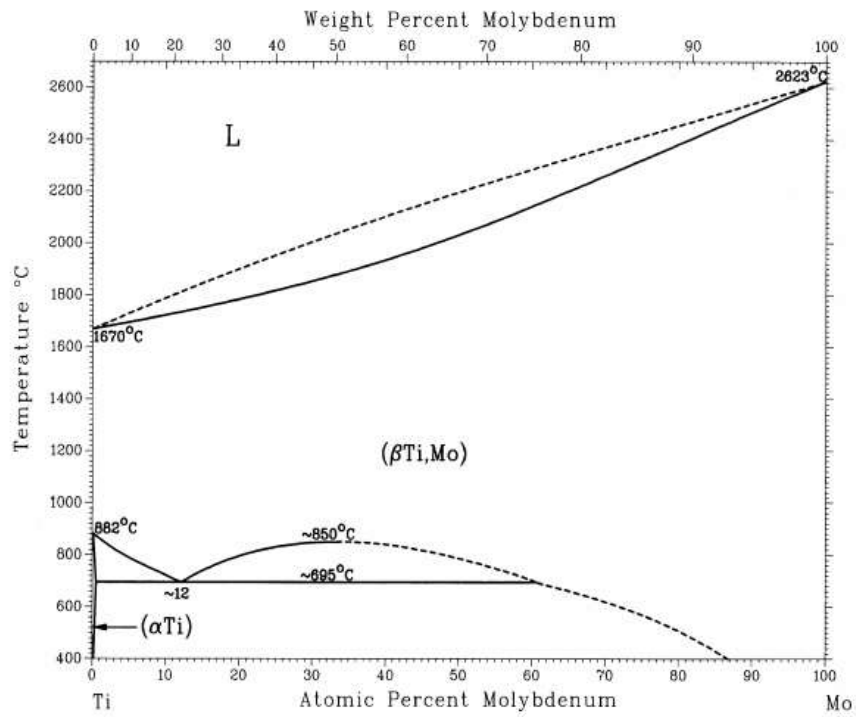


Figure 61: Titanium-molybdenum binary phase diagram [41]

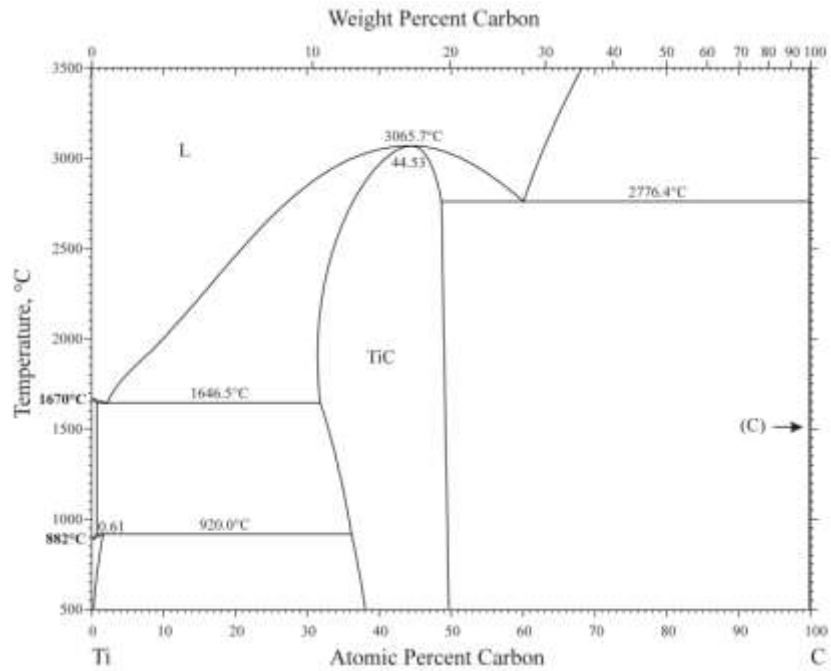


Figure 62: Titanium-carbon binary phase diagram [41]

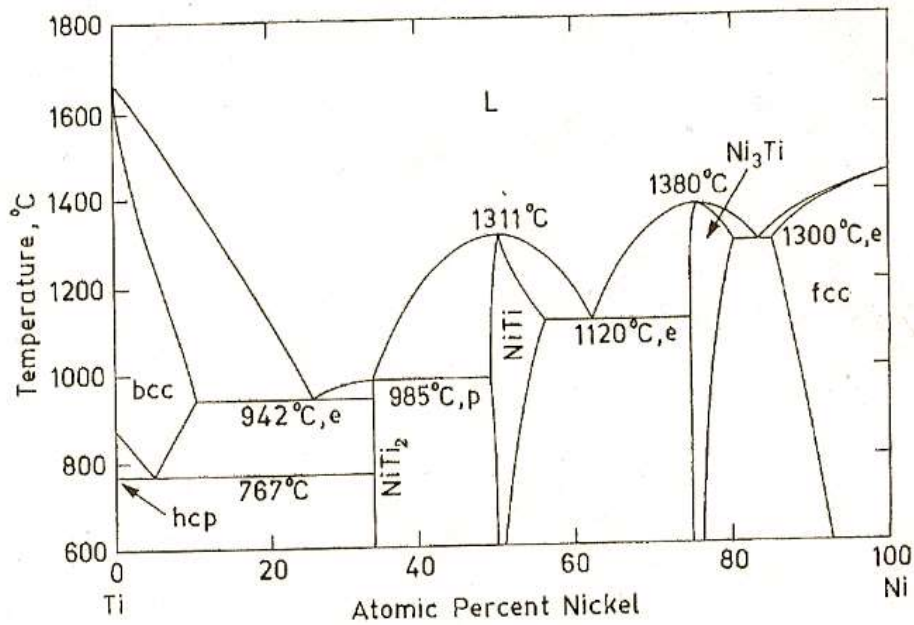


Figure 63: Titanium-nickel binary phase diagram [42]

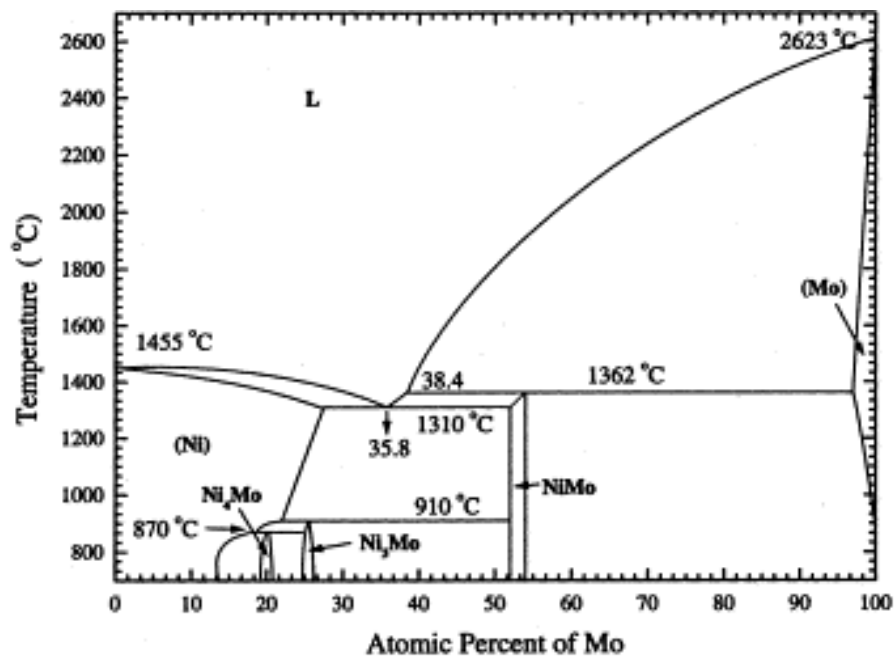


Figure 64: Nickel-molybdenum binary phase diagram [43]

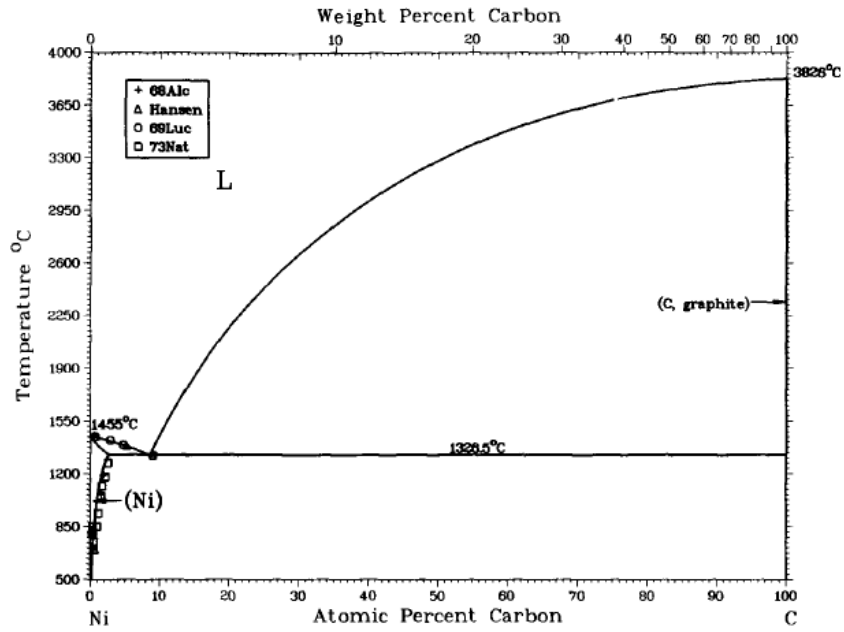


Figure 65: Nickel-carbon binary phase diagram [44]

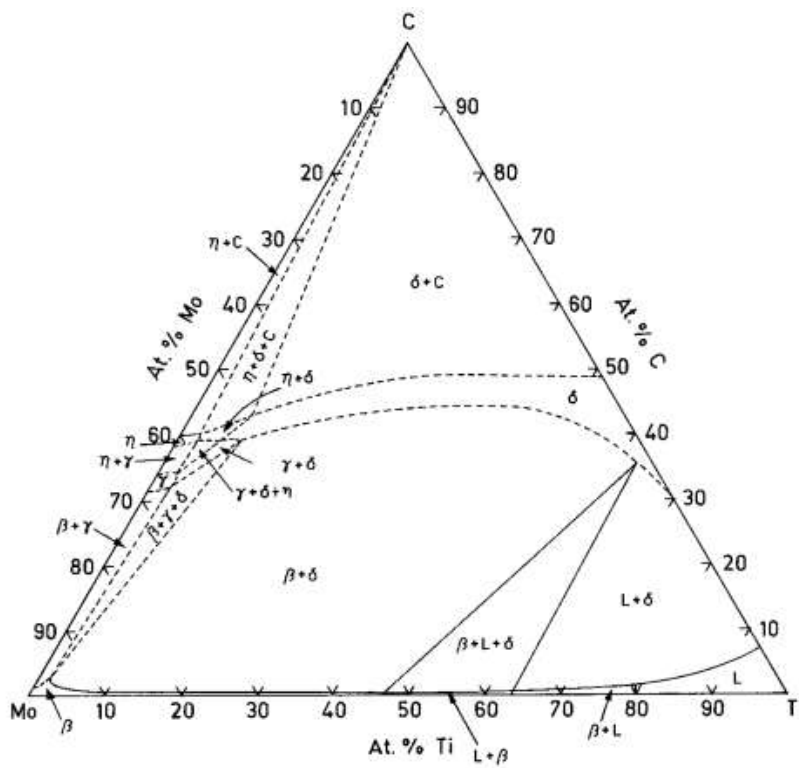


Figure 66: Isothermal section of the titanium-molybdenum-carbon ternary phase diagram at 1400C. The ternary phases are based on the binary phases as follows:  $\beta$ -( $\beta$ Ti,Mo);  $\gamma$ -( $\beta$ Mo<sub>2</sub>C);  $\delta$ -(TiC);  $\eta$ -(MoC<sub>1-x</sub>). [41]

## G. Single Edge V Notch Beam notch radii

**Table 33: List of fracture toughness values measured, and corresponding notch radii**

	sample	notch radius ( $\mu\text{m}$ )	Fracture Toughness
<b>As-received</b>	FT-1		16.3
	FT-2		19.0
	FT-4		15.5
	FT-5	31.5	19.2
	FT-6	33.2	13.9
	FT-7	34.1	16.2
	FT-9	27.9	15.4
<b>As-received (TOP of plate)</b>	TOP-1	32.4	14.0
	TOP-2	37.2	15.1
	TOP-3		14.7
	TOP-4	30	12.5
	TOP-5	31.7	15.5
<b>As-received (BOT of plate)</b>	BOT-3	41.3	14.7
	BOT-4	48.3	15.1
	BOT-6	30.6	14.2
	BOT-8		14.7
<b>HIP</b>	FT-2H	39	19.8
	FT-3H	34.5	16.3
	FT-5H	39.5	15.8

## H. Uncertainty analyses for pulse-echo ultrasonic measurements

The micrometer has a resolution of 0.001 mm. Since 0.001 mm is half of the possible values that will be rounded up or down, a triangular probability density function can be used to determine the standard uncertainty  $u_1$  (with 65 % Confidence Level) due to the micrometer resolution as:

$$u_1 = \frac{0.001}{\sqrt{6}} = \pm 0.000408 \text{ mm}$$

To increase the confidence level to 95%, the standard uncertainty  $u_1$  is multiplied by a factor of 1.81 to give  $u_1 = \pm 0.000739 \text{ mm}$ .

The uncertainty due to measurement repeatability is the standard deviation  $\sigma_d$  of the mean of the repeat thickness measurements. The standard uncertainty  $u_2$  for  $n$  number of measurements is thus given as:

$$u_2 = \frac{\sigma_d}{\sqrt{n}}$$

The combined uncertainty  $u$  of measurements is given as:

$$u = \sqrt{u_1^2 + u_2^2}$$

## I. Hardness Values

**Table 34: Vickers microhardness measurements for as-received condition**

	<b>Trial</b>	<b>Load (kgf)</b>	<b>d1 (mm)</b>	<b>d2 (mm)</b>	<b>HV</b>
<b>As-received 1</b>	1	1	0.0425	0.0437	998
	2	1	0.0420	0.0394	1120
	3	1	0.0400	0.0395	1173
	4	1	0.0447	0.0427	972
	5	1	0.0423	0.0425	1032
	6	1	0.0386	0.0387	1242
	7	1	0.0382	0.0381	1276
	8	1	0.0394	0.0394	1197
	9	1	0.0427	0.0403	1077
	10	1	0.0359	0.0352	1468
	<b>AVG</b>				<b>1155±150</b>
<b>As-received 2</b>	1	1	0.0479	0.0463	836
	2	1	0.0349	0.0355	1498
	3	1	0.0430	0.0403	1069
	4	1	0.0420	0.0382	1154
	5	1	0.0413	0.0463	967
	6	1	0.0414	0.0476	936
	7	1	0.0407	0.0444	1024
	8	1	0.0406	0.0417	1094
	9	1	0.0391	0.0434	1090
	<b>AVG</b>				<b>1117±168</b>

Table 35: Vickers microhardness measurements for HIPed condition

	Trial	Load (kgf)	d1 (mm)	d2 (mm)	HV
HIP 1	1	1	0.0337	0.0379	1448
	2	1	0.0368	0.0422	1187
	3	1	0.0344	0.0373	1446
	4	1	0.0305	0.0347	1745
	5	1	0.0355	0.0348	1502
	6	1	0.0343	0.0347	1559
	7	1	0.0342	0.0354	1530
	8	1	0.0315	0.0291	2019
	9	1	0.0351	0.0326	1620
	<b>AVG</b>				<b>1562 ± 228</b>
HIP 2	1	1	0.0438	0.0442	959
	2	0.5	0.0290	0.0272	1174
	3	0.5	0.0293	0.0301	1054
	4	0.5	0.0292	0.0297	1072
	5	0.5	0.0273	0.0263	1293
	6	0.5	0.0271	0.0277	1238
	7	0.5	0.0295	0.0280	1122
	8	0.5	0.0251	0.0242	1521
	9	0.5	0.0275	0.0275	1226
	<b>10</b>	0.5	0.0256	0.0263	1374
	<b>AVG</b>				<b>1203±165</b>

## J. Selected stress-strain curves from compression testing

Table 36: Compression testing complete results

Specimen Type	Specimen Label	Young's Modulus (Mpa)	.2% Yield (GPa)	Compressive Fracture Strength (GPa)
As- received	CT2-01	347		
	CT2-02	355		
	CT2-03	355	2.04	
	CT2-04	400	2.26	2.79
	CT2-05	246	2.08	2.47
	CT2-06	319	2.31	
	CT2-10	294	2.56	2.71
	<b>AVG</b>	<b>330</b>	<b>2.25</b>	<b>2.67</b>
HIPed	CT2-01-H	375		
	CT2-02-H	346		
	CT2-03-H	350	2.01	
	CT2-04-H	365	2.15	
	CT2-05-H	364	2.15	
	CT2-06-H	375	2.35	2.76
	CT2-09-H	296	2.42	2.48
	<b>AVG</b>	<b>353</b>	<b>2.22</b>	<b>2.62</b>

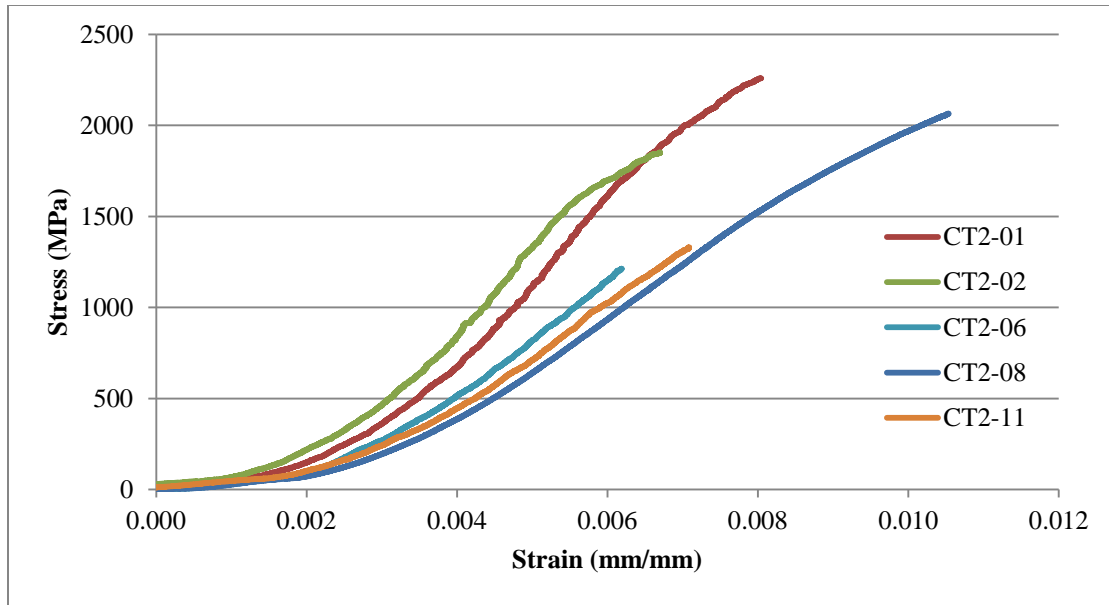


Figure 67: Stress-strain curves for as-received specimens

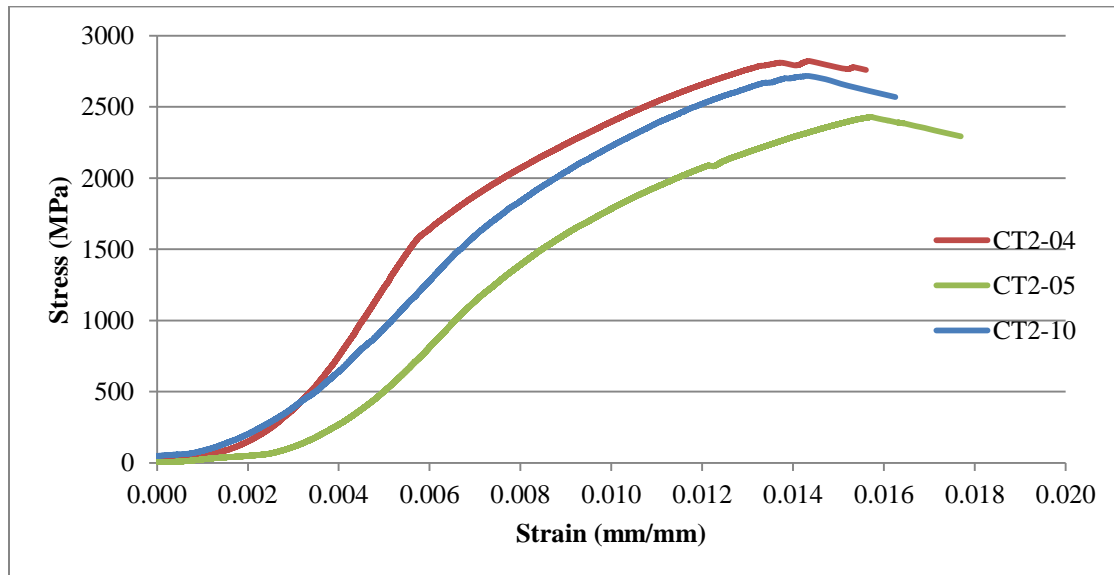


Figure 68: Stress-strain curves for as-received specimens tested to failure

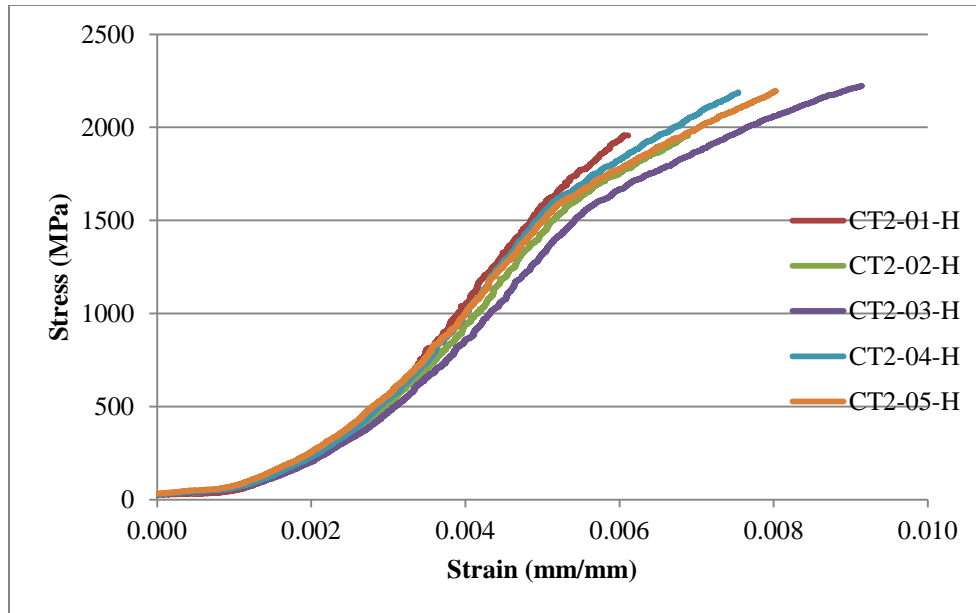


Figure 69: Stress-strain curves for HIPed specimens

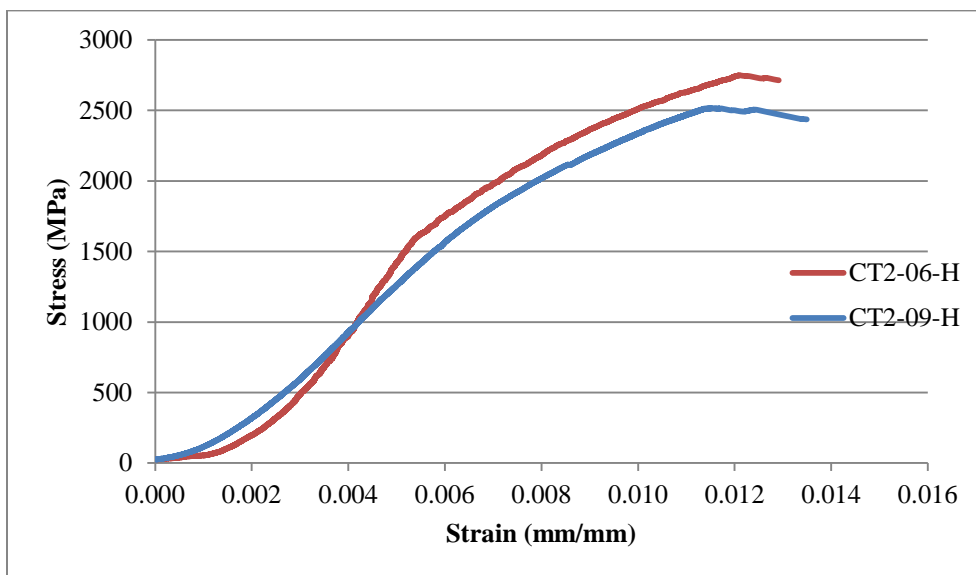


Figure 70: Stress-strain curves for as-received specimens tested to failure

## K. Selected load-deflection curves from single edge v notch beam experiment

All of the fracture toughness samples (one exception) exhibited load-deflection behavior with a completely brittle failure. It is observed in the figures below as an immediate inability to sustain load once cracking begins. The one exception (see sample TOP-1 in Figure 73) exhibits what the ASTM standard refers to as “pop-in” behavior. In this case the sample fractures, but the sample retains some load-bearing capacity.

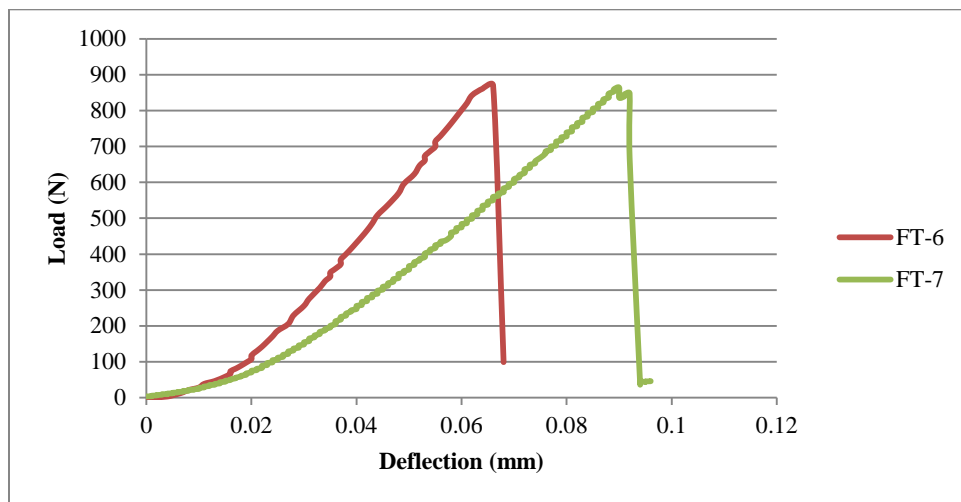


Figure 71: Sample load-deflection curves for as-received condition

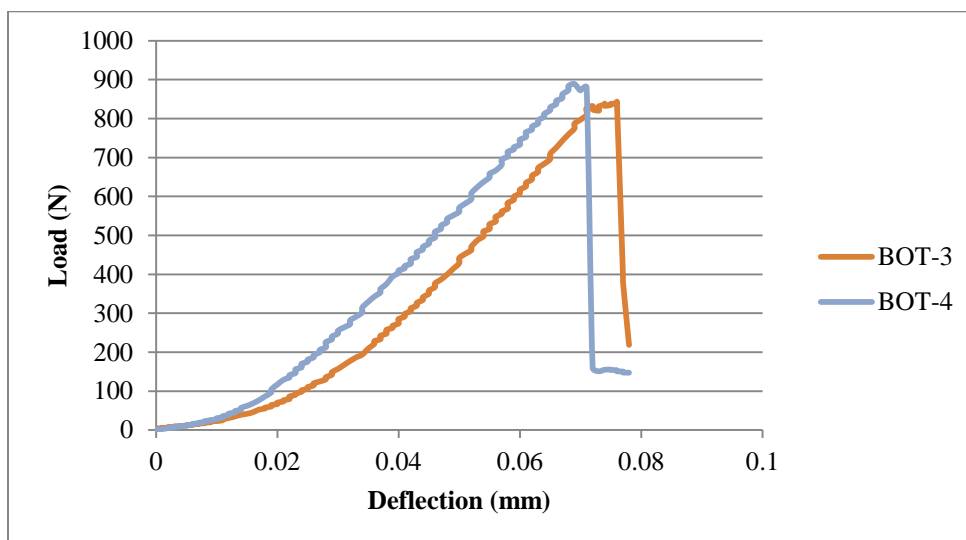


Figure 72: Sample load deflection curve for as-received material from bottom of 18mm plate.

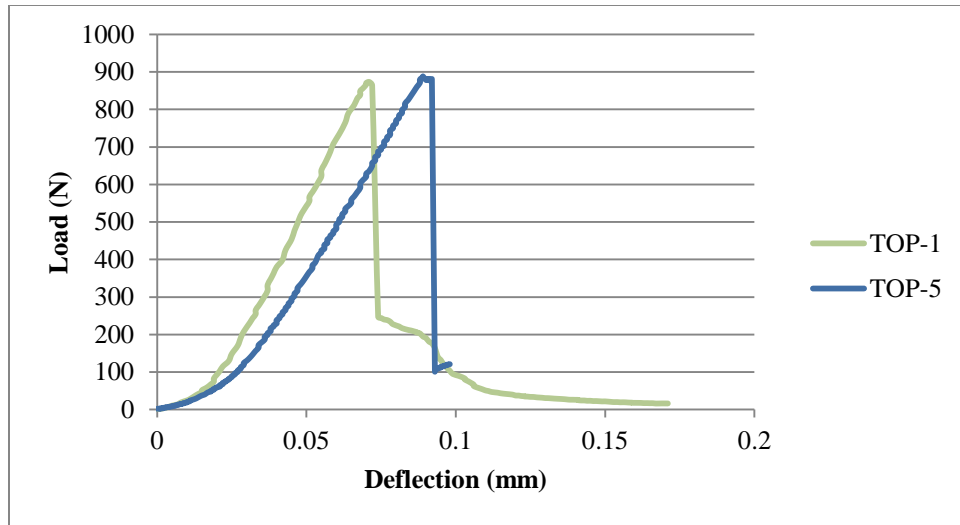


Figure 73: Sample load deflection curves for as-received material from top side of 18mm plate.

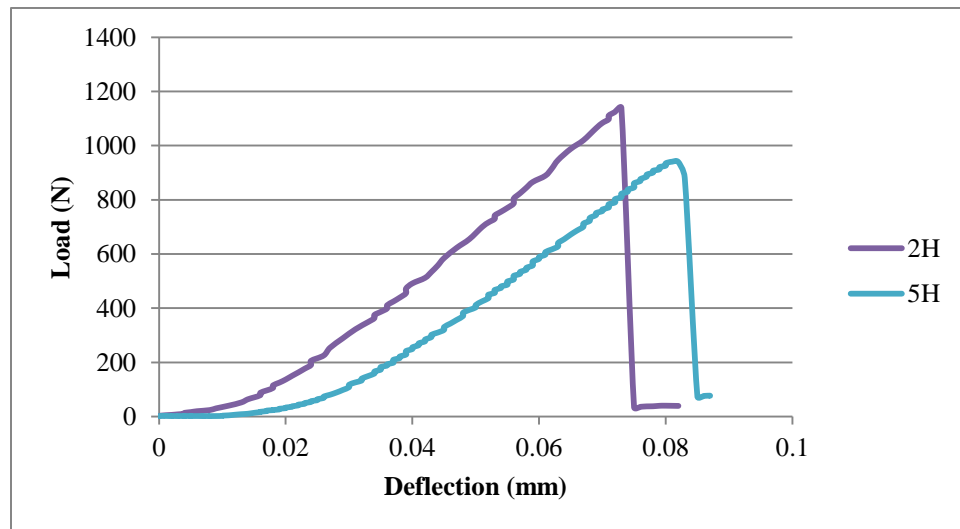


Figure 74: Sample load-deflection curves for HIPed material.

### L. Vendor supplied properties of DDG-X cermet (Ti(Mo)C-Ni)

The as-received cermet properties are provided by the vendor (Davis Defense Group) as shown in Figure 75 below. The vendor also provides a comparison to similar materials.

Ceramic Armor Material	DDG-X	B <sub>4</sub> C	SiC N	WC
Bulk Density (g/cm <sup>3</sup> )	4,2-5.45	2.49	3.2	15.4
Average grain Size (μm)	6	10	4	2
Flexural Strength (4-Pt MOR) @ RT (Ksi)	n/a	45	85	145
(MPa)	900-2000	310	580	1,000
Compressive Strength (GPa)	high	2.76	3.41	4.46
(Ksi)	n/a	400	494	646
Weibull Modulus (m)	15	12	17	10
Elastic Modulus (E) (GPa)	n/a	450	460	690
(Mpsi)	n/a	65	66	100
Poisson's Ratio (ν)	n/a	0.16	0.16	0.2
Hardness – Knoop 0.3 kg (kg/mm <sup>2</sup> )	1,600-2300	2,700	2,450	2,100
Fracture Toughness - Chevron Notch (MPa-m <sup>1/2</sup> )	20 (18-21)	3	2.8	7
Shear Modulus (GPa)	n/a	195	200	287
Bulk Modulus (GPa)	n/a	217	219	386
Longitudinal Wave Velocity (km/s)	n/a	13.7	12.43	6.86
Transverse Wave Velocity (km/s)	n/a	8.67	7.91	4.3

Figure 75: Cross-comparison chart provided with as-received cermet tiles.

### **M. Nanoindentation**

Nanoindentation is widely regarded as a reliable method for obtaining mechanical properties of nanoscale objects – particularly of thin films and multiphase materials [56-58]. Continuous stiffness measurements in particular allow for a “direct measure of dynamic contact stiffness during loading” [45], which provide enough data to deduce contact stiffness, elastic modulus, hardness, creep resistance, and even fatigue properties. Since this method is capable of assessing these objects on a nanoscale, it is used in this study to evaluate properties of the carbide and binder phases separately.

An MTS Systems Corporation nanoindenter was used with a 500mN load XP head with a standard Berkovitch tip was used to perform load-depth experiments on the Ti(Mo)C-Ni cermet in both the as-received and HIPed condition . This load cell configuration has the capability to resolve the load to 1mN and the penetration depth to 1 $\mu$ m. Utilizing a dynamic contact module, continuous stiffness measurements (CSM) could be performed in order to obtain a depth profile for the young's modulus and hardness of the cermet material. All CSM profiles were obtained using a harmonic load frequency of 45 Hz and a harmonic displacement of 2nm allowed. For each sample, the indenter contact area function vs. depth was calibrated via a sample of fused quartz with a known hardness and modulus. Next, a total of 16 indents in a 2x8 array with a spacing of 50 $\mu$ m were completed. A standard loading sequence consisting of a harmonic load segment, a holding segment at the prescribed depth, and an unload segment that ends with a hold at 10% of the maximum load to obtain a thermal drift correction. To reduce any effects of the environment, all experiments were performed on a vibration stabilized table within an environmental chamber that prevents vibration, temperature, and pressure from varying during the experiment.

It is important to note that at this penetration depth, the size of the indents was on the same length scale as the microstructure of the cermet. For example, the microstructure of the as-is cermet consists of particles of the Ti(Mo)C hard phase with an average particle size of 5.6 $\mu\text{m}$ , bordered by the softer Ni-Mo-Ti binder phase. By observation, the amount of binder between particles varies spatially. Since each indent has a footprint as wide as 7 $\mu\text{m}$ , many of the indents simultaneously penetrated both the binder and carbide phase. For these reasons, the results obtained from this experiment are considered largely qualitative, which is why they appear here in the appendix.

The widely accepted *Oliver-Pharr method* [46] was used to analyze the load vs. penetration depth data to obtain values for elastic modulus and hardness. A second method, presented by *Pethica and Oliver* [47] was used to evaluate the continuous stiffness. Details of the technique and analysis are not presented here, but can be found in previously published work by the authors mentioned. Figure 76 below shows an SEM micrograph of the HIPed sample after indentation. In the micrograph, four phenomena are observed – (1) evidence of pileup in the softer binder phase (2) fracture within the carbide phase observed as “pop-in” on the stress-strain curve [48], (3) particle debonding from binder, and (4) cleavage planes in the carbide phase after indenting.

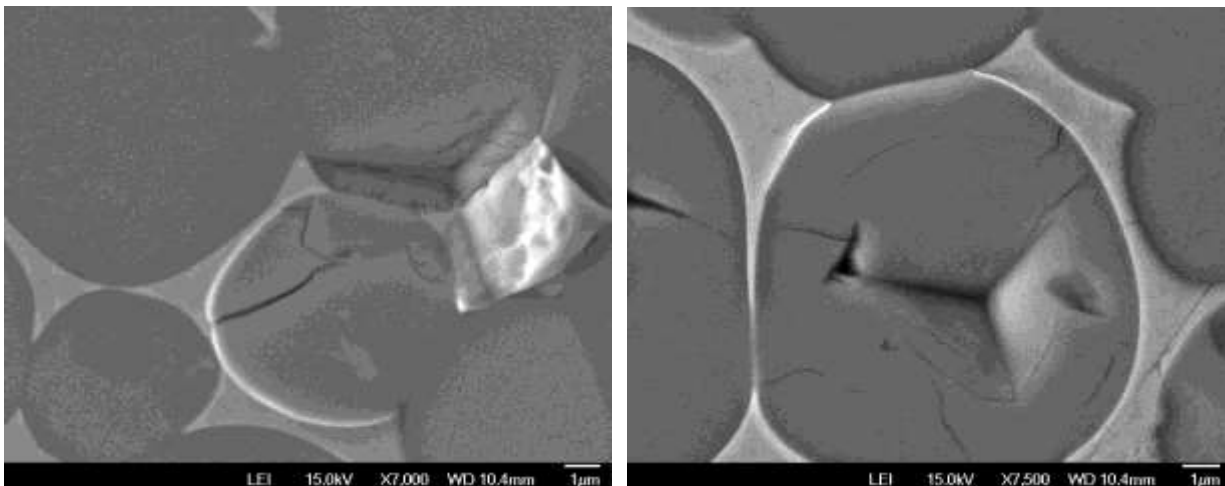


**Figure 76: SEM micrographs of indent on HIPed sample. (Left) showing evidence of (1) pileup in the binder (2) fracture within the carbide phase, (3) particle debonding from the binder, and (4) cleavage planes in the carbide phase after indenting. (Right) example of indentation exclusive to one phase.**

Although all four characteristics are not present in every indent, each is critical to understanding the load-displacement curves, and depth dependent modulus data, which is shown later. It is also clear to see that under these displacement conditions, the indent is on the same length scale as the microstructural features of the cermet. Due to the unknown effect of the indenter to the results obtained, the numerical values of results of this test should largely be considered qualitative.

Through analysis of the load-penetration depth data, the average hardness and elastic modulus can be determined using the *Oliver-Pharr method* [46]. In addition, the preferential indenting used allows differentiation between the carbide and binder phase within the cermet. Anecdotally, however, the different phases yield characteristically different responses, allowing the distinction as shown in Figure 77 and Figure 78 below. As expected, the carbide phase has a higher modulus, and has the capability to take more load than the binder phase for equal deflections. It was observed that the as-received condition had a larger mismatch between the

properties of the two phases, but it is unknown whether or not that is a result of the HIP considering the known error generated by the size similarity of the indented area to the microstructure.

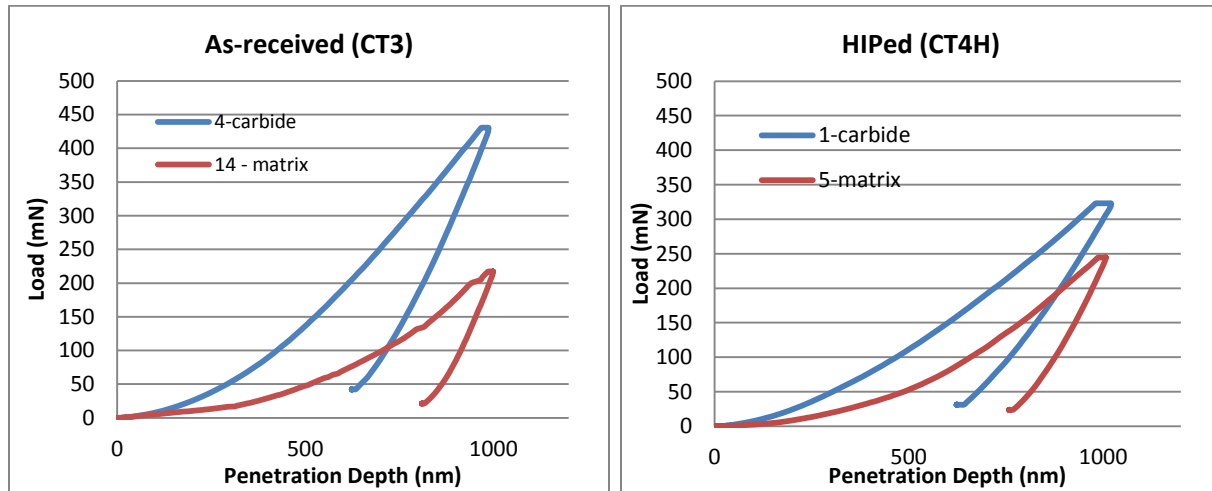


Figure 77: Load vs. penetration depth charts for both the as-is and HIPed sample.

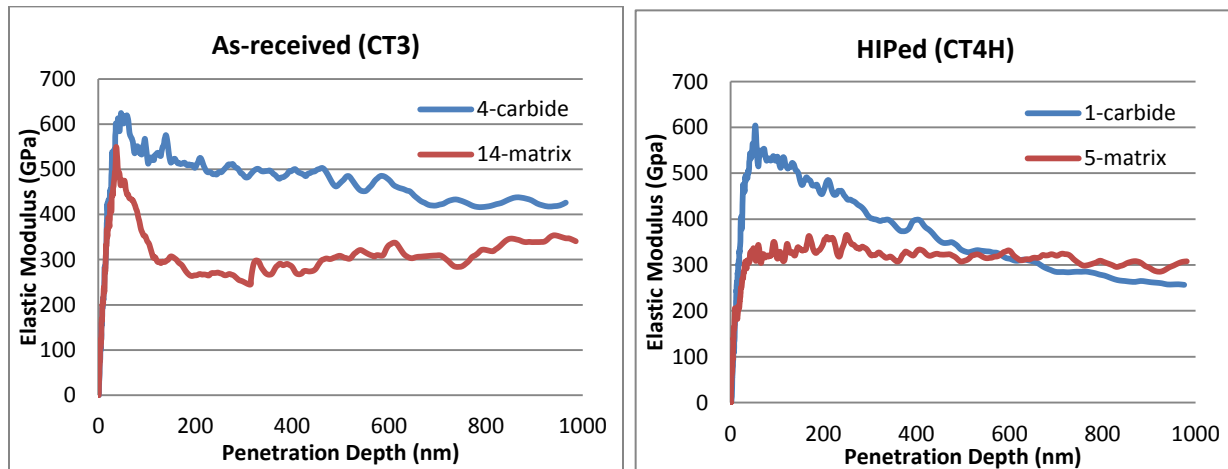


Figure 78: Modulus vs. depth data as captured via CSM measurement techniques. Striking differences are observed between the two phases.

## REFERENCES

- [1] Z. Xue and J. W. Hutchinson, "A comparative study of impulse-resilient metal sandwich plates," *International Journal of Impact Engineering*, vol. 30, pp. 1283-1305, 2004.
- [2] H. Wadley, *private communication*, 2013.
- [3] A. Wei, V. S. Deshpande, A. G. Evans, K. P. Dharmasena, D. T. Queheillalt, H. G. Wadley, Y. V. Murty, R. K. Elzey, P. D. Dudt, Y. Chen, D. Knight and K. Kiddy, "The resistance of metallic plates to localized impulse," *Journal of the Mechanics and Physics of Solids*, vol. 56, pp. 2074-2091, 2008.
- [4] H. Wadley, K. Dharmasena, Y. Chen, P. Dudt, D. Knight, R. Charette and K. Kiddy, "Compressive response of multilayered pyramidal lattices during underwater shock loading," *International Journal of Impact Engineering*, vol. 35, pp. 1102-1114, 2008.
- [5] V. S. Deshpande, N. A. Fleck and M. F. Ashby, "Effective properties of the octet-truss lattice material," *Journal of the Mechanics and Physics of Solids*, vol. 49, pp. 1747-1769, 2001.
- [6] H. Jie-Cai, X.-H. Zhang and J. V. Wood, "In-situ combustion synthesis and densification of TiC-xNi cermets," *Materials Science and Engineering A*, vol. 280, pp. 328-333, 2000.
- [7] J. C. LaSalvia and M. A. Meyers, "Microstructure, Properties, and Mechanisms of TiC-Mo-Ni Cermets produced by SHS," *International Journal of Self-Propagating High-Temperature Synthesis*, vol. 4, no. 1, pp. 43-57, 1995.
- [8] B. D. Cullity and S. R. Stock, *Elements of X-ray Diffraction*, Upper Saddle River, NJ: Prentice Hall, 2001.
- [9] P. S. Prevely, "X-ray diffraction residual stress techniques," *Metals Handbook*, vol. 10, pp. 380-392, 1986.
- [10] M. E. Fitzpatrick, A. T. Fry, P. Holdway, F. A. Kandil, J. Shackleton and L. Suominen, "Determination of Residual Stresses by X-ray Diffraction - Issue 2," Crown, Middlesex, 2005.
- [11] "MatWeb Material Property Data," MatWeb, LLC, 1999. [Online]. Available: <http://www.matweb.com/search/DataSheet.aspx?MatGUID=e6eb83327e534850a062dbca3bc758dc&ckck=1>. [Accessed 7 Sept 2013].
- [12] A. R. Denton and N. W. Ashcroft, "Vegard's law," *Physical Review A*, vol. 43, no. 6, pp. 3161-3164, 1991.
- [13] D. Mari, S. Bolognini, G. Feusier, T. Cutard, T. Viatte and W. Benoit, "TiMoCN based cermets Part II. Microstructure and room temperature mechanical properties," *International Journal of Refractory Metals and Hard Materials*, vol. 21, pp. 47-53, 2003.

- [14] G. Lloyd, "Atomic number and crystallographic contrast images with the SEM: a review of backscattered electron techniques," *Mineralogical Magazine*, vol. 51, pp. 3-19, 1987.
- [15] E. E. Underwood, *Quantitative Stereology*, Philadelphia: Addison-Wesley, 1970.
- [16] J. C. LaSalvia and M. A. Meyers, "Combustion Synthesis/Dynamic Densification of TiC-Ni Cermets," *Journal of Materials Synthesis and Processing*, vol. 2, no. 4, pp. 255-274, 1994.
- [17] E. Underwood, "Quantitative Stereology for Microstructural Analysis," in *Microstructural Analysis: Tools and Techniques*, 1973, pp. 35-66.
- [18] R. Asthana, A. Kumar and N. Dahotre, "Powder Metallurgy and Ceramic Forming," in *Materials Processing and Manufacturing Science*, Academic Press, 2006, pp. 167-241.
- [19] E. Stover, "The Binder Phase in titanium carbide-nickel cermets," Massachusetts Institute of Technology, 1952.
- [20] NORAN Instruments, *Energy-Dispersive X-ray Microanalysis*, Middleton, 1999.
- [21] X. Hou and B. Jones, "Inductively Coupled Plasma/Optical Emission Spectroscopy," John Wiley & Sons, Chichester, 2000.
- [22] Muso, Artist, *Principle of EDX*. [Art]. 2007.
- [23] J. Goldstein, D. E. Newbury, D. C. Joy, P. Lyman, E. Echlin, L. S. Lfshin and J. R. Michael, *Scanning Electron Microscopy and X-ray Microanalysis*, Springer, 2003.
- [24] K.-K. Pirkko, "Accuracy, Precision, and Detection Limits of SEM-WDS, WEM-EDS and PIXE in the Multi-Elemental Analysis of Medieval Glass," *X-Ray Spectrometry*, vol. 29, pp. 111-118, 2000.
- [25] N. Liu, C. Han, Y. Xu, S. Chao, M. Shi and J. Feng, "Microstructures and mechanical properties of nanoTiN modified TiC - based cermets for the milling tools," *Materials Science and Engineering A*, pp. 122-131, 2004.
- [26] L. Chen, W. Lengauer, P. Etmayer, K. Dreyer, H. Daub and D. Kassel, "Fundamentals of liquid phase sintering for modern cermets and functionally graded cemented carbonitrides (FGCC)," *International Journal of Refractory Metals and Hard Materials*, vol. 18, no. 6, pp. 307-322, 2000.
- [27] D. Cripps, "Netcomposites," Gurit, 2013. [Online]. Available: <http://www.netcomposites.com/guide/formulae/62>. [Accessed 11 July 2013].
- [28] J. M. Barranco and R. A. Warenchak, "Liquid Phase Sintering of Carbides using a Nickel Molybdenum Alloy," Benet Laboratories, Watervliet, 1988.
- [29] H. Awaji, T. Watanabe and Y. Sakaida, "Fracture Toughness Measurements of Ceramics by V notch

- technique," *Ceramics International*, vol. 18, pp. 11-17, 1992.
- [30] Versailles Project on Advanced Materials and Standards, "VAMAS Round Robin on Fracture Toughness Measurement of Ceramic matrix Composite," Japan Fine Ceramics Center, Nagoya, Japan, 1997.
- [31] Y. Torres, R. Bermejo, L. Llanes and M. Anglada, "Influence of notch radius and R-curve behavior on the fracture toughness evaluation of WC-Co cemented carbides.," *Engineering Fracture Mechanics*, vol. 75, pp. 4422-4430, 2008.
- [32] B. C. Compton and F. W. Zok, "Impact resistance of TiC-based cermets," *International Journal of Impact Engineering*, vol. 62, pp. 75-87, 2013.
- [33] M. F. Ashby and D. R. Jones, "The statistics of brittle fracture and case study," in *Engineering Materials 2: An Introduction to Microstructures, Processing and Design*, Oxford, Butterworth-Heinemann, 1998, pp. 185-193.
- [34] "Matweb Material Property Data," MatWeb, [Online]. Available: <http://matweb.com/search/DataSheet.aspx?MatGUID=058d1b70edbd4b2293f298c52bbf9818>.
- [35] J. F. Peters, M. Muthuswamy, J. Wibowo and A. Tordesillas, "Characterization of force chains in granular material," *Physical Review E*, vol. 72, no. 4, 2005.
- [36] L. Dong and H. Wadley, *Private Communication*, Charlottesville, 2013.
- [37] Z. R. Li, J. C. Feng and J. Cao, "Vacuum diffusion bonding of TiB<sub>2</sub> cermet to TiAl based alloys," *Materials Science and Technology*, vol. 20, pp. 1666-1668, 2004.
- [38] Air Products and Chemicals, Inc, "Introduction to Furnace Brazing," 2001.
- [39] Sulzer Metco, "An Introduction to Brazing," 2011.
- [40] V. S. Deshpande and N. A. Fleck, "Collapse of truss core sandwich beams in 3-point bending," *International Journal of Solids and Structures*, vol. 38, pp. 6275-6305, 2001.
- [41] D. Bandyopadhyay, B. Haldar, R. C. Sharma and N. Chakraborti, "The Ti-Mo-C (Titanium-Molybdenum-Carbon) System," *Journal of Phase Equilibria*, vol. 20, no. 3, 1999.
- [42] D. Bandyopadhyay, R. C. Sharma and N. Chakraborti, "The Ti-Ni-C system (Titanium-Nickel-Carbon)," *Journal of Phase Equilibria*, vol. 21, no. 2, 2000.
- [43] A. Arya, G. K. Dey, V. K. Vasudevan and S. Banerjee, "Effect of chromium addition on the ordering behaviour of Ni-Mo alloy: experimental results vs. electronic structure calculations," *Acta Materialia*, vol. 50, no. 13, pp. 3301-3315, 2002.

- [44] M. Singleton and P. Nash, "The C-Ni (Carbon-Nickel) System," *Bulleting of Alloy Phase Diagrams*, vol. 10, no. 2, pp. 121-126, 1989.
- [45] X. Li and B. Bhushan, "A review of nanoindentation continuous stiffness measurement technique and its application.," *Materials Characterization*, vol. 48, pp. 11-36, 2002.
- [46] W. C. Oliver and G. M. Pharr, "An improved technique for determining hardness and elastic modulus using load and displacement sensing indentation experiments," *Journal of Materials Research*, vol. 7, no. 6, pp. 1564-1583, 1992.
- [47] W. Oliver and J. Pethica, "Method for continuous determination of the elastic stiffness of contact between two bodies". United States of America Patent US4848141 A, 18 July 1989.
- [48] J. Ding, Y. Meng and S. Wen, "Mechanical properties and fracture toughness of multilayer hard coatings using nanoindentation," *Thin Solid Films*, vol. 371, pp. 178-182, 2000.
- [49] J. J. Rimoli, B. Talamini, J. J. Wetzel, K. P. Dharmasena, R. Radovitzky and H. G. Wadley, "Wet-sand impulse loading of metallic plates and corrugated core sandwich panels," *International Journal of Impact Engineering*, vol. 38, pp. 837-848, 2011.
- [50] H. Jie-Cai, X.-H. Zhang and J. V. Wood, "In-situ combustion synthesis and densification of TiC-xNi cermets," *Materials Science and Engineering A*, vol. 280, pp. 328-333, 2000.
- [51] M. E. Fitzpatrick, A. T. Fry, P. Holdway, F. A. Kandial, J. Shackleton and L. Suominen, "Determination of Residual Stresses by X-ray diffraction," Crown, Middlesex, UK, 2005.
- [52] W. C. Oliver and G. M. Pharr, "Measurement of hardness and elastic modulus by instrumented indentation: Advances in understanding and refinements to methodology.," *Journal of Materials Research*, vol. 19, no. 1, 2003.
- [53] V. Bonache, E. Rayon, M. D. Salvador and D. Busquets, "Nanoindentation study of WC-12Co hardmetals obtained from nanocrystalline powders: Evaluation of hardness and modulus on individual phases," *Materials Science and Engineering A*, vol. 527, pp. 2935-2941, 2010.
- [54] A. R. Denton and N. W. Ashcroft, "Vegard's law," *Physical Review A*, vol. 43, no. 6, pp. 3161-3164, 1990.
- [55] Z. Hashin and S. Shtrickman, "A Variational Approach to the Theory of the Elastic Behaviour of Multiphase Materials," *Journal of the Mechanics and Physics of Solids*, vol. 11, pp. 127-140, 1962.
- [56] B. D. Flinn, C. S. Lo, F. W. Zok and A. G. Evans, "Fracture Resistance Characteristics of a Metal-Toughened Ceramic," *Journal of American Ceramics*, vol. 76, no. 2, pp. 369-375, 1993.
- [57] K. S. Ravichandran, "Fracture Toughness of Two Phase WC-Co Cermets," *Acta metall. mater.*, vol. 42, no. 1, pp. 143-150, 1994.

- [58] V. K. Sarin and T. Johansson, "On the Deformation of WC-Co Cemented Carbides," *Metal Science*, vol. 9, pp. 472-476, 1975.
- [59] M. G. Gee, R. Roebuck, P. Lindahl and H. O. Andren, "Constituent phase nanoindentation of WC/Co and Ti(C,N) hard metals," *Materials Science and Engineering A*, vol. 209, pp. 128-136, 1996.
- [60] G. Pezzotti, H. Huebner, H. Suenobu, O. Sbaizero and T. Nishida, "Analysis of Near-Ti Crack Bridging in WC/Co cermet," *Journal of European Ceramic Society*, vol. 19, pp. 119-123, 1999.
- [61] AK Steel Corporation, "AK Steel," 2007. [Online]. Available: [http://www.aksteel.com/pdf/markets\\_products/stainless/precipitation/17-4\\_PH\\_Data\\_Sheet.pdf](http://www.aksteel.com/pdf/markets_products/stainless/precipitation/17-4_PH_Data_Sheet.pdf). [Accessed 19 September 2013].
- [62] K. Dharmasena, D. Queheillalt, H. Wadley, P. Dudd, Y. Chen, D. Knight and A. Evans, "Dynamic compression of metallic sandwich structures during planar impulsive loading in water," *European Journal of Mechanics A/Solids*, vol. 29, pp. 56-67, 2010.
- [63] K. Dharmasena, H. Wadley, T. Liu and V. Deshpande, "The dynamic response of edge clamped plates loaded by spherically expanding sand shells," *international Journal of Impact Engineering*, vol. 62, pp. 182-195, 2013.
- [64] D. Queheillat, Y. Murty and H. Wadley, "Mechanical properties of an extruded pyramidal lattice truss sandwich structure," *Scripta Materialia*, vol. 58, pp. 76-79, 2008.
- [65] A. Dridi, B. Bouhafs, P. Ruterana and H. Aourag, "First-principles calculations of vacancy effects on structural and electronic properties of TiCx and TiNx," *Journal of Physics: Condensed Matter*, vol. 14, pp. 10237-10249, 2002.
- [66] G. Hart, B. Klein and S. Begay, "Vacancy ordering and non-stoichiometry in TiC(1-x)Qx and TiN(1-x)Qx," *Complex Inorganic Solids*, pp. 99-109, 2005.